Displacement and Stress Computation in Dual-Horizon State-Based Peridynamics

Ali Khoshrou

A Thesis

in

The Department

of

Mechanical, Industrial, and Aerospace Engineering

Presented in Partial Fulfillment of the Requirements

for the Degree of

Master of Applied Science (Mechanical Engineering) at

Concordia University

Montréal, Québec, Canada

April 2024

CONCORDIA UNIVERSITY

School of Graduate Studies

This is to certify that the thesis prepared

By: **Ali Khoshrou**

Entitled: **Displacement and Stress Computation in Dual-Horizon State-Based Peridynamics**

And submitted in partial fulfillment of the requirements for the degree of

Master of Applied Science (Mechanical Engineering)

Complies with the regulations of this University and meets the accepted standards with respect to originality and quality.

Signed by the Final Examining Committee:

_____ Chair/Examiner
Dr. Behrooz Yousefzadeh

_____ External Examiner
Dr. Biao Li

_____ Supervisor
Dr. Ayhan Ince

Approved by _____
Dr. Sivakumar Narayanswamy, Graduate Program Director

_____ 2024 _____
Dr. Mourad Debbabi, Dean
Gina Cody School of Engineering and Computer Science

Abstract

Displacement and Stress Computation in Dual-Horizon State-Based Peridynamics

Ali Khoshrou

Numerous research endeavors have delved into the realm of multi-horizon peridynamics frameworks and their connection to the interplay between peridynamic force densities and stress tensors in the field of continuum mechanics. This study introduces an enhanced iteration of the dual horizon peridynamic (DH-PD) model, merging established multi-horizon peridynamic frameworks with equations that specifically establish stress components using peridynamic forces. This pioneering model offers a method to analyze stress within a 2D framework.

The new formulation allows for choosing two horizons and concentration of more material points in high-stress areas. By using this dual horizon idea, the model computes faster by focusing on areas of interest while providing accurate results in less crucial areas. The peridynamics equations are solved using a direct integration method.

The efficiency of the model is assessed by benchmark problem tests involving a 2D steel plate containing a central hole under uniform tension. The obtained solution is rigorously compared with finite element solutions. This study demonstrates that the extended DH-PD model is capable of computing stress and displacement fields, regardless of whether they are near high-stress concentration zones or in distant areas of the simulated 2D setup. The model showcases its ability to accurately capture the intricate behavior of stress and deformation.

Acknowledgments

I express my gratitude to Prof. Ayhan Ince, my supervisor, for his guidance over the past three years as I worked on my thesis. He not only directed me in completing the project but also imparted valuable lessons on effective research methods. His steadfast support and tireless sharing of knowledge have consistently motivated me to persevere in my research endeavors. I am committed to delivering meaningful contributions to the scientific community, driven by the inspiration he has provided throughout this journey.

Dedications

To my beloved parents and my only sibling

Table of Contents

List of Figures

List of Tables

Symbols

Symbol	Description	Unit/ value
$\boldsymbol{b_i}$	Body force (i.e. external force) density applied to material point number i	$N \cdot m^{-3}$
$\boldsymbol{c}$	Peridynamic bond constant	$N \cdot m^{-6}$
$\boldsymbol{d}$	A peridynamic parameter used in force density calculation	$\frac{9}{4\pi\delta^4}\ m^{-4}$
E	Young's modulus	$200\ GPa$
$\boldsymbol{F}$	Initial force vector	$N \cdot m^{-3}$
$\boldsymbol{H}(\mathbf{x_i})$	Horizon set of material point number i	-
$\boldsymbol{L}$	Length dimension of the benchmark steel plates	cm
$\boldsymbol{M}$	Stable mass matrix	$N \cdot s^2 \cdot m^5$
$\boldsymbol{\rho}$	Central hole vertex curvature	cm
$\boldsymbol{r_a}$	Central hole major radius	cm
$\boldsymbol{r_b}$	Central hole minor radius	cm
$\boldsymbol{s_{ij}}$	Peridynamical stretch between two material points i and j	-
$\boldsymbol{t_{ij}}$	Peridynamical force density exerted by material point j to material point i	$N \cdot m^{-6}$
$\boldsymbol{u_i}$	Displacement of material point number i	m
$\boldsymbol{V_{x_i}}$	Volume of the material point number i	m^3
W	Width dimension of the benchmark steel plates	cm
$\boldsymbol{x_i}$	Initial cartesian coordinates of the material point number i	m
$\boldsymbol{y_i}$	Post-deformation cartesian coordinates of the material point number i	m
$\boldsymbol{\alpha}$	A peridynamic parameter used in force density calculation	$N \cdot m^{-2}$
$\boldsymbol{\beta}$	A peridynamic parameter used in force density calculation	$N \cdot m^{-7}$
$\boldsymbol{\Gamma}$	A subset of peridynamical body (i.e. subdomain)	-

$\boldsymbol{\Delta t}$	Time step	s
$\boldsymbol{\delta_i}$	Horizon size of material point number i	m
$\boldsymbol{\theta_i}$	Dilatation term of material point number i	-
κ	Bulk modulus	$143\ GPa$
μ	Shear modulus	$77\ GPa$
$\boldsymbol{\nu}$	Poisson's ratio	0.3
$\boldsymbol{\xi_{ij}}$	Initial relative position vector between material point number i and j	m
$\boldsymbol{\eta_{ij}}$	Relative displacement vector between material point number i and j	m
$\boldsymbol{\rho}$	Mass density	$kg \cdot m^{-3}$
$\boldsymbol{\sigma}$	Peridynamic stress tensor	$N \cdot m^{-2}$
$\boldsymbol{\tau}$	Force flux	$N \cdot m^{-2}$
$\boldsymbol{\phi}$	Horizon ratio	-
$\boldsymbol{V}$	Stress tensor	$N \cdot m^{-2}$
$\mathfrak{B}$	Peridynamic material point set (i.e. peridynamic body)	-
$\boldsymbol{f}$	Peridynamical pairwise force density	$N \cdot m^{-6}$

Chapter 1:

Introduction and literature review

Continuum mechanics is an established branch of mechanics that has been developed to explain the mechanical response of materials to internal and external forces, first proposed by Augustin-Louis Cauchy, the father of continuum mechanics [1]. The principal assumption of this theory is the continuity of the material which ignores the fact that they are made of particles, atoms, and contain microscopic defects. With the constitutional principles of continuum mechanics set in conservation of mass, energy, and momentum, the governing equations of continuum mechanics take the form of integral or differential equations which are then solved using calculus.

With the disregard of inherent discontinuous nature of materials, continuum mechanic models are able to sufficiently explain and predict the mechanical behavior of materials at a macroscopic level; However, the constitutive relationships governing this field fail to accommodate for the macroscopic features that are caused by microscopical properties, such as crack initiation in fracture mechanics or the role of microstructure in deformation theories[2-9]. For instance, crack initiation, a symptom of material fatigue, emerges from micro-cracks near defects such as pores, grain boundaries, or dislocations [10, 11]. The assumption of continuity in continuum mechanics requires that the material consist of infinitesimal volumes that are continuous. This theory therefore disregards any involvement of microscopic discontinuities that naturally occur in all materials. This shortcoming is worsened as constitutive equations in continuum mechanics will have singularities in a discontinuous body, since they are mathematically spatial derivative equations. Therefore, the study of crack initiation and crack propagation using continuous models requires special treatments. [12, 13].

1.1. History of fracture analysis

1.1.1. Linear Elastic Fracture Mechanics

One of the earliest attempts at remedying the treatment of crack propagation was done by Griffith in the early twentieth-century by developing the concept of Linear Elastic Fracture Mechanics (LEFM), which treats the crack growth of pre-existing cracks in a continuous body using continuum principles [14]. This theory was later developed with the introduction of new concepts such as critical energy release rate which is equal to the decrease of total potential energy per increase of fracture surface area [15, 16], and stress intensity factor (K) which indicates the severity of stress at the crack tip. The introduction of stress intensity factor helps to characterize the crack tip conditions using a single parameter K. In other words, knowing the value K, one can find the distribution of stress around the crack tip given a linear elastic material. Tension opening, sliding shear, tear shear are the types LEFM fracture which differ in the direction of the fracture forces with respect to the fracture surface, as seen in Figure 1.1.The most common fracture mode is the

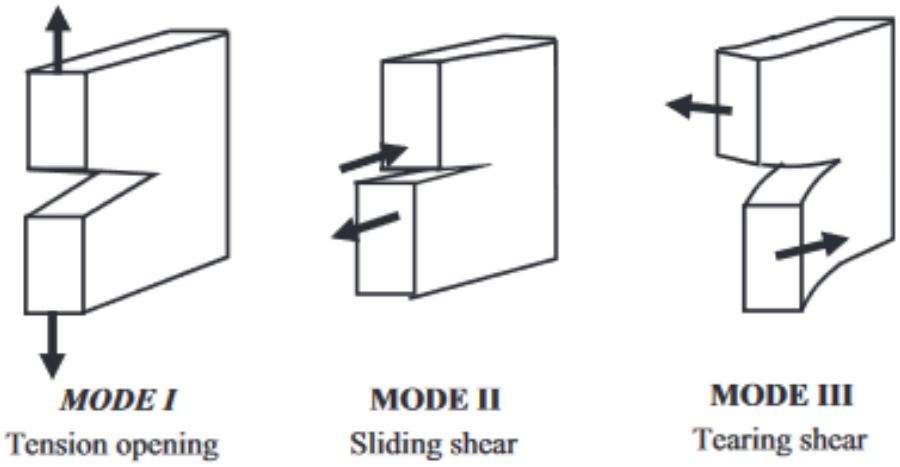

Figure 1.1. Modes of fracture relative to the direction of crack propagation [17].

opening mode which occurs if the stress is normal and is perpendicular to the crack plane. In case of shear stresses, Mode II and Mode III can occur, with Mode II having the shear stress perpendicular to the crack front and Mode III having the shear stress applied parallel to the crack front [17].

Depending on the mode of fracture, its corresponding roman numeric will be added as a subscript to K. For example, in Mode I, which is the most studied of the three modes, the stress intensity

factor is shown as K_I. The critical stress intensity for Mode I is known as K_{IC}, which is an inherent property and does not depend on geometry. If the condition in Eq. (1) is true, the crack grows.

$$K_I > K_{Ic} \tag{1}$$

It is worth noting that although LEFM has been adopted in wide range of engineering applications, it comes with limitations. First, there is the assumption of linearity and elasticity of the material. LEFM is not applicable to non-linear materials such as elastomers, nor is it applicable when the deformation is considered plastic. In other words, when using LEFM, the plastic deformation near the crack front is assumed to have an infinitesimal volume [18]. Secondly, the underlying issue of singularities still persist. This means that LEFM predicts infinite stress magnitudes near the crack front. As explained, this is due to the nature of continuum mechanics equations, which rely on spatial derivatives equations. This led to validity of LEFM - as was proposed by Griffith – limited only to brittle materials such as glass and ceramics [18]. Studying fracture mechanics of metals and alloys that undergo large plastic deformation prior to fracture require a modified theory that incorporates the effect of plastic deformation on crack propagation.

1.1.2. Irwin's modification

Following Griffith, Irwin [19] postulated that it is the stress field that determines whether fracture is possible, and that the energy required to create fracture surfaces can be measured with the stress field near the crack tip. Irwin concluded that the stress field near the fracture surface is dependent on certain geometric parameters such as plane thickness and mode of fracture. In thin plates, the conditions of "plane stress" emerge, which limits the stress component normal to thickness of the plate to zero. The thinness of the plate prevents forces to be transmitted throughout the thickness, resulting in zero stress in that direction. On the other hand, there is the "plane strain" condition, which prevails in thick specimen. Under plane strain conditions, the plate can produce adequate forces in the transverse direction, resulting to the existence of stress component in the traverse direction.

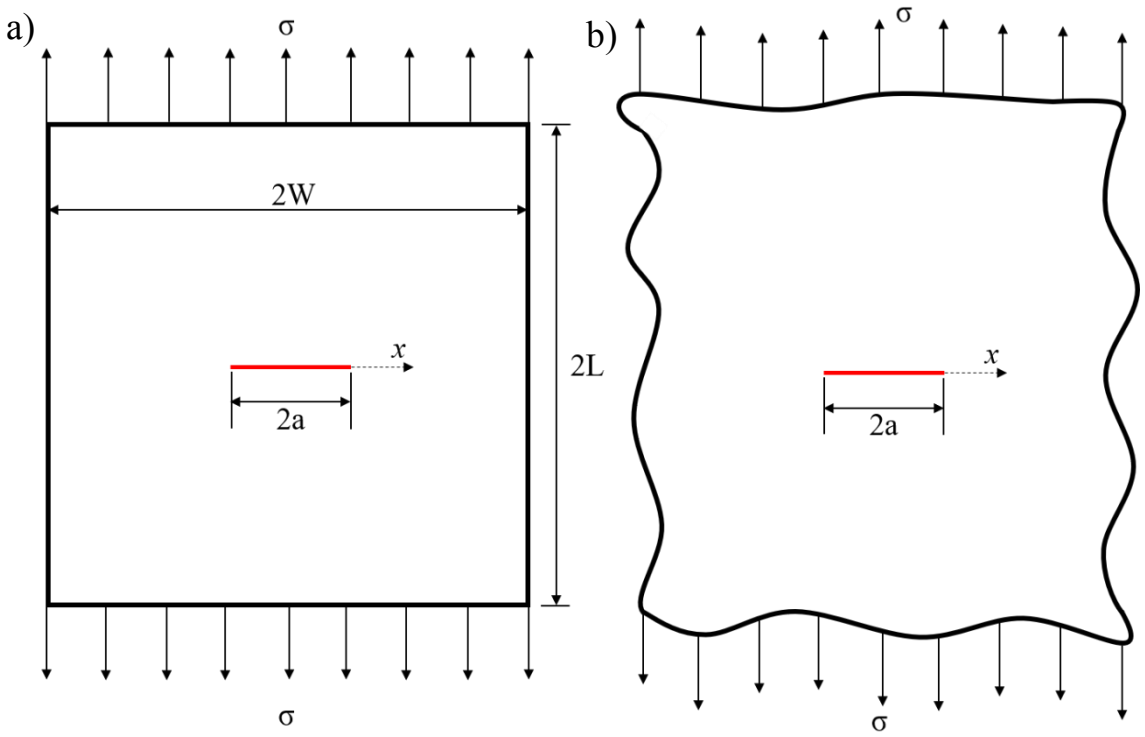

Figure 1.2. Schematics of a central crack in a two-dimensional plate of a) width $2W$ and b) infinite width, in fracture Mode I.

The general solution of the stress field in two-dimensional elastic problems leads to the Airy stress function shown in Eq. (2) [20, 21].

$$\nabla^4 \boldsymbol{\Psi} = 0 \tag{2}$$

With $\boldsymbol{\Psi}$ being a function dependent on stress field such that it satisfied the following Eq. (3).

$$\sigma_{xx} = \frac{\partial^2 \boldsymbol{\Psi}}{\partial y^2}; \quad \sigma_{yy} = \frac{\partial^2 \boldsymbol{\Psi}}{\partial x^2}; \quad \tau_{xy} = \frac{\partial^2 \boldsymbol{\Psi}}{\partial y \partial x} \tag{3}$$

Irwin argued that by knowing the stress field near the fracture surface, whether by solving the Airy stress function equations or by using stress gauges to experimentally determine the stress field, the stress intensity factor is linearly proportionate to the stress nonlinearly to the crack length [19]. The general equation of K depends on specimen geometry as well, shown in Eq. (4) as the factor $f(a/W)$, which depends on the specimen width W (See Figure 1.2.a).

$$K = \sigma \sqrt{\pi a} f\left(\frac{a}{W}\right) \tag{4}$$

For loading conditions shown in Figure 1.2.b, the stress intensity factor is expressed as in Eq. (5).

$$K_I = \sigma\sqrt{\pi a} \tag{5}$$

The stress intensity factor has been derived for other specimen configurations including but not limited to: finite plate under uniform uniaxial stress [22], edge crack in a plate under uniaxial stress [23], single-edge notch bending specimen [24], and under different Modes I, II and III.

The stress intensity factor is a fundamental parameter that characterizes the behavior of crack under linear elastic conditions. It has been shown that two cracks with the same value of K but in different structural components will behave similarly, that is, will propagate or initiate in similar rates.

1.1.3. Numerical approaches in fracture analysis

To incorporate analytical fracture mechanics into computational models, there had been a need to modify the traditional finite element method (FEM) so that it would be capable of analyzing structures with volume discontinuities. FEM as a popular method of numerically solving partial differential equations (PDEs), uses the technique of subdividing the problem domain into smaller sections called the elements. The origins of this technique go back to the works of Clough [25] and Courant [26] who used continuous functions defined over triangular domains. FEM reduces the original PDEs into a series of linear equations which weakly satisfy the original PDEs boundary conditions. Linear equations are derived per node which are points derived after meshing the problem. The node solutions are then assembled to form the overall solution of the entire system.

FEM however is cumbersome in dealing with crack propagation as with the change of crack length, remeshing is required. Moës et al [27] introduced the modified finite element method or XFEM, which used the enrichment of solution space with discontinuous functions to create a meshless solution. The enrichment is an exploitation of the partition of unity property of finite elements first identified by Melenk and Babuska [28] allowing for more degrees of freedom assigned to selected nodes at the conjunction of the growing crack.

Another attempt is to build a computational model based off of the “cohesive zone model” or CZM, which as a fracture mechanics model to simulate and analyze crack propagation and cohesive behavior in materials. A special zone is defined at the vicinity of any cracks or discontinuities called the cohesive zone. This zone has its own material properties, such as the cohesive strength, fracture toughness, and cohesive law. The cohesive strength is the stress value that the material withstands before it starts to separate, while the fracture toughness characterizes its resistance to crack propagation [29].

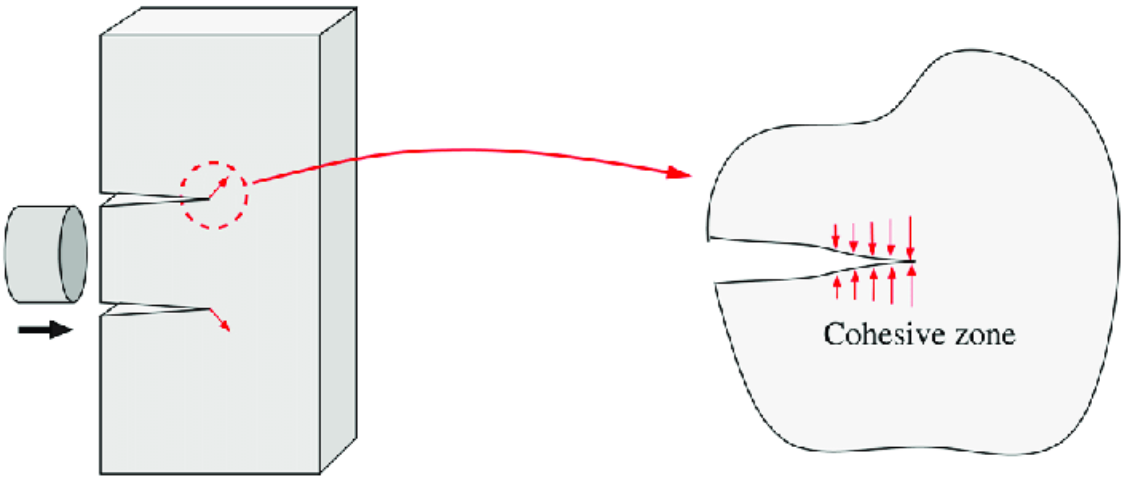

Figure 1.3. CZM schematic [29].

A cohesive law describes the behavior of CZM, which relates the separation or traction forces across the zone to the corresponding displacements or deformations. The cohesive law defines the cohesive zone behavior during crack initiation, growth, and stabilization [30].

Cohesive zone models have found application in addressing discontinuities within LEFMs and approximating nonlinear material separation phenomena [31, 32], they have also been employed to investigate a range of material failure scenarios, such as stress distribution near the crack tip in brittle materials [33], polymer crazing [34], fatigue crack growth [35], and dynamic fracture [36]. Moreover, cohesive zone models have been integrated into FEM for studying quasi-brittle materials [37].

Nonetheless, a significant drawback of the cohesive zone model lies in its strong dependence on the mesh configuration. Specifically, the accuracy of predictions made by the cohesive zone model

can be influenced by both mesh size and orientation. In cases involving extrinsic cohesive zone models, effectively managing adaptive mesh modifications is essential [38], Furthermore, representing arbitrary crack geometries and crack paths poses a challenge when employing cohesive zone models, as prior knowledge of the crack's growth trajectory is required [39].

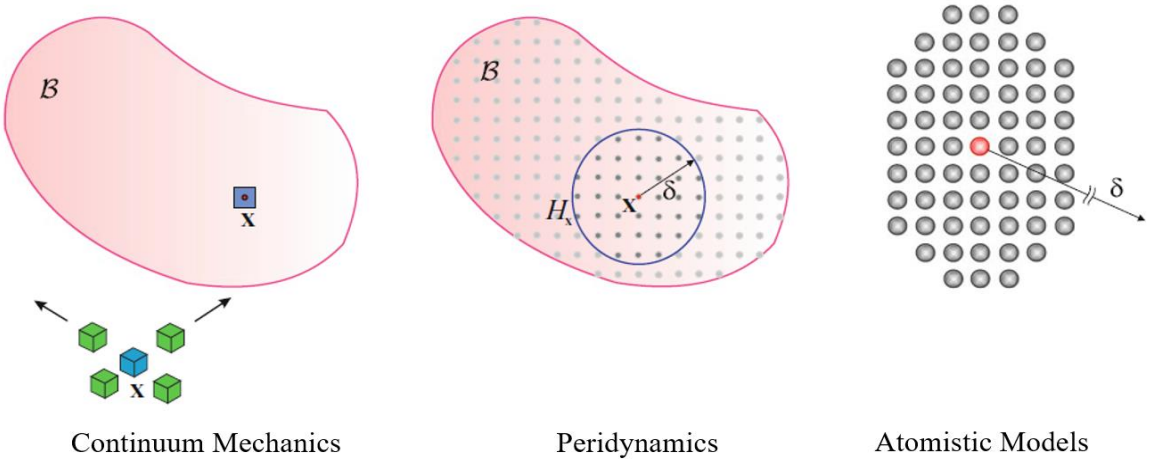

Figure 1.4. Visualization of Peridynamic model in relation to continuum mechanics models and atomistic models [40].

1.2. Peridynamics literature review

1.2.1. Peridynamics: a generalization of continuum mechanics

Peridynamics can be viewed as an extension that permits the inclusion of forces operating across distances, leading to the incorporation of a length scale within the continuum depiction of classical phenomena [41]. The conventional understanding of local stress within materials confines interactions solely to neighboring material points in immediate contact with each other. Peridynamics involves a continuum framework rooted in integral equations. These peridynamic equations take into account nonlocal force interaction between material points over a pre-defined distance limit. Material response is shaped by these nonlocal interactions, with interaction forces linked to the material's deformation within a finite local region. Conceptually, peridynamics exhibits similarities to molecular dynamics, where forces operate remotely on atoms. Peridynamic as a mathematical framework bridges the gap between atomistic models and continuum mechanics

models (See Figure 1.4). While atomistic models such as molecular dynamics, explicitly simulate the behavior of individual atoms, they are computationally intensive and are limited to relatively small spatial and temporal scales [42]. In peridynamic while individual atoms are not simulated, a non-local interaction between material points over finite distances is considered, allowing it to capture non-local effects that emerge at larger scales due to atomic interactions. On the other side of the spectrum, in continuum mechanics models, material is treated as continuous media, which while it is highly efficient for large-scale engineering simulations, microscopic level interactions are not considered [43].

1.2.2. Continuum constitutive laws and nonlocal theories

In cases involving plastic softening or damage, continuum mechanics theories encounter problems where negative tangent moduli arise, leading to imaginary wave speeds [44]. The presence of such a constitutive response in boundary value problems renders them mathematically unsound, as material softening becomes localized to an extremely small region. This challenge is addressed by introduction of a set length scale into nonlocal representation model. Nonlocal theories are classified into two types: weakly nonlocal and strongly nonlocal [44]. Weakly nonlocal theories, exemplified by strain gradient and higher-order gradient theories like the Mindlin model [45], rely on local evaluations of higher order gradients to approximate nonlocal effects. On the other hand, Peridynamics, characterized as a strongly nonlocal theory, embraces nonlocal interactions right from the start, effectively introducing a physical length scale to regularize the description of continua [46].

1.2.3. Complex dispersion and nonlocal interactions

One major difference between local and nonlocal theories is the arise of complex dispersion relation in nonlocal theories, including peridynamics. This has been shown in both weak nonlocal theories [45], such as higher order gradient theories and strong nonlocal theories, like peridynamics [47, 48]. In homogenous linearly elastic materials, the nonlocal phase velocity correlates with wave number, thus causing a complex dispersion relation (i.e. wave dispersion). This is shown to not be the case for local phase velocity, neither for pressure waves or shear waves. The proof involves a definition of an equation of motion, derivation of energy balance equation, and derivation of phase velocity equation from Fourier transformed equation of motion [47]. The

dispersion relation complexity reduces with the increase in wave number. This occurs given sufficiently small horizon size in peridynamic models [49].

1.2.4. Peridynamics approach in modeling material failure

Due to the fundamental approach and the more flexible continuity conditions, the concept of fracture and fragmentation can be naturally incorporated without the necessity of using traditional cohesive elements or similar devices, as commonly employed in classical continuum discretization methods [50]. However, this advantage comes with its own complexities, as it necessitates the inclusion of additional material behavior information, such as a failure criterion, directly into the continuous formulation.

To accurately model material degradation involving interruptions, peridynamics has been utilized for predicting damage in composites [51, 52] and layered heterogeneous materials [53]. Peridynamic has been adapted to consider irreversible damage in materials while retaining a unique solution [12]. Peridynamic has been used to simulate pitting corrosion and to understand nonlocal parameters involved in corrosion. De Meo et al. [54] showed that peridynamics can have a numerical multiphysics framework and utilized it in modeling stress-corrosion cracking induced by adsorbed hydrogen. De Meo and Oterkus [55] incorporated a peridynamics-based pitting corrosion damage model into a FEM, as discussed in [56, 57]. Jiang et al. [58] utilized peridynamics theory to thoroughly examine micro damage occurring in cemented carbide cutting tools.

The use of peridynamics has emerged as a potent approach for modeling different types of material fractures, mainly because it relies on integro-differential principles without spatial derivatives. By employing the peridynamics framework, Kilic and Madenci [59] were able to predict crack propagation in plates of grass the were prequenched. Ha et al. [60] applied a bond-based peridynamics approach to study dynamic brittle fractures. Shi [61] simulated the propagation of cracks in brittle glasses using a modified Lennard–Jones potential. To investigate brittle and ductile solids, Liu and Hong [62] utilized discretized peridynamics in combination with parallel computing. The initial exploration of dynamic fracture using peridynamics was conducted by Silling [63]. Shojaei et al. [64] integrated the finite point method with peridynamics to investigate dynamic fracture phenomena. Madenci et al. [65] studied short crack growth in isotropic materials under four-point shearing loading condition and simulated the crack path given the presence of a

miss hole in the specimen. Peridynamic is extensively used to study fracture mechanics of brittle materials [59, 60, 66] , fiber networks [67], polymers [68], concrete structures [69], and anisotropic materials [70, 71, 72]. Evangelatos and Spanos [73] introduced the use of peridynamics for stochastic fracture modeling. Recently, Vieira and Araujo [74] proposed a correspondence-based peridynamic model to model the crack growth in piezoelectric solids under complex loading conditions. Lu et al. [75] used a viscoelastic peridynamic method to study the fracture behavior of a three-point bending concrete beam with an initial crack. Xiang et al [76] studied potential mechanical damages in various anodes under severe conditions within a single-cell design subjected to thermal shocks using peridynamics.

In the field of fatigue behavior, Hu and Madenci [77] introduced presented a trans-scale model aimed at simulating crack generation and propagation based on microstructural characteristics in composites. The numerical simulations they conducted agreed with the experimental fatigue data. Zhang et al. [78] formulated a Peridynamic model for the analysis of fatigue cracking in functionally graded materials such as a two-phase composite. Recently, Wang et al [79] used a peridynamics capture the fatigue crack growth in corrosive environments.

Extensive exploration has focused on analyzing composite damage through the application of peridynamic methods. These composite materials find wide usage across various applications owing to their outstanding features such as high strength-to-weight ratios, long fatigue life, high tolerance against damage. Efforts are underway to develop efficient computational models aimed at expediting and streamlining experimental procedures, contributing to better characterization of materials behavior. Silling [80] illustrated that nonlocality in a heterogenous materials (i.e. layered composites) occur only in homogenized models, given a choice of smoothed displacement field. For the examination of the tolerance of composite laminates given any impact velocities, Sun and Huang [81] proposed a peridynamic rate-dependent equation model based on an interlayered bondage mode to account for interaction occurring at interlayers of fiber reinforced composite laminates. Using the proposed equations, they simulated low and high velocity collisions and their damage pattern in composite laminates. The results were then compared to the high velocity impact resistance of plates with isotropic properties. Kilic et al. [82] demonstrated that peridynamics can predict damage in composite laminates without the need for an assumption of lamina homogeneity. In a related study, Hu et al. [70] asserted that without the need to set any special criteria for Mode

II facture, a homogenous peridynamic model can observe multitudes of modes of failure including but not limited to: matrix-fiber-splitting fracture, matrix cracking and crack migration in the matrix.

Askari et al. [51] developed three models of peridynamic and compared their capabilities in reproducing inelastic moduli in laminate composites. It was shown bond-based peridynamics has limitation in reproducing all inelastic moduli, whereas correspondence and state-based peridynamics (SB-PD) can simulate all five moduli. Bond-based peridynamics can be improved via a coupling strategy they introduced called "morphing" which glues bond-based peridynamic to continuum mechanics. Hu et al. [83] used peridynamics to implicitly find the critical stretch in the study of delamination growth and remove the necessity of assumption of constant critical stretch. Diyaroglu et al. [84] studied the validity of peridynamics models in capturing damage propagation and nonlinear transient deformation of composites under blasts and explosions. Sadowski and Pankowski [85] developed peridynamics models to examine nanoindentation of ceramic composites. Recently, Wu and Chen [86] studied peridynamic electromechanical modeling of crack propagation in conductive composites. Hu et al. [87] presented a novel 3D micromechanical peridynamic model that can establish the correlation of microstructural features of the composites with damage mechanisms. Madenci et al. [88] used the capabilities of peridynamic in capturing material point interaction in plies and in the adjacent plies to study failure progression in fiber steered composites.

Peridynamics has found diverse applications in the in areas where continuum mechanics traditionally utilized. These applications encompass various areas such as membrane and fiber modeling [89], phase transitions [90], intergranular fracture [91], and thermal engineering [92]. Researchers have even integrated peridynamics into traditional finite element codes using beam elements [93]. Additionally, a bond-based formulation has been successfully incorporated into the molecular dynamics code LAMMPS [94]. Peridynamic formulations have demonstrated their utility in meso-scale modeling of material responses [91], suggesting that peridynamics could serve as a valuable tool for bridging length scales within a multi-scale framework.

Furthermore, bond-based peridynamic mathematical limitations has been extensively explored, including issues related to convergence [95, 96]. Notably, bond-based peridynamics converges to classical results only when the Poisson's ratio is limited to $v = 0.25$[96]. Additionally, a

correspondence has been established between strain gradient elasticity and elastic peridynamics [96]. Note that peridynamic convergence into continuum mechanic approximations hold true with the assumption of smooth displacement fields. At the vicinity of discontinuities, such as cracks, a classical modeling is not viable while peridynamics holds its validity.

The peridynamic theory was first prompted by the need for a more comprehensive model that involved discontinuities such as cracks, without a need for extra treatments, unlike in cohesive zone model and XFEM. The integral equations of peridynamic theory allows the incorporation the specimen discontinuities by developing and the circumvention of the spatial discontinuities introduced by PDEs. With the non-locality property introduced in peridynamics, it was now possible to treat complex crack propagation paths with multiple trajectories, without the need of knowing the crack growth path or any special treatments. The extent of peridynamic in simulating various modes of fracture has been studied as well, such as dynamic fracture [63, 97, 98, 99, 100, 101, 102, 103, 104] and crack propagation in isotropic materials under complex loading conditions [65].

1.2.5. Stress theory in peridynamics

Lehoucq and Silling [105] first defined a peridynamic stress tensor and explained its relation to the peridynamic force tensor. Although the research was done using a bond-based peridynamic model, the assumptions made about the pairwise-force function were arbitrary and could be relaxed, leading to a general definition of peridynamic stress tensor which could be applied in SB-PD models. Fallah et al. [106] developed used the peridynamic stress tensor defined in [105] to calculate the J-integral in the case of benchmark problem of a 2D plate with an edge crack and compared the results with the J-integral calculated using stress tensor derived by FEM.

In the case of non-ordinary SB-PD models, Warren et al. [107] used the non-local deformation gradient definition given by Silling et al. [41] and approximated the non-ordinary stress tensor using general continuum mechanics approach described by Malvern [108]. Jiang and Wang [109] implemented the same method to evaluate the stress of a multi-scale Griffith crack subjected to tensile loading. In recent years, Dipasquale et al. [110] experimented with a failure criterion for ordinary SB-PD using a calculated stress tensor. Asgari and Kouchakzadeh [111] derived von Mises stress and corresponding equivalent plastic strain in ordinary peridynamics by comparing the deviatoric energy part of the strain energy defined in peridynamic with its equivalent in

continuum mechanics. Le [112] calculated Mode-I J-integral via peridynamic stresses calculated by using peridynamics stress calculation that was originally equatied to weighted static Virial stress in [113]. Sau et al. [114] analyzed failure points of concrete structures by calculating stress in peridynamics.

1.2.6. Multi horizon peridynamics

Variable horizon peridynamics is an extension of the peridynamics framework that incorporates the concept of varying influence horizons. In standard peridynamics, the horizon is usually fixed and uniform throughout the material domain. However, in variable horizon peridynamics, the horizon can vary spatially and temporally. This enables flexible and adaptive simulation of the material behavior, especially situations where different regions of the material may exhibit different length scales or response characteristics. By allowing the horizon to vary, variable horizon peridynamics provides a means to capture localized deformation, strain gradients, and fracture initiation and propagation in a more accurate and efficient manner. It can be particularly useful in simulating materials with complex microstructures, heterogeneous materials, or problems involving large deformations and discontinuities.

Ren et al [115] proposed dual-horizon peridynamics model which uses two different horizon sizes. It was shown that the use of varied horizons can help the model to allocate more nodes to areas of interest, similar to fine meshing in FEM, allowing for a reduction in computation cost and increase in accuracy in areas of interest. Wang et al [116] reformulated dual-horizon SB-PD by way of basing the model on Euler-Lagrange equation, while also explaining the application of constraints and derivation of correction factors in dual-horizon peridynamics. The majority of numerical approaches towards peridynamic is of the explicit form. Dorduncu and Madenci [117] have developed a variable horizon peridynamic model within the FE framework that uses a combination of implicit and explicit solvers. They showed that by using an implicit solver right before crack initiation, and afterwards switching to an explicit scheme for crack initiation and propagation, there is a boost in computation cost.

1.3. Objective of study

The objective of this dissertation is to introduce a multi-horizon peridynamic model capable of accurately calculating displacement and stress components. While previous research has extensively explored single-horizon peridynamics, the realm of multi-horizon peridynamic models remains relatively unexplored. Moreover, the direct derivation of stress calculations from peridynamic constitutional laws is lacking. Therefore, this dissertation delves into the study of stress calculation through the multi-horizon peridynamic framework.

From the preceding discussion, it is deduced that peridynamic theory holds significant promise in bridging the gap between various length scales. What's more, the capability of predicting damage within peridynamic theory surpasses the realism of methods grounded in classical continuum theory, as peridynamics seamlessly incorporates material failure into the material response, without the need for external damage criteria.

In Chapter 2, the foundational principles of peridynamic theory is delved into and a novel material model capable of accommodating mechanical loadings is introduced. In this chapter, the peridynamic balance laws are introduced and compared to their continuum mechanics counterparts. Convergence of peridynamic results into continuum mechanic models with respect to the value of peridynamic horizon size is also discussed. The contexts of balance laws and convergence theories are studied through the perspectives of SB-PD and dual-horizon peridynamics.

Chapter 3 is dedicated to addressing the developing a numerical model of the peridynamic constitutive equations, and it introduces a programmable set of equations to accomplish this task. In this solution method, two methods of discretization methods of the domain of interest are introduced and briefly compared in terms of computational efficiency. The domain of interest is discretized into a set of collocation points (i.e. material points) and for each unique material points the discrete peridynamic equations are solved. The requirement of solving peridynamic differential equations, such as intial and boundary conditions, and the challenges of introducing them into the equations in the context of benchmark problems is studied. Finally, corrections such as volumetric and surface corrections of peridynamic equations in the context of two-dimensional benchmark problems are utilized. To solve for discrete peridynamic partial differential equations, explicit time integration is employed. However, it's important to note that explicit time integration comes with

the requirement of using small time steps, which can make it challenging to solve problems subjected to static or quasi-static conditions. Consequently, this chapter introduces an extension of the adaptive dynamic relaxation method initially introduced by [118]. This extension adapts the method to accommodate the intricacies of peridynamic theory.

In Chapter 4, a dual-horizon peridynamic approach to address a benchmark problem involving a two-dimensional steel plate with a central hole is implemented. This quasi-static benchmark problem serves as a critical test to evaluate the accuracy of displacement and stress component calculations in comparison to their FEM counterparts. Additionally, various discretization modes to assess the impact of material point distribution and density on the accuracy of the model is explored.

Chapter 2:

Peridynamics theory

Initially, peridynamics was conceived as a "bond-based" model, assuming a unique force density between minuscule elements of a material referred to as "material points." These points needed to be within a certain distance known as "the horizon," denoted as δ [33, 34]. These adjacent material points formed bonds in the peridynamical framework, subject to deformation under peridynamical bond forces. However, a drawback of the bond-based peridynamics was its reliance on specific Poisson's ratios, specifically $v = 0.25$ in plane strain models and $v = 0.33$ in plane stress models [34]. This limitation was attributed to inherent constraints imposed by Cauchy's relations for isotropic materials [35].

To address these shortcomings, a more encompassing peridynamics model, known as the "state-based" peridynamics, was subsequently introduced. In the SB-PD, constitutive models account for significant deformations by making bond deformation dependent on the collective deformation of neighboring bonds. The SB-PD is itself expanded into two subtypes: ordinary state-based (OSB-PD) and non ordinary state-based (NOSB-PD), with the latter representing the most generalized form of peridynamics.

In this chapter, the main focus is on studying SB-PD, as this will be the constitutive model which is used throughout the thesis. Bond-based peridynamics is briefly explained as a subset of the SB-PD.

2.1. State-based peridynamics

In a peridynamic model, a material body is subdivided into multiple material points. All material points are assigned a radius variable called the horizon, which defines a circular or spherical area centered around the material point [33, 34]. Let's consider a specific point, denoted as $\boldsymbol{x}_i$, and its associated horizon size, referred to as $\delta(\boldsymbol{x}_i)$. Any other point located within the circular region centered at $\boldsymbol{x}_i$ with a radius of $\delta(\boldsymbol{x}_i)$ is termed a "neighbor" of $\boldsymbol{x}_i$ and is represented as $\boldsymbol{x}_j$. Within

the peridynamic body designated as $\mathfrak{B}$, the collection of points surrounding $\boldsymbol{x}_i$ is referred to as $H(\boldsymbol{x}_i)$, and its precise definition is provided in Eq. (6).

$$H(\boldsymbol{x}_i) = \{\boldsymbol{x}_j - \boldsymbol{x}_i : 0 < \|\boldsymbol{x}_j - \boldsymbol{x}_i\| \leq \delta(\boldsymbol{x}_i),\ \boldsymbol{x}_j \in \mathfrak{B}\} \tag{6}$$

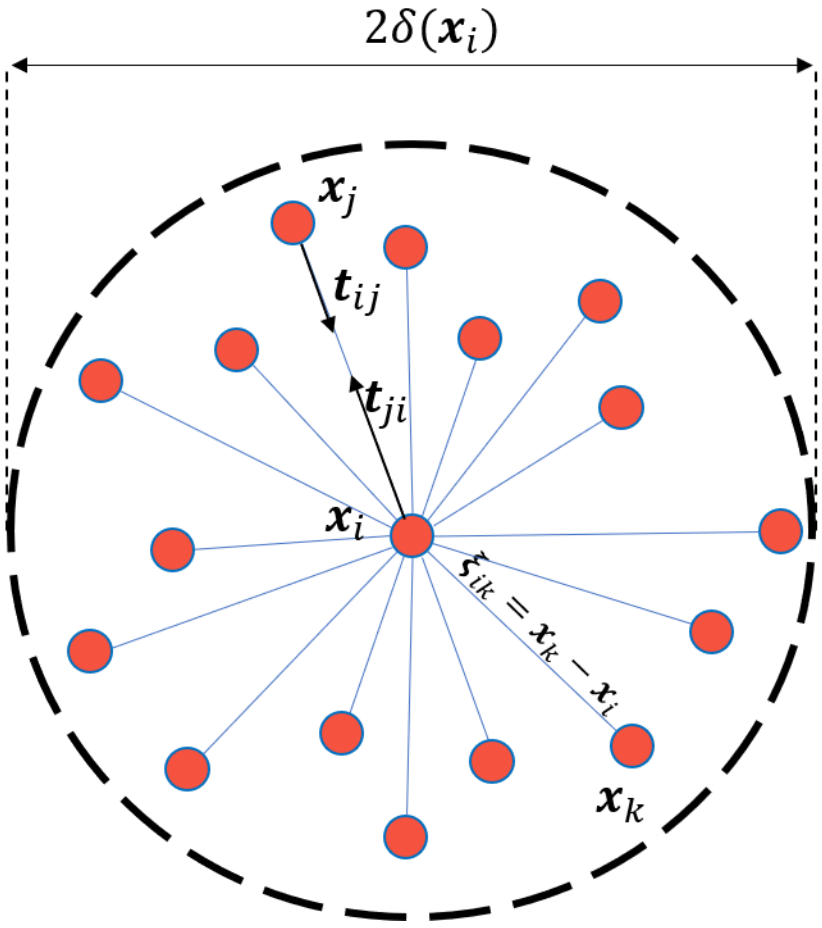

Figure 2.1. Schematic of horizon and neighbors of point $\boldsymbol{x}_i$

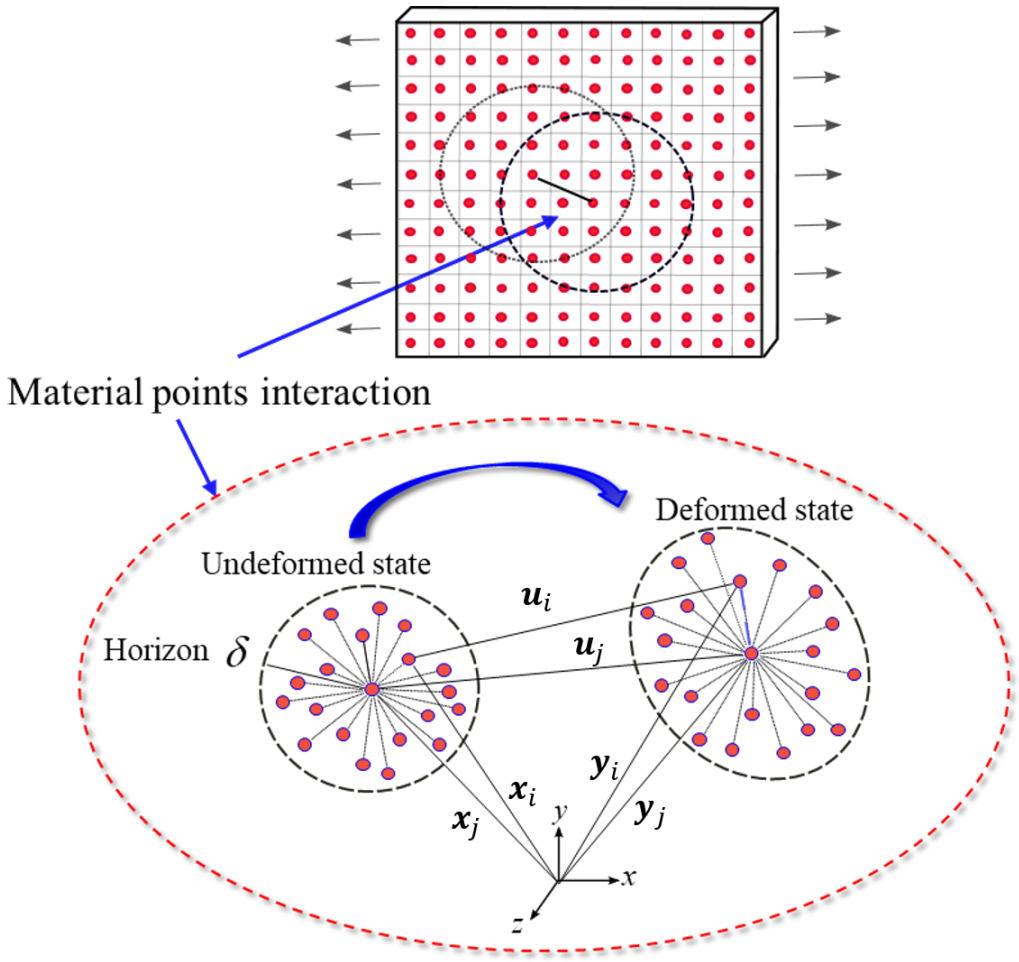

Figure 2.2. The deformed state at the vicinity of the material points $\boldsymbol{x}_i$ and $\boldsymbol{x}_j$

The initial relative position vector between two neighbors is shown as $\boldsymbol{\xi}_{ij} = \boldsymbol{x}_j - \boldsymbol{x}_i$ shown in Figure 2.1. For every material point $\boldsymbol{x}_j$, the displacement is defined as $\boldsymbol{u}_j = \boldsymbol{y}_j - \boldsymbol{x}_j$, with $\boldsymbol{y}_j$ as the coordinates of point $\boldsymbol{x}_j$ in the deformed state shown in Figure 2.2.

2.1.1. Peridynamics states

Silling [41] defines a series of infinite-dimensional arrays called vectors states (see Figure 2.3), to store and represent peridynamic constitutive relations in a compact form. The term state-based peridynamics comes from this new feature, as opposed to bond-based peridynamic, which relies simply on defining pairs of particle interactions using a bond from one material point to another.

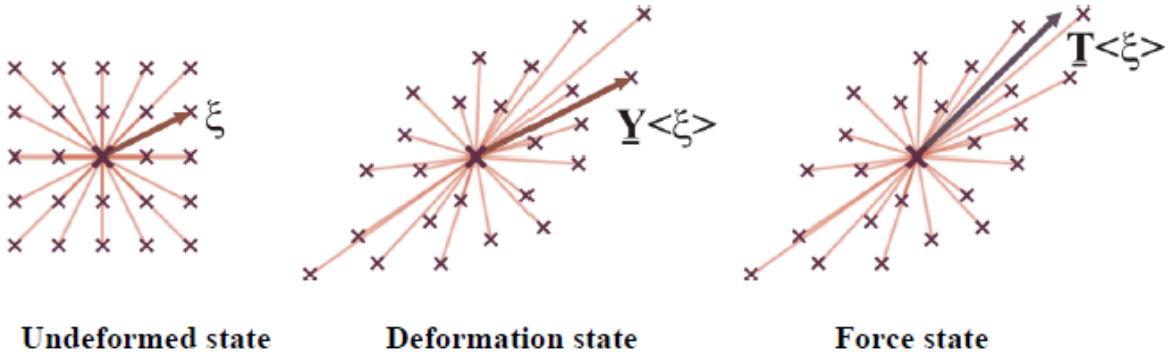

Figure 2.3. Schematic of deformations state and force state in relation to the initial relative position vector ξ [119].

A vector-state maps peridynamic bonds into real coordinate space of $\mathbb{R}^n$, with $n = 1, 2,$ or 3. The dependence of the vector-state to space $\boldsymbol{x}$ or time variable $\boldsymbol{t}$ is shown using a square-bracket.

The vector-states operate on bonds $\boldsymbol{\xi} \in H(\boldsymbol{x})$ expressed by angle brackets. Dependencies on other vector-state or other types of variables are shown using parentheses. By convention, a vector-state is shown as a capital letter with an underline such as $\underline{\boldsymbol{Y}}$ for deformation vector-state.

A vector-state $\underline{\boldsymbol{A}}[\boldsymbol{x}] \in \mathcal{V}^3(\boldsymbol{x})$ is generally defined as in Eq. (7).

$$\underline{\boldsymbol{A}}[\boldsymbol{x}]\langle\cdot\rangle : H(\boldsymbol{x}) \to \mathbb{R}^3 \tag{7}$$

Where $\mathcal{V}^3(\boldsymbol{x}) := H(\boldsymbol{x}) \times \mathbb{R}^3$ defines the vector-state space at $\boldsymbol{x}$. This definition is analogous to a tensor $\boldsymbol{A} \in \mathbb{R}^{\boldsymbol{3}} \times \mathbb{R}^{\boldsymbol{3}}$ as defined in continuum mechanics and is interpreted as a function operating on point $\boldsymbol{x}$.

The two most important vector-states defined are the deformation vector-state $\underline{\boldsymbol{Y}}$ and force vector-state $\underline{\boldsymbol{T}}$. The deformation vector-state $\underline{\boldsymbol{Y}}$ stores all the relative position vectors associated with a material point $\boldsymbol{x}$. Operating on the initial relative position vector $\boldsymbol{\xi}_{ij}$, the deformation vector-state yields

$$\underline{\boldsymbol{Y}}[\boldsymbol{x}_i, t]\langle\boldsymbol{\xi}_{ij}\rangle = \boldsymbol{y}_j - \boldsymbol{y}_i = \boldsymbol{\xi}_{ij} + \boldsymbol{u}_j - \boldsymbol{u}_i$$

Which is the deformed relative position vector. Similarly, all the force density vectors associate with space $\boldsymbol{x}$ is stored in force vector-state $\underline{\boldsymbol{T}}$. Operating on the initial relative position vector $\boldsymbol{\xi}_{ij}$, the force density vector-state yields

$$\underline{\boldsymbol{T}}[\boldsymbol{x}_i, t]\langle \boldsymbol{\xi}_{ij} \rangle = \boldsymbol{t}_{ij}$$

In terms of dependency, the force density vector-state $\underline{\boldsymbol{T}}$ depends on deformation vector-state $\underline{\boldsymbol{Y}}$, while the opposite is not true. The standard constitutive assumption of SB-PD is that the force vector-state is given by a constitutive law $\overline{\underline{\boldsymbol{T}}}$ of the form in Eq. (8).

$$\underline{\boldsymbol{T}} = \overline{\underline{\boldsymbol{T}}}(\underline{\boldsymbol{Y}}, \dot{\underline{\boldsymbol{Y}}}, \underline{\boldsymbol{q}}, \boldsymbol{q}) \tag{8}$$

In which $\boldsymbol{q}$ summarizes the internal parameters such as the body temperature and damage, and $\underline{\boldsymbol{q}}$ stands for all the internal vector-state field variables.

The principal gauge of deformation in peridynamics is the deformation vector-state, which associates each bond with its altered counterpart. A fundamental and physically grounded limitation in continuum mechanics pertains to the requirement that individual material points, as they exist in the initial reference state, must retain their uniqueness in the altered configuration. Put differently, the deformation mapping must be a one-to-one correspondence. This is mathematically expressed as Eq. (9).

$$\det(\boldsymbol{F}) > 0 \tag{9}$$

With $\boldsymbol{F}$ as deformation gradient tensor. This condition guarantees that the material density stays both positive and finite, thereby preventing the material from undergoing complete collapse or inversion to attain negative volume. Compliance with the condition of impenetrability of matter can be achieved by the condition enforced on the deformation vector-state shown in Eq.(10) [41, 120].

$$\underline{\boldsymbol{Y}}[\boldsymbol{x}]\langle \boldsymbol{\xi} \rangle \neq 0, \quad \forall \boldsymbol{\xi} \neq 0 \in H(\boldsymbol{x}), \quad \forall \boldsymbol{x} \in \mathfrak{B} \tag{10}$$

2.1.2. Balance laws

The constitutive equations of peridynamic must follow balances of linear and angular momentum, similar to equations of continuum mechanics. The principle of virtual work can be utilized to derive peridynamic constitutive equations which satisfy linear momentum balance, shown in Eq. (11).

$$\delta \int_t^{\square} (T - U)dt = 0 \tag{11}$$

This principle holds true when solved for Lagrange's equation shown in Eq. (12), with T representing the overall kinetic energy and U representing the total potential energy within the system, with Lagrangian defined as $L = T - U$.

$$\frac{d}{dt}\left(\frac{\partial L}{\partial \dot{\boldsymbol{u}}}\right) - \frac{\partial L}{\partial \boldsymbol{u}} = 0 \tag{12}$$

The kinetic and potential energies can be defined as in Eq. (13) and Eq. (14).

$$T = \sum_{i=1}^{\infty} \frac{1}{2} \rho_i \dot{\boldsymbol{u}}_i \cdot \dot{\boldsymbol{u}}_i V_i \tag{13}$$

$$U = \sum_{i=1}^{\infty} W_i V_i - \sum_{i=1}^{\infty} (\boldsymbol{b}_i \cdot \boldsymbol{u}_i) V_i \tag{14}$$

The strain energy W equals the summation of micropotentials. The interactions between two material points denoted as $\boldsymbol{x_i}$ and $\boldsymbol{x}_j$ has a micropotential denoted as w_{ij}. This micropotential is influenced by both the material properties and the stretching between point $\boldsymbol{x}_i$ and all other material points within its associated group. It's important to note that the micropotential w_{ij} is distinct from w_{ji} because w_{ij} depends on the conditions of bonds between $\boldsymbol{x}_j$ and its neighbors. These micropotentials can be represented as Eq. (15).

$$w_{ij} = f(\underline{\boldsymbol{Y}}[\boldsymbol{x_i}, \boldsymbol{t}]) \tag{15}$$

The strain energy W of material point $\boldsymbol{x_i}$ is thus defined as Eq. (16).

$$W_i = \frac{1}{2} \sum_{x_j \in H(x_i)}^{\square} \frac{1}{2} (w_{ij} + w_{ji}) V_j \tag{16}$$

By substituting the definitions of strain energy, potential energy, and kinetic energy, the Lagrangian can be defined as Eq. (17).

$$L = \sum_{i=1}^{\infty} L_i \tag{17}$$

$$L_i = \frac{1}{2}\rho_i \dot{\boldsymbol{u}}_i \cdot \dot{\boldsymbol{u}}_i V_i - \frac{1}{4} V_i \sum_{x_j \in H(x_i)} \left(w_{ij} + w_{ji}\right) V_j + \boldsymbol{b}_i \cdot \boldsymbol{u}_i V_i \tag{18}$$

Using the Eq. (18) into Eq. (12), the Lagrangian equation for $\boldsymbol{x}_i$ is simplified to Eq. (19).

$$\rho_i \ddot{\boldsymbol{u}}_i = \frac{1}{2} V_i \sum_{x_j \in H(x_i)} \left(\frac{\partial w_{ij}}{\partial(\boldsymbol{y}_j - \boldsymbol{y}_{i)}}\right) - \left(\frac{\partial w_{ji}}{\partial(\boldsymbol{y}_i - \boldsymbol{y}_{j)}}\right) + \boldsymbol{b}_i \tag{19}$$

with $\frac{\partial w_{ij}}{\partial(\boldsymbol{y}_j - \boldsymbol{y}_{i)}}$ and $\frac{\partial w_{ji}}{\partial(\boldsymbol{y}_i - \boldsymbol{y}_{j)}}$ as $\boldsymbol{t}_{ij}$ and $\boldsymbol{t}_{ji}$, respectively. Equation (19) must be valid for the conservation of linear momentum. Given the classical formation of the Lagrangian, The force densities $\boldsymbol{t}_{ij}$ and $\boldsymbol{t}_{ji}$ have to be equal to $\frac{\partial w_{ij}}{\partial(\boldsymbol{y}_j - \boldsymbol{y}_{i)}}$ and $\frac{\partial w_{ji}}{\partial(\boldsymbol{y}_i - \boldsymbol{y}_{j)}}$, respectively. This will ensure the conservation of linear momentum while setting values for peridynamic force densities.

Given the angular momentum $\boldsymbol{H}_0$ and torque $\boldsymbol{\Pi}_0$, the conservation of angular momentum is met if and only if Eq. (20) holds.

$$\dot{\boldsymbol{H}}_0 = \boldsymbol{\Pi}_0 \tag{20}$$

Given a set of particles at time t in volume V, the angular momentum is defined as in Eq. (21).

$$\boldsymbol{H}_0 = \int_V \boldsymbol{y}(\boldsymbol{x}, t) \times \dot{\boldsymbol{u}}(\boldsymbol{x}, t) \rho(\boldsymbol{x}) dV \tag{21}$$

And torque is defined as in Eq. (22).

$$\boldsymbol{\Pi}_0 = \int_V \left(\boldsymbol{y}(\boldsymbol{x}, t) \times \boldsymbol{b}(\boldsymbol{x}, t) + \int_{H(\boldsymbol{x})} \boldsymbol{y}(\boldsymbol{x}, t) \times \left(\underline{\boldsymbol{T}}[\boldsymbol{x}, t]\langle \boldsymbol{\xi} \rangle - \underline{\boldsymbol{T}}[\boldsymbol{x}', t]\langle \boldsymbol{\xi}' \rangle\right) dH\right) dV \tag{22}$$

The force densities converge to zero outside of the horizon of a material point. Thus Eq. (22) can be re-written to eliminate the limit $H(x)$ into V. Substituting into Eq. (20), one can have Eq. (23).

$$\int_V \left(\boldsymbol{y}(\boldsymbol{x}, t) \times \rho(x) \ddot{\boldsymbol{u}}(\boldsymbol{x}, t)\right) dV \;\; = \;\; \int_V \boldsymbol{y}(\boldsymbol{x}, t) \times \boldsymbol{b}(\boldsymbol{x}, t) dV \tag{23}$$

$$+ \int_V \int_V \boldsymbol{y}(\boldsymbol{x},t) \times \underline{\boldsymbol{T}}[\boldsymbol{x},t]\langle\boldsymbol{\xi}\rangle dV' dV$$

$$- \int_V \int_V \boldsymbol{y}(\boldsymbol{x}',t) \times \underline{\boldsymbol{T}}[\boldsymbol{x}',t]\langle\boldsymbol{\xi}'\rangle dV' dV$$

To use the vector-state notation, the subtraction shown in Eq. (23) can be shows to reduce to Eq. (24).

$$\boldsymbol{y}(\boldsymbol{x}',t) - \boldsymbol{y}(\boldsymbol{x},t) = \underline{\boldsymbol{Y}}[\boldsymbol{x},t]\langle\boldsymbol{x}' - \boldsymbol{x}\rangle \tag{24}$$

The elimination of the limit $H(x)$ allows to show Eq. (25) via a change of parameter.

$$\int_V \int_V \boldsymbol{y}(\boldsymbol{x},t) \times \underline{\boldsymbol{T}}[\boldsymbol{x},t]\langle\boldsymbol{\xi}\rangle dV' dV = \int_V \int_V \boldsymbol{y}(\boldsymbol{x}',t) \times \underline{\boldsymbol{T}}[\boldsymbol{x}',t]\langle\boldsymbol{\xi}'\rangle dV dV' \tag{25}$$

With integration limited only to the horizon, substitution of Eq. (24) and Eq. (25) into Eq. (23) leads to Eq. (26) as the final form.

$$\int_V (\boldsymbol{y}(\boldsymbol{x},t) \times (\rho(x)\ddot{\boldsymbol{u}}(\boldsymbol{x},t) - \boldsymbol{b}(\boldsymbol{x},t)))dV = \int_V \int_H \left(\underline{\boldsymbol{Y}}[\boldsymbol{x},t]\langle\boldsymbol{x}' - \boldsymbol{x}\rangle \times \underline{\boldsymbol{T}}[\boldsymbol{x},t]\langle\boldsymbol{x}' - \boldsymbol{x}\rangle\right) dH dV \tag{26}$$

2.1.3. Initial and boundary conditions

The force densities introduced in the SB-PD are the counterparts of surface tractions in continuum mechanics, except that they operate on a volumetric basis. The difference can be shown in the problem of calculating the internal forces of a body under external loads. An internal force is defined as the that exerted by one region of the body to another adjacent region. In other words, if

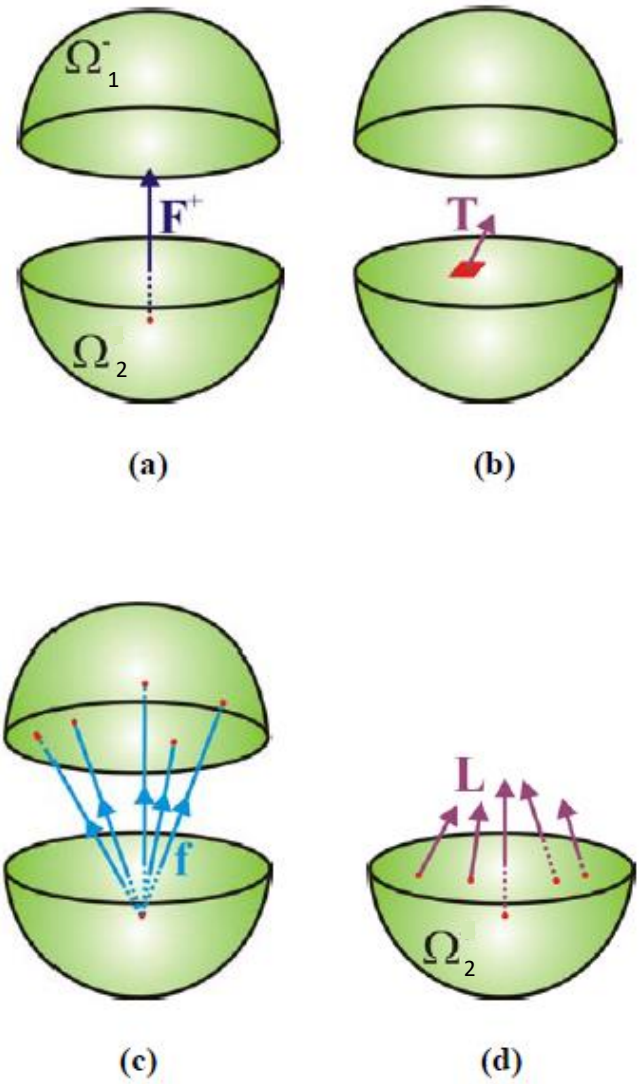

Figure 2.4. Comparison of continuum mechanics and peridynamic forces: (a) Total force applied on a point in Ω_2 from region Ω_1, (b) Tractions in continuum mechanics, (c) Peridynamic force densities acting on a point in Ω_2 from Ω_1, (d) Peridynamic force densities acting on Ω_2 due to Ω_1 [103].

body $\mathfrak{B}$ is divided into two regions Ω_1 and Ω_2, there must be an internal force applied from region Ω_1 onto region Ω_2 and vice versa.

In classical continuum mechanics, this internal force termed as F, is measured by an integration of surface traction of region Ω_1 over its cross-sectional area, $\partial\Omega$, as shown in Eq. (27).

$$\boldsymbol{F} = \int_{\partial\Omega} \boldsymbol{T} dA \tag{27}$$

With $\boldsymbol{T}$ as surface traction. In the peridynamic theory, the integration will turn from a surface integration into a volumetric integration, as the interaction of the two regions is extended over the cross section to the maximum depth of the horizon size used in the model. The volumetric integration is shown in Eq. (28).

$$\boldsymbol{F} = \iint_{\Omega_1\Omega_2} \underline{\boldsymbol{T}}[\boldsymbol{x}, t]\langle \boldsymbol{x} - \boldsymbol{x}' \rangle - \underline{\boldsymbol{T}}[\boldsymbol{x}', t]\langle \boldsymbol{x}' - \boldsymbol{x} \rangle dV_{\Omega_2} dV_{\Omega_1} \tag{28}$$

With $\boldsymbol{x}$ and $\boldsymbol{x}'$ belonging to regions Ω_1 and Ω_2, respectively. As stated previously, parameter body force density $\boldsymbol{b}$ stands for all external loads applied in the peridynamic equation of motion. Boundary conditions is then introduced by presetting a displacement or a velocity of the material points forming the boundary layer.

2.1.4. State-based peridynamics force density

The deformation on one material point at location $\boldsymbol{x}_i$ is dependent on the total displacement of its neighbor points; that is, material points that are members of $H(\boldsymbol{x}_i)$. As stated previously, in SB-PD, vector-state $\underline{\boldsymbol{T}}$ can be prompted to output the force density applied by $\boldsymbol{x}_j$ on $\boldsymbol{x}_i$ as $\underline{\boldsymbol{T}}[\boldsymbol{x}_i, t]\langle \boldsymbol{x}_j - \boldsymbol{x}_i \rangle$.

Given the requirements for the conservation of linear momentum, the state-based force density is dependent on the partial differentiation of the strain energy density W with respect to the relative position vector $\boldsymbol{\xi} + \boldsymbol{\eta}$ (Eq. (29)).

$$\underline{\boldsymbol{T}}[\boldsymbol{x}_i, t]\langle \boldsymbol{x}_j - \boldsymbol{x}_i \rangle \sim \frac{1}{V} \frac{\partial W(\boldsymbol{x})}{\partial(|\boldsymbol{\xi} + \boldsymbol{\eta}|)} \frac{\boldsymbol{\xi} + \boldsymbol{\eta}}{|\boldsymbol{\xi} + \boldsymbol{\eta}|} \tag{29}$$

With W defined as the same in classical continuum mechanics shown in Eq. (30).

$$W = \frac{K}{2}\theta^2 + \frac{1}{4\mu}\sum_{i=1}^{3}\sigma_{ii}^2 + \frac{1}{2\mu}(\tau_{12}^2 + \tau_{13}^2 + \tau_{23}^2) - \frac{3K^2}{4\mu}\theta^2 \tag{30}$$

With θ as the dilatation term. All influence emanating from neighboring points is summarized in the dilatation term [40]. In the denominator, the shear modulus is equal to $\mu = \frac{E}{2(1+\nu)}$ given

Poisson's ratio as ν and Young's modulus as E. In order to relate force densities to the strain energy density, Cauchy stress components need to be defined based on force densities, shown in Eq. (31) by Madenci [40].

$$\sum_{i=1}^{3} \sigma_{ij}^2 = \sum_{\square}^{\square} 4\boldsymbol{t} \cdot \boldsymbol{t}|\boldsymbol{\xi}|V^2 \tag{31}$$

Equation (32) is derived with the substitution of Eq. (30) and Eq. (31) into Eq. (29).

$$\underline{\boldsymbol{T}}[\boldsymbol{x_i}, t]\langle \boldsymbol{x_j} - \boldsymbol{x_i} \rangle = \frac{2\delta}{|\boldsymbol{\xi}_{ij}|}\left(d\alpha\theta + \beta s_{ij}\right)\frac{\boldsymbol{\xi}_{ij} + \boldsymbol{\eta}_{ij}}{|\boldsymbol{\xi}_{ij} + \boldsymbol{\eta}_{ij}|} \tag{32}$$

With parameters d, α, and β as peridynamic parameters which are constant for all material points given a constant horizon size. For a two-dimensional body, these parameters are defined as in Eq. (33).

$$\alpha = \frac{1}{2}(K - 2\mu) \quad , \quad \beta = \frac{6\mu}{\pi h \delta^4} \quad , \quad d = \frac{2}{\pi h \delta^3} \tag{33}$$

The dilatation term in its general form is shown in Eq. (34).

$$\theta = \sum_{x' \in H(x)} \frac{ws(\boldsymbol{\xi} + \boldsymbol{\eta})}{|\xi + \eta|} \cdot \boldsymbol{\xi} V' \tag{34}$$

Equations (33) and (34) are then substituted into Eq. (32) to yield the force density in an SB-PD model.

Finally, for an SB-PD model, the equation of motion is defined as in Eq. (35).

$$p\ddot{\boldsymbol{u}}(\boldsymbol{x}_i, t) = \int_{H(\boldsymbol{x}_i)} (\underline{\boldsymbol{T}}[\boldsymbol{x}_i, t]\langle \boldsymbol{x}_j - \boldsymbol{x}_i \rangle - \underline{\boldsymbol{T}}[\boldsymbol{x}_j, t]\langle \boldsymbol{x}_i - \boldsymbol{x}_j \rangle)\, dV_{\boldsymbol{x}_j} + \boldsymbol{b}(\boldsymbol{x}_i, t) \tag{35}$$

2.2. Ordinary peridynamics

A peridynamic material model is ordinary if Eq. (36) is satisfied for all material points.

$$\underline{\boldsymbol{T}}\langle \boldsymbol{\xi} \rangle \times \underline{\boldsymbol{Y}}\langle \boldsymbol{\xi} \rangle = 0, \quad \forall \boldsymbol{\xi} \in H \tag{36}$$

This stipulation states that the force direction is parallel to the deformation direction, ensuring the adherence to the angular momentum rule. For elastic materials, this means that the elastic energy can be calculated by knowing the deformed relative position vector-state (i.e. distances after

deformation). It has been shown that typical peridynamic materials can accurately portray nonlocal isotropic elasticity. [41], as well as nonlocal isotropic plasticity [121].

2.3. Bond-based peridynamics

Bond-based peridynamics is the original format of the peridynamic theory first proposed by Silling [122] can be seen as a subset of SB-PD. In this case, the force density vectors $\underline{\boldsymbol{T}}[\boldsymbol{x}_i, \boldsymbol{t}]\langle \boldsymbol{x}_j - \boldsymbol{x}_i \rangle$ and $\underline{\boldsymbol{T}}[\boldsymbol{x}_j, t]\langle \boldsymbol{x}_i - \boldsymbol{x}_j \rangle$ are equal in magnitude, parallel, and opposite in direction (i.e. Eq. (37)). For conservation of angular momentum, all force density vectors are also parallel to their respective relative position vectors or $\underline{\boldsymbol{Y}}[\boldsymbol{x}_i, t]\langle \boldsymbol{x}_j - \boldsymbol{x}_i \rangle$.

$$\underline{\boldsymbol{T}}[\boldsymbol{x}_i, t]\langle \boldsymbol{x}_j - \boldsymbol{x}_i \rangle = -\underline{\boldsymbol{T}}[\boldsymbol{x}_j, t]\langle \boldsymbol{x}_i - \boldsymbol{x}_j \rangle = \frac{1}{2}\boldsymbol{f} \tag{37}$$

The constitutive equation of motion of point $\boldsymbol{x}_i$ in bond-based peridynamic is defined as Eq. (38).

$$\rho(\boldsymbol{x})\ddot{\boldsymbol{u}}(\boldsymbol{x}, t) = \int_{H(\boldsymbol{x})} \boldsymbol{f} dH + \boldsymbol{b}(\boldsymbol{x}, t) \tag{38}$$

With $\boldsymbol{f}$ being the pair-wise force density which is dependent on the initial relative position vector $\boldsymbol{\xi}$ and deformed relative position vector $\boldsymbol{\xi} + \boldsymbol{\eta}$. Silling [122] defined the pair-wide force density along with its properties.

To follow the rule of reaction per force interaction, the pairwise force exerted by material point $\boldsymbol{x}$ unto $\boldsymbol{x}'$ has to be equal to the pairwise force exerted by material point $\boldsymbol{x}'$ unto $\boldsymbol{x}$ as shown in Eq. (39).

$$\boldsymbol{f}(-\boldsymbol{\xi}, -\boldsymbol{\eta}) = -\boldsymbol{f}(\boldsymbol{\xi}, \boldsymbol{\eta}) \tag{39}$$

Another limitation comes from the angular momentum shown in Eq. (40), forcing the pairwise force density to be in the parallel to the deformed position vector $\boldsymbol{\xi} + \boldsymbol{\eta}$.

$$(\boldsymbol{\xi} + \boldsymbol{\eta}) \times \boldsymbol{f}(\boldsymbol{\xi}, \boldsymbol{\eta}) = 0 \quad \forall \boldsymbol{\eta}, \boldsymbol{\xi}. \tag{40}$$

For a microelastic material without memory with constant temperature, the pairwise force density is linearly correspondant to the bond stretch of two material points, shown in Eq. (41).

$$\boldsymbol{f}(\boldsymbol{\xi}, \boldsymbol{\eta}) = \frac{Cs(\boldsymbol{\xi}, \boldsymbol{\eta})(\boldsymbol{\xi} + \boldsymbol{\eta})}{|\boldsymbol{\xi} + \boldsymbol{\eta}|} \tag{41}$$

With stretch being defined as in Eq. (42).

$$s(\boldsymbol{\xi}, \boldsymbol{\eta}) = \frac{|\boldsymbol{\xi} + \boldsymbol{\eta}| - |\boldsymbol{\xi}|}{|\boldsymbol{\xi}|} \tag{42}$$

Based on the findings of [123], the constant C in Eq. (41) is equal to that in Eq. (43).

$$C = \frac{18K}{\pi\delta^4} \tag{43}$$

With K as bulk modulus.

2.4. Dual-horizon peridynamics

One fundamental limitation in traditional peridynamic formulations is the requirement for constant horizon radii. Failure to maintain constant horizon sizes can lead to unwanted wave reflections and the introduction of erroneous forces between material points, thereby compromising the accuracy of results. Nevertheless, in many practical applications, there is a need to adaptively adjust the sizes of horizons based on the spatial distribution of material points, such as for the purpose of computational efficiency, adaptive refinement, and multiscale modeling.

In the original peridynamic models, it is crucial to set the horizon radius according to the local resolution required by the material points with the lowest resolution. When a multitude of horizon sizes is introduced to the model without consideration of its effect on the constitutive peridynamic assumption, the problem of "spurious wave reflections" occurs [124]. A review and modification of consttitutive peridynamic equations has led to a novel approach known as dual-horizon peridynamics (DH-PD) [124]. The central concept behind DH-PD involves defining two horizons per material point, with one being essentially complementary to the original horizon.

Using DH-PD, it becomes possible to derive the traditional peridynamics with constant horizon values, without the need for additional techniques such as variational principles or Taylor expansions, as required in other methods [125]. Notably, DH-PD enables the usage of multiple horizon sizes as needed, leading to a reduction in computation cost by limiting computationally intensive calculations to areas of interest. DH-PD multi-horizon capabilities are similar to how various mesh sizes can be used in traditional methods such as FEM or Finite Volume Method (FVM).

2.4.1. Horizon and dual horizon set

In DH-PD a concept of 'dual horizon' has to be introduced adjacent to the previous definition of 'horizon' in peridynamics. As was originally stated, The neighbors $H(\boldsymbol{x}_i)$ is a set of all the

material points that are within the horizon of the material point $\boldsymbol{x}_i$, as stated in Eq. (6), repeated below for convenience.

$$H(\boldsymbol{x_i}) = \{\boldsymbol{x}_j - \boldsymbol{x}_i : 0 < \|\boldsymbol{x}_j - \boldsymbol{x}_i\| \leq \delta(\boldsymbol{x}_i),\ \boldsymbol{x}_j \in \mathfrak{B}\}$$

All neighbors of material point $\boldsymbol{x}_i$ exert a force density $\boldsymbol{f}_{ij}$, which is equal to the pairwise force density $\boldsymbol{f}$ when using a bond-based peridynamics model and equal to $\underline{\boldsymbol{T}}[\boldsymbol{x_i}, t]\langle \boldsymbol{x}_i - \boldsymbol{x}_j \rangle$ or $\boldsymbol{t}_{ij}$ in

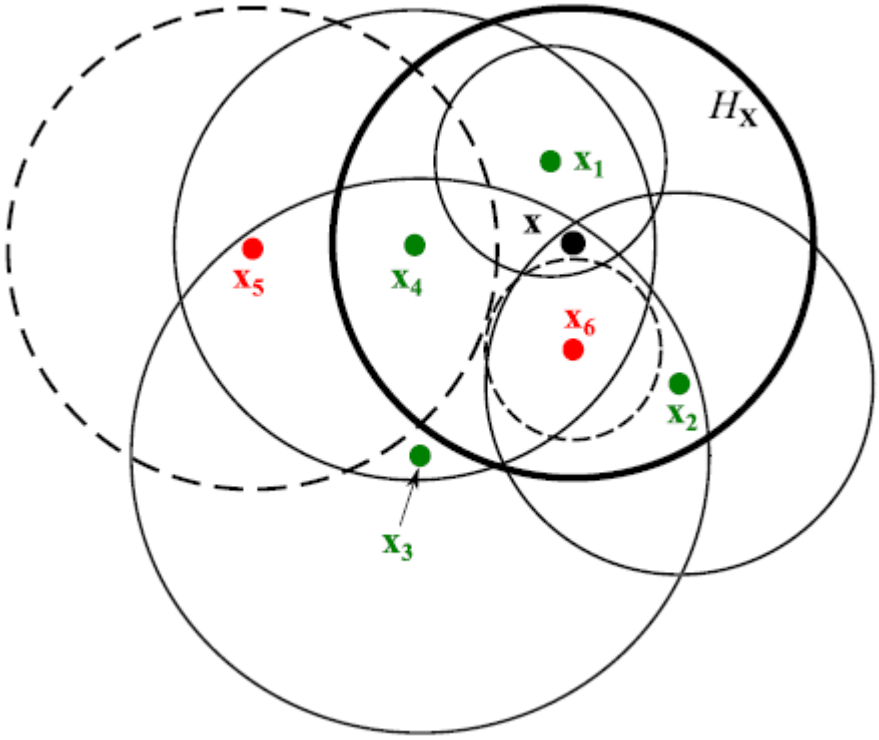

Figure 2.5. A schematic of horizon and dual horizon sets in a multi-horizon peridynamic model.

SB-PD. Based on Newton's third law of motion, there will be a reactionary force applied to the neighbor $\boldsymbol{x}_j$ due to this peridynamic force density. Note that in this definition, there is no implicit assumption that $\boldsymbol{x_i}$ is a neighbor of $\boldsymbol{x}_j$, only that $\boldsymbol{x}_j$ is a neighbor of $\boldsymbol{x_i}$. The constituent assumption of neighborhood mutuality no longer applies in DH-PD. Nevertheless, the reaction force density has to be taken into account. This is done by the introduction of the dual horizon set, which compliments the original horizon set $H(\boldsymbol{x}_i)$.

The dual horizon $H'(\boldsymbol{x}_i)$ is a set of all the material points whose neighborhood includes material point $\boldsymbol{x_i}$. In other words, the set of all material points that 'see' material point $\boldsymbol{x_i}$, regardless of whether the opposite is true. Figure 2.5 shows a schematic of horizon and dual horizon sets and their difference. In this figure, points $\boldsymbol{x}_1$, $\boldsymbol{x}_2$, $\boldsymbol{x}_4$ and $\boldsymbol{x}_3$ see point $\boldsymbol{x}$ and are part of its dual horizon set, or $H'(\boldsymbol{x}) = \{\boldsymbol{x}_1, \boldsymbol{x}_2, \boldsymbol{x}_3, \boldsymbol{x}_4\}$. Points $\boldsymbol{x}_5$ and $\boldsymbol{x}_6$ do not see point $\boldsymbol{x}$. members of point $\boldsymbol{x}$ horizon set are $H(\boldsymbol{x}) = \{\boldsymbol{x}_1, \boldsymbol{x}_2, \boldsymbol{x}_4, \boldsymbol{x}_6\}$. If material point $\boldsymbol{x}_k \in H'(\boldsymbol{x}_i)$, there is a peridynamic force $\boldsymbol{f}_{ki}$ applied over $\boldsymbol{x}_k$ by $\boldsymbol{x}_i$. Newton's third law of motion requires an existence of reactionary force of equal magnitude in the opposite direction applied over $\boldsymbol{x_i}$. A 'shape' can also be assigned to horizon and dual-horizon sets, which is the area or volume containing the members of the set. While the shape of the $H(\boldsymbol{x}_i)$ is a circle around the $\boldsymbol{x}_i$, the shape of the dual horizon $H'(\boldsymbol{x_i})$ is circular if and only if the horizon sizes of material points in $H'(\boldsymbol{x_i})$ are equal to that of $\boldsymbol{x}_i$.

The distinction between the dual horizon set and the horizon set is useful in finding the equation of motion in DH-PD, but it is worth noting that no new bonds were introduced in DH-PD, rather, the existing peridynamic bonds between material points were regrouped by new definitions into two sets of horizon and dual horizon. It is seen in the coming sections that the dual horizon set vanishes from the angular momentum and linear momentum balance laws, keeping the equilibrium of the body intact. Also, The DH-PD does not alter the nature of peridynamic bonds, so a DH-PD model can either be bond-based, state-based, or oridnary and non-ordinary. An ordinary state-based DH-PD model is set as the default model used in the rest of this dissertation

Equation (44) is includes the dual horizon set in the definition of state-based force density.

$$\underline{\boldsymbol{T}}[\boldsymbol{x}_i, t]\langle \boldsymbol{x}_j - \boldsymbol{x}_i \rangle \neq 0, \quad if\ \boldsymbol{x}_j \in H(\boldsymbol{x}_i)\ \ or\ \boldsymbol{x}_i \in H'(\boldsymbol{x}_j) \tag{44}$$

For any region Ω, the net internal force can be calculated by summing up the force densities via two approaches [126]. The first approach is to iterate through every horizon set and is shown as in Eq. (45).

$$\boldsymbol{F} = \sum_{\boldsymbol{x}_i \in \Omega} \left(\sum_{\boldsymbol{x}_j \in H(\boldsymbol{x}_i)} \underline{\boldsymbol{T}}[\boldsymbol{x}_i, t]\langle \boldsymbol{x}_j - \boldsymbol{x}_i \rangle dV_{\boldsymbol{x}_j} \right) dV_{\boldsymbol{x}_i} \tag{45}$$

The second approach is to iterate through every dual horizon set shown in Eq. (46).

$$\boldsymbol{F} = -\sum_{\boldsymbol{x}_i \in \Omega} \left(\sum_{\boldsymbol{x}_j \in H'(\boldsymbol{x}_i)} -\underline{\boldsymbol{T}}[\boldsymbol{x}_j, t]\langle \boldsymbol{x}_i - \boldsymbol{x}_j \rangle dV_{\boldsymbol{x}_j} \right) dV_{\boldsymbol{x}_i} \tag{46}$$

Note that the reactionary forces must be considered in calculating the net internal force. Comparing the two equations yields Eq. (47).

$$\begin{aligned} &\sum_{\boldsymbol{x}_i \in \Omega} \left(\sum_{\boldsymbol{x}_j \in H(\boldsymbol{x}_i)} \underline{\boldsymbol{T}}[\boldsymbol{x}_i, t]\langle \boldsymbol{x}_j - \boldsymbol{x}_i \rangle dV_{\boldsymbol{x}_j} \right) dV_{\boldsymbol{x}_i} \\ &\qquad = \sum_{\boldsymbol{x}_i \in \Omega} \left(\sum_{\boldsymbol{x}_j \in H'(\boldsymbol{x}_i)} -\underline{\boldsymbol{T}}[\boldsymbol{x}_j, t]\langle \boldsymbol{x}_i - \boldsymbol{x}_j \rangle dV_{\boldsymbol{x}_j} \right) dV_{\boldsymbol{x}_i} \end{aligned} \tag{47}$$

Equation (47) allows the elimination of the dual horizon set in angular momentum and linear momentum balance laws.

2.4.2. Equation of motion in dual horizon peridynamics

Similar to the equation of motion in single horizon peridynamics, the net total force applied on a material point is used to find the displacement. In state-based DH-PD, given a neighbor particle called $\boldsymbol{x}_j$ for a material point $\boldsymbol{x}_i$, a force density of $\underline{\boldsymbol{T}}[\boldsymbol{x}_i, t]\langle \boldsymbol{x}_j - \boldsymbol{x}_i \rangle$ exists. The force vector $\tilde{\boldsymbol{f}}_{ij}(\boldsymbol{\xi}_{ij}, \boldsymbol{\eta}_{ij})$ is defined as in Eq. (48).

$$\tilde{\boldsymbol{f}}_{ij}(\boldsymbol{\xi}_{ij}, \boldsymbol{\eta}_{ij}) \coloneqq \underline{\boldsymbol{T}}[\boldsymbol{x}_i, t]\langle \boldsymbol{x}_j - \boldsymbol{x}_i \rangle \cdot \Delta V_{\boldsymbol{x}_i} \cdot \Delta V_{\boldsymbol{x}_j} \tag{48}$$

With $\Delta V_{\boldsymbol{x}_i}$ denoting the volume associated with $\boldsymbol{x}_i$. Note that the unit of $\underline{\boldsymbol{T}}[\boldsymbol{x}_i, t]\langle \boldsymbol{x}_j - \boldsymbol{x}_i \rangle$ is force per volume squared. Summation of Eq. (48) over all the neighbors of $\boldsymbol{x}_i$ yields the net direct peridynamical force applied to $\boldsymbol{x}_i$.

For every material point $\boldsymbol{x}_k \in H'(\boldsymbol{x}_i)$, there exists a force density $\underline{\boldsymbol{T}}[\boldsymbol{x}_k, t]\langle \boldsymbol{x}_i - \boldsymbol{x}_k \rangle$ which is applied to $\boldsymbol{x}_k$. The reaction of this force density, $-\underline{\boldsymbol{T}}[\boldsymbol{x}_k, t]\langle \boldsymbol{x}_i - \boldsymbol{x}_k \rangle$, is applied to $\boldsymbol{x}_i$. The force vector associated with this force density felt by $\boldsymbol{x}_k$ is defined in Eq. (49).

$$\tilde{\boldsymbol{f}}(\boldsymbol{\xi}_{ki}, \boldsymbol{\eta}_{ki}) \coloneqq \underline{\boldsymbol{T}}[\boldsymbol{x}_k, t]\langle \boldsymbol{x}_i - \boldsymbol{x}_k \rangle \cdot \Delta V_{\boldsymbol{x}_k} \cdot \Delta V_{\boldsymbol{x}_i} \tag{49}$$

The reaction to the force of Eq. (49) is applied to $\boldsymbol{x}_i$ and is equal to $-\tilde{\boldsymbol{f}}(\boldsymbol{\xi}_{ki}, \boldsymbol{\eta}_{ki})$ or $-\tilde{\boldsymbol{f}}(-\boldsymbol{\xi}_{ik}, -\boldsymbol{\eta}_{ik})$. Summation of Eq. (49) over all the members of $H'(\boldsymbol{x}_i)$ yields the net reactionary

peridynamical force applied to $\boldsymbol{x}_i$. The governing equation of motion in a state-based DH-PD model over $\boldsymbol{x}_i$ is thus surmised as in Eq. (50).

$$\rho\ddot{\boldsymbol{u}}(\boldsymbol{x}_i,t)\Delta V_{\boldsymbol{x}_i}=\sum_{\boldsymbol{x}_j\in H(\boldsymbol{x}_i)}\tilde{\boldsymbol{f}}_{ij}\left(\boldsymbol{\xi}_{ij},\boldsymbol{\eta}_{ij}\right)-\sum_{\boldsymbol{x}_k\in H'(\boldsymbol{x}_i)}\tilde{\boldsymbol{f}}(-\boldsymbol{\xi}_{ik},-\boldsymbol{\eta}_{ik})+\boldsymbol{b}(\boldsymbol{x}_i,t)\Delta V_{\boldsymbol{x}_i} \quad (50)$$

With $\boldsymbol{b}(\boldsymbol{x}_i,t)$ as body force density applied to $\boldsymbol{x}_i$ with a unit of force per volume. Substituting equations (48) and (49) into Eq. (50) and dividing the two sides by $\Delta V_{\boldsymbol{x}_i}$, one can have the get Eq. (51).

$$\begin{aligned}\rho\ddot{\boldsymbol{u}}(\boldsymbol{x}_i,t)=&\sum_{\boldsymbol{x}_j\in H(\boldsymbol{x}_i)}\underline{\boldsymbol{T}}[\boldsymbol{x}_i,t]\langle\boldsymbol{x}_j-\boldsymbol{x}_i\rangle\cdot\Delta V_{\boldsymbol{x}_j}\\&-\sum_{\boldsymbol{x}_k\in H'(\boldsymbol{x}_i)}\underline{\boldsymbol{T}}[\boldsymbol{x}_k,t]\langle\boldsymbol{x}_i-\boldsymbol{x}_k\rangle\cdot\Delta V_{\boldsymbol{x}_k}+\boldsymbol{b}(\boldsymbol{x}_i,t)\end{aligned} \quad (51)$$

Equation (51) is the governing equation of motion of $\boldsymbol{x}_i$ in the discretized form. By refining the discretization volume so that $\Delta V_{\boldsymbol{x}_i}\to 0$, the integral form of the equation of motion is equal to Eq. (52).

$$\rho\ddot{\boldsymbol{u}}(\boldsymbol{x},t)=\int_{\boldsymbol{x}'\in H(\boldsymbol{x})}\underline{\boldsymbol{T}}[\boldsymbol{x},t]\langle\boldsymbol{x}'-\boldsymbol{x}\rangle dV_{\boldsymbol{x}'}-\int_{\boldsymbol{x}'\in H'(\boldsymbol{x})}\underline{\boldsymbol{T}}[\boldsymbol{x}',t]\langle\boldsymbol{x}-\boldsymbol{x}'\rangle dV_{\boldsymbol{x}'}+\boldsymbol{b}(\boldsymbol{x},t) \quad (52)$$

By setting a constant horizon, one will have $H(\boldsymbol{x})=H'(\boldsymbol{x})$ and Eq. (52) collapses into the equation of motion governing a state-based single horizon shown in Eq. (53).

$$\rho\ddot{\boldsymbol{u}}(\boldsymbol{x},t)=\int_{\boldsymbol{x}'\in H(\boldsymbol{x})}\underline{\boldsymbol{T}}[\boldsymbol{x},t]\langle\boldsymbol{x}'-\boldsymbol{x}\rangle-\underline{\boldsymbol{T}}[\boldsymbol{x}',t]\langle\boldsymbol{x}-\boldsymbol{x}'\rangle dV_{\boldsymbol{x}'}+\boldsymbol{b}(\boldsymbol{x},t) \quad (53)$$

Which is exactly equal to Eq. (35).

2.4.3. Balance of linear momentum in dual horizon peridynamics

The conservation of linear momentum requires that the sum of the internal forces of a closed system (i.e. the peridynamic body of $\mathfrak{B}$) be equal to zero if the net external force is zero. Thus Eq. (54) must hold.

$$\sum_{\boldsymbol{x}_i\in\mathfrak{B}}\sum_{\boldsymbol{x}_j\in H(\boldsymbol{x}_i)}\underline{\boldsymbol{T}}[\boldsymbol{x}_i,t]\langle\boldsymbol{x}_j-\boldsymbol{x}_i\rangle\cdot\Delta V_{\boldsymbol{x}_i}\cdot\Delta V_{\boldsymbol{x}_j} - \sum_{\boldsymbol{x}_i\in\mathfrak{B}}\sum_{\boldsymbol{x}_k\in H'(\boldsymbol{x}_i)}\underline{\boldsymbol{T}}[\boldsymbol{x}_k,t]\langle\boldsymbol{x}_i-\boldsymbol{x}_k\rangle\cdot\Delta V_{\boldsymbol{x}_k}\cdot\Delta V_{\boldsymbol{x}_i}=\boldsymbol{0} \tag{54}$$

But given Eq. (47) it is concluded that Eq. (54) is already satisfied, therefore the linear momentum balance is valid in dual horizon peridynamics. An intuitive way to notice the conservation of linear momentum is to realize that for every direct force, there is a unique reactionary force. This principle is not violated when the dual horizon set is introduced, therefore linear momentum is conserved.

2.4.4. Balance of angular momentum in dual horizon peridynamics

The angular momentum is conserved if the net internal torque equals the rate of angular momentum of the body $\mathfrak{B}$. As shown in Eq. (55). In the case of a body under no external force, the sum of the internal torque must equal zero.

$$\sum_{\boldsymbol{x}_i\in\mathfrak{B}}\sum_{\boldsymbol{x}_j\in H(\boldsymbol{x}_i)}\boldsymbol{y_i}\times\underline{\boldsymbol{T}}[\boldsymbol{x}_i,t]\langle\boldsymbol{x}_j-\boldsymbol{x}_i\rangle\cdot\Delta V_{\boldsymbol{x}_i}\cdot\Delta V_{\boldsymbol{x}_j} - \sum_{\boldsymbol{x}_i\in\mathfrak{B}}\sum_{\boldsymbol{x}_k\in H'(\boldsymbol{x}_i)}\boldsymbol{y_i}\times\underline{\boldsymbol{T}}[\boldsymbol{x}_k,t]\langle\boldsymbol{x}_i-\boldsymbol{x}_k\rangle\cdot\Delta V_{\boldsymbol{x}_k}\cdot\Delta V_{\boldsymbol{x}_i}=\boldsymbol{0} \tag{55}$$

With $\boldsymbol{y}_i = \boldsymbol{x}_i + \boldsymbol{u}_i$. Expanding Eq. (55) and using Eq. (47) one can get Eq. (56)

$$
\begin{aligned}
&\sum_{x_i\in\mathfrak{B}}\sum_{x_j\in H(x_i)} \boldsymbol{y_i}\times\underline{\boldsymbol{T}}[\boldsymbol{x}_i,t]\langle\boldsymbol{x}_j-\boldsymbol{x}_i\rangle\cdot\Delta V_{x_i}\cdot\Delta V_{x_j}\\
&\quad-\sum_{x_i\in\mathfrak{B}}\sum_{x_k\in H'(x_i)} \boldsymbol{y_i}\times\underline{\boldsymbol{T}}[\boldsymbol{x}_k,t]\langle\boldsymbol{x}_i-\boldsymbol{x}_k\rangle\cdot\Delta V_{x_k}\cdot\Delta V_{x_i}\\
&\quad=\sum_{x_i\in\mathfrak{B}}\sum_{x_j\in H(x_i)} (\boldsymbol{x_i}+\boldsymbol{u_i})\times\underline{\boldsymbol{T}}[\boldsymbol{x}_i,t]\langle\boldsymbol{x}_j-\boldsymbol{x}_i\rangle\cdot\Delta V_{x_i}\cdot\Delta V_{x_j}\\
&\quad-\sum_{x_i\in\mathfrak{B}}\sum_{x_k\in H'(x_i)} (\boldsymbol{x_i}+\boldsymbol{u_i})\times\underline{\boldsymbol{T}}[\boldsymbol{x}_k,t]\langle\boldsymbol{x}_i-\boldsymbol{x}_k\rangle\cdot\Delta V_{x_k}\cdot\Delta V_{x_i}\\
&\quad=\sum_{x_i\in\mathfrak{B}}\sum_{x_j\in H(x_i)} (\boldsymbol{x_i}+\boldsymbol{u_i})\times\underline{\boldsymbol{T}}[\boldsymbol{x}_i,t]\langle\boldsymbol{x}_j-\boldsymbol{x}_i\rangle\cdot\Delta V_{x_i}\cdot\Delta V_{x_j}\\
&\quad-\sum_{x_i\in\mathfrak{B}}\sum_{x_j\in H(x_i)} \big(\boldsymbol{x_j}+\boldsymbol{u_j}\big)\times\underline{\boldsymbol{T}}[\boldsymbol{x}_i,t]\langle\boldsymbol{x}_j-\boldsymbol{x}_i\rangle\cdot\Delta V_{x_j}\cdot\Delta V_{x_i}\\
&\quad=\sum_{x_i\in\mathfrak{B}}\sum_{x_j\in H(x_i)} \big(\boldsymbol{x_i}+\boldsymbol{u_i}-\boldsymbol{x_j}-\boldsymbol{u_j}\big)\times\underline{\boldsymbol{T}}[\boldsymbol{x}_i,t]\langle\boldsymbol{x}_j-\boldsymbol{x}_i\rangle\cdot\Delta V_{x_i}\\
&\quad\cdot\Delta V_{x_j}=-\sum_{x_i\in\mathfrak{B}}\sum_{x_j\in H(x_i)} \underline{\boldsymbol{Y}}\langle\boldsymbol{x}_j-\boldsymbol{x}_i\rangle\times\underline{\boldsymbol{T}}[\boldsymbol{x}_i,t]\langle\boldsymbol{x}_j-\boldsymbol{x}_i\rangle\Delta V_{x_j}\,\Delta V_{x_i}\\
&\quad=\boldsymbol{0}
\end{aligned}
\tag{56}
$$

2.5. Stress calculation in peridynamics

The stress calculation in peridynamics requires establishing a relationship between the force density and stress components given the non-locality of the model. Lehoucq and Silling [105] showed in a bond-based peridynamic model, the stress tensor $\boldsymbol{V}$ at point $\boldsymbol{x}$ is defined as in Eq. (57)..

$$
\boldsymbol{V}(\boldsymbol{x})=\frac{1}{2}\int_{\Theta}\int_{0}^{\infty}\int_{0}^{\infty}(y+z)^2\hat{\boldsymbol{f}}(\boldsymbol{x}+y\boldsymbol{m},\boldsymbol{x}-z\boldsymbol{m})\otimes\boldsymbol{m}dydzd\Omega_{\boldsymbol{m}} \tag{57}
$$

In Eq. (57), $\hat{\boldsymbol{f}}$ is an alternate representation of the pairwise force density $\boldsymbol{f}$. Their relationship is defined in Eq. (58).

$$
\hat{\boldsymbol{f}}\big(\boldsymbol{x}_j,\boldsymbol{x}_i\big)=\begin{cases}\boldsymbol{f}\big(\boldsymbol{\xi}_{ij},\boldsymbol{\eta}_{ij}\big), & if\ \boldsymbol{x}_j\in H(\boldsymbol{x}_i)\\ \boldsymbol{0}, & otherwise\end{cases} \tag{58}
$$

This alternate representation is only used to simplify the equation. In other words, $\hat{\boldsymbol{f}}(\boldsymbol{x}_j, \boldsymbol{x}_i)$ equals the pairwise force density $\boldsymbol{x}_j$ applied onto $\boldsymbol{x}_i$. In Eq. (57), $\boldsymbol{m}$ is a unit vector, and $d\Omega_m$ denotes a differential solid angle in the direction of $\boldsymbol{m}$. Equation (57) is thus interpreted as the outer product of $\boldsymbol{m}$ and all the pairwise force densities parallel to $\boldsymbol{m}$ that pass through point $\boldsymbol{x}$. Similarly, in SB-PD, the stress tensor $\boldsymbol{V}$ at point $\boldsymbol{x}$ can be defined as in Eq. (59).

$$\boldsymbol{V}(\boldsymbol{x}) = \frac{1}{2}\int_{\Theta}\int_{0}^{\infty}\int_{0}^{\infty}(y+z)^2(\underline{\hat{\boldsymbol{T}}}[\boldsymbol{x}-z\boldsymbol{m},t]\langle(y-z)\boldsymbol{m}\rangle - \underline{\hat{\boldsymbol{T}}}[\boldsymbol{x}+y\boldsymbol{m},t]\langle(z-y)\boldsymbol{m}\rangle)\otimes\boldsymbol{m}\,dy\,dz\,d\Omega_{\boldsymbol{m}} \tag{59}$$

With the condition that the force vector-state follows the conditions of Eq. (60).

$$\underline{\hat{\boldsymbol{T}}}[\boldsymbol{x}-z\boldsymbol{m},t]\langle(y-z)\boldsymbol{m}\rangle = \begin{cases}\underline{\boldsymbol{T}}[\boldsymbol{x}-z\boldsymbol{m},t]\langle(y-z)\boldsymbol{m}\rangle, & if\ \boldsymbol{x}+y\boldsymbol{m}\in H(\boldsymbol{x}-z\boldsymbol{m})\\ \boldsymbol{0}, & otherwise\end{cases} \tag{60}$$

In both equations (58) and (59) the coefficient $\frac{1}{2}$ exists to prevent the summation of both direct and reactionary force densities since the integration iterates through every unit vector $\boldsymbol{m}$. Note that Eq. (59) combined with Eq. (60) is also valid for a DH-PD model as the integration iterates through all the material points that may exert a force density passing through point $\boldsymbol{x}$, regardless of whether the said material point is in the horizon or dual horizon set of point $\boldsymbol{x}$.

2.5.1. Physical and classical interpretations of peridynamic stress tensor

Lehoucq and Silling [105] also proved that Eq. (61) holds true if $\boldsymbol{f}$ is continuously differentiable.

$$\nabla.\boldsymbol{V}(\boldsymbol{x}) = \int_{\boldsymbol{x}'\in H(\boldsymbol{x})}\boldsymbol{f}(\boldsymbol{\xi},\boldsymbol{\eta})\,dV_{\boldsymbol{x}'} \tag{61}$$

Equations (62) and (63) are the equivalents of Eq. (61) in SB-PD and DH-PD.

$$\nabla.\boldsymbol{V}(\boldsymbol{x}_i) = \int_{\boldsymbol{x}_j\in H(\boldsymbol{x}_i)}(\underline{\boldsymbol{T}}[\boldsymbol{x}_i,t]\langle\boldsymbol{x}_j-\boldsymbol{x}_i\rangle - \underline{\boldsymbol{T}}[\boldsymbol{x}_j,t]\langle\boldsymbol{x}_i-\boldsymbol{x}_j\rangle)\,dV_{\boldsymbol{x}_j} \tag{62}$$

In DH-PD, an extra integration is required for all the dual horizon bonds.

$$\nabla.\boldsymbol{V}(\boldsymbol{x}_i) = \int_{\boldsymbol{x}_j \in H(\boldsymbol{x}_i)} \underline{\boldsymbol{T}}[\boldsymbol{x}_i, t]\langle \boldsymbol{x}_j - \boldsymbol{x}_i \rangle dV_{\boldsymbol{x}_j} - \int_{\boldsymbol{x}_k \in H'(\boldsymbol{x}_i)} \underline{\boldsymbol{T}}[\boldsymbol{x}_k, t]\langle \boldsymbol{x}_i - \boldsymbol{x}_k \rangle \, dV_{\boldsymbol{x}_k} \tag{63}$$

The equations above allow for a rewriting of the equation of motion similar to that of the classical theory of mechanics such as in Eq. (64).

$$\rho(\boldsymbol{x})\ddot{\boldsymbol{u}}(\boldsymbol{x}, t) = \nabla.\boldsymbol{V}(\boldsymbol{x}) + \boldsymbol{b}(\boldsymbol{x}, t) \tag{64}$$

It is clear from Eq. (64) that $\boldsymbol{V}$ is the equivalent of the first Piola stress tensor in classical continuum mechanics [105]. The symmetry of $\boldsymbol{V}$ is guaranteed if and only if balances of linear and angular momentum are conserved.

Equation (65) is another necessary definition, called the peridynamic force flux, and is defined for any unit vector $\boldsymbol{n}$.

$$\boldsymbol{\tau}(\boldsymbol{x}, \boldsymbol{n}) = \boldsymbol{V}(\boldsymbol{x})\boldsymbol{n} \tag{65}$$

Substituting Eq. (59) into Eq. (65) one can have the form of Eq. (66).

$$\begin{aligned} \boldsymbol{\tau}(\boldsymbol{x}, \boldsymbol{n}) = \frac{1}{2} \int_{\Theta}^{\square} \int_{0}^{\infty} \int_{0}^{\infty} (y+z)^2 \big(\underline{\widehat{\boldsymbol{T}}}[\boldsymbol{x} - z\boldsymbol{m}, t]\langle (y-z)\boldsymbol{m} \rangle \\ - \underline{\widehat{\boldsymbol{T}}}[\boldsymbol{x} + y\boldsymbol{m}, t]\langle (z-y)\boldsymbol{m} \rangle \big) \boldsymbol{m}.\boldsymbol{n} \, dydzd\Omega_{\boldsymbol{m}} \end{aligned} \tag{66}$$

Chapter 3:

Methodology

3.1. Discretization of equation of motion

In peridynamics the body $\mathfrak{B}$ is discretized into a uniform grid of material points at equal distances of Δx from one another. The equation of motion is thus approximated as Eq. (67).

$$\rho\ddot{\boldsymbol{u}}(\boldsymbol{x}_i,t)=\sum_{\boldsymbol{x}_j\in H(\boldsymbol{x}_i)}\underline{\boldsymbol{T}}[\boldsymbol{x}_i,t]\langle\boldsymbol{x}_j-\boldsymbol{x}_i\rangle\,\Delta V_{\boldsymbol{x}_j}-\sum_{\boldsymbol{x}_k\in H\prime(\boldsymbol{x}_i)}\underline{\boldsymbol{T}}[\boldsymbol{x}_k,t]\langle\boldsymbol{x}_i-\boldsymbol{x}_k\rangle\Delta V_{\boldsymbol{x}_k}+\boldsymbol{b}(\boldsymbol{x}_i,t) \tag{67}$$

Similarly, three-dimensional problems are discretized in three cardinal directions by a uniform grid of material points. A time integration scheme is required to solve Eq. (67). An explicit forward and backward difference technique is applied to solve for $\boldsymbol{u}^n$ at the n$^{\text{th}}$ time step or $t=n\Delta t$. Substituting $t=n\Delta t$ in Eq. (67), the numerical equation of motion becomes Eq. (68)

$$\begin{aligned}\rho\ddot{\boldsymbol{u}}(\boldsymbol{x}_i,n\Delta t)=&\sum_{\boldsymbol{x}_j\in H(\boldsymbol{x}_i)}\underline{\boldsymbol{T}}[\boldsymbol{x}_i,n\Delta t]\langle\boldsymbol{x}_j-\boldsymbol{x}_i\rangle\;\Delta V_{\boldsymbol{x}_j}\\&-\sum_{\boldsymbol{x}_k\in H\prime(\boldsymbol{x}_i)}\underline{\boldsymbol{T}}[\boldsymbol{x}_k,n\Delta t]\langle\boldsymbol{x}_i-\boldsymbol{x}_k\rangle\Delta V_{\boldsymbol{x}_k}+\boldsymbol{b}(\boldsymbol{x}_i,n\Delta t)\end{aligned} \tag{68}$$

It is worth noting that according to Eq. (8), force densities are dependent on the deformed relative position vectors. Thus, per time step, the force densities must be recalculated as in Eq. (69).

$$\underline{\boldsymbol{T}}[n\Delta t]=\overline{\underline{\boldsymbol{T}}}(\underline{\boldsymbol{Y}}[n\Delta t],\underline{\dot{\boldsymbol{Y}}}[n\Delta t],\underline{\boldsymbol{q}}[n\Delta t],\boldsymbol{q}^{(n)}) \tag{69}$$

With superscript n depicting the value of the variable in time step $t=n\Delta t$. Utilizing Eq. (32) to find the force density in a time integration scheme one derives Eq. (70) .

$$\underline{\boldsymbol{T}}[\boldsymbol{x}_i,n\Delta t]\langle\boldsymbol{\xi}_{ij}\rangle=\frac{2\delta}{|\boldsymbol{\xi}_{ij}|}\left(d\alpha\;\theta_i^{(n)}+\beta s_{ij}^{(n)}\right)\frac{\boldsymbol{\xi}_{ij}+\boldsymbol{\eta}_{ij}^{(n)}}{\left|\boldsymbol{\xi}_{ij}+\boldsymbol{\eta}_{ij}^{(n)}\right|} \tag{70}$$

At time step $t=n\Delta t$, the dilatation term becomes Eq. (71).

$$\theta_i^{(n)}=\sum_{\boldsymbol{x}_j\in H(\boldsymbol{x}_i)}^{\square}d\delta s_{ij}^{(n)}\Lambda_{ij}^{(n)}V_{\boldsymbol{x}_j} \tag{71}$$

And the stretch becomes Eq. (72).

$$s_{ij}^{(n)} = \frac{\left|\boldsymbol{\xi}_{ij} + \boldsymbol{\eta}_{ij}^{(n)}\right| - \left|\boldsymbol{\xi}_{ij}\right|}{\left|\boldsymbol{\xi}_{ij}\right|} \tag{72}$$

3.2. Adaptive dynamic relaxation

The dynamic relaxation technique converts a static or a quasi-static problem into a dynamic one to solve it. Since peridynamic equation of motion is dynamic, a dynamic relaxation correction will convert the benchmark problems in this study into dynamic equations. The steady-state solution of the dynamically relaxed equation corresponds to the static solution of the original equation [127]. To achieve this, the dynamic relaxation technique solves peridynamic equations with the addition of a damping coefficient that is artificially introduced into the equation. If the damping coefficient is updated iteratively, the method is called Adaptive Dynamic Relaxation (ADR) [118], which will be used in this research.

In accordance with the dynamic relaxation approach, the equation of motion is reformulated with the addition of the time derivative of displacement multiplied by the fictitious inertia and damping terms as in Eq. (73).

$$\boldsymbol{D}\ddot{\boldsymbol{u}}(\boldsymbol{x},t) + c\boldsymbol{D}\dot{\boldsymbol{u}}(\boldsymbol{x},t) = \boldsymbol{F}(\boldsymbol{\xi},\boldsymbol{\eta},\dot{\boldsymbol{\eta}},t) \tag{73}$$

The diagonal matrix $\boldsymbol{D}$ is called the fictitious density matrix and c is the damping coefficient. The addition of c allows a fictitious dampening effect which can drastically reduce the number of iterations to solve the equation.

Using a central-difference explicit time integration scheme, the displacements and velocities of each iteration can be defined as in Eq. (74).

$$\dot{\boldsymbol{u}}^{(n+\frac{1}{2})} = \frac{\left(2 - c^{(n)}\Delta t\right)\dot{\boldsymbol{u}}^{\left(n-\frac{1}{2}\right)} + 2\Delta t\boldsymbol{D}^{-1}\boldsymbol{F}^{(n)}}{2 + c^{(n)}\Delta t} \tag{74}$$

Equation (74) is required to calculate $\boldsymbol{u}$ at time step $t = n + 1$, shown in Eq. (75).

$$\boldsymbol{u}^{(n+1)} = \boldsymbol{u}^{(n)} + \Delta t\dot{\boldsymbol{u}}^{\left(n+\frac{1}{2}\right)} \tag{75}$$

The dynamic relaxation approach involves initiating c and $\boldsymbol{D}$ and then iteratively solving equations (70) to (75). For convenience, Δt can be assumed to be equal to 1, as the magnitude of

time step can be arbitrary in explicit time schemes. To ensure the stability and convergence of the solution, diagonal density matrix $\boldsymbol{D}$ must follow the inequality of Eq. (76).

$$a_{ii} < \frac{1}{4}\Delta t^2 \sum_j |\boldsymbol{K}_{ij}| \tag{76}$$

With a_{ii} as the diagonal elements of $\boldsymbol{D}$ and $\boldsymbol{K}_{ij}$ as the stiffness matrix of the bond between material points $\boldsymbol{x}_i$ and $\boldsymbol{x}_j$ in the global coordinate system. The calculation of the bond stiffness matrix requires the differentiation of the force density with respect to the relative displacement vector $\boldsymbol{\eta}$, which can prove tedious given the nonlinearity of interactions between the two. Assuming small displacements, the stiffness matrix can be approximated as Eq. (77).

$$\left|\boldsymbol{K}_{ij}\right| = \frac{\partial\left(\boldsymbol{t}_{ij} - \boldsymbol{t}_{ji}\right)}{\partial\left(\left|\boldsymbol{\eta}_{ij}\right|\right)} . \boldsymbol{e} = \left|\boldsymbol{\xi}_{ij} . \boldsymbol{e}\right| \frac{2\delta}{\left|\boldsymbol{\xi}_{ij}\right|^2} \left(\frac{ad^2\delta}{\left|\boldsymbol{\xi}_{ij}\right|}\left(V_i + V_j\right) + \beta\right) \tag{77}$$

With $\boldsymbol{e}$ as the unit vector along the global cartesian coordinate directions [128].

To find the value of c, one can use the lowest frequency of the system. Equation (78) shows the approximation of the system frequency using Rayleigh's quotient [128].

$$\omega = \sqrt{\frac{\boldsymbol{u}^* \boldsymbol{K} \boldsymbol{u}}{\boldsymbol{u}^* \boldsymbol{D} \boldsymbol{u}}} \tag{78}$$

The condition of using Rayleigh's quotient is for $\boldsymbol{K}$ and $\boldsymbol{D}$ to be of Hermitian matrix and for vector $\boldsymbol{u}$ to be nonzero. For real vectors and matrices, the conjugate transpose $\boldsymbol{u}^*$ is reduced to the common transpose $\boldsymbol{u}^T$ and the Hermitian condition is reduced to the matrix being symmetric [128]. The calculation of the denominator of Eq. (78) can be simplified by only measuring the damping coefficient at the nth iteration, expressed in Eq. (79).

$$c^{(n)} = 2\sqrt{\frac{\boldsymbol{u}^{(n)^T} \boldsymbol{k}^{(n)} \boldsymbol{u}^{(n)}}{\boldsymbol{u}^{(n)^T} \boldsymbol{u}^{(n)}}} \tag{79}$$

With $\boldsymbol{k}^{(n)}$ as the diagonal stiffness matrix in the local coordinate system at the nth iteration, given as Eq. (80).

$$\boldsymbol{k}_{ii}^{(n)} = -\frac{\boldsymbol{F}_i^{(n)} - \boldsymbol{F}_i^{(n-1)}}{\mathbf{D}_{\mathrm{ii}} \Delta t \dot{\boldsymbol{u}}_i^{\left(n-\frac{1}{2}\right)}} \tag{80}$$

Rayleigh's quotient is only an approximation of the lowest system frequency as the lowest frequency of the system at equilibrium is not known. This will lead the overdamping or underdamping depending on the overestimation or underestimation of the damping coefficient. In other words, Eq. (79) gives the critical damping coefficient of the nth iteration. The cyclic update of the coefficient ensures that the damping coefficient reaches its optimum value, and therefore ensuring that the equation converges faster to its equilibrium state [129].

3.3. Volume correction factor

A volume correction factor is introduced into the peridynamic equations by Silling [130] which corrects the volume of neighboring materials depending on their distance and the grid used to discretize the body. In a uniform grid, with a constant space of Δx between each material point and horizon size of $\delta = 3\Delta x$, the volume of certain neighbors will only be partially inside the horizon (See Figure 3.1). The distance of neighbors is given by $\boldsymbol{\xi_{ij}}$. For any neighbor that falls in the range of $|\boldsymbol{\xi}_{ij}| < \delta - r$, with $r = 2\Delta x$, the entire volume lies inside the horizon δ and therefore the volume correction factor $\upsilon_j = 1$. For neighbors with their distance between $\delta - r < |\boldsymbol{\xi}_{ij}| < \delta$, υ_j is defined in Eq. (81).

$$\upsilon_j = \frac{\delta + r - |\boldsymbol{\xi}_{ij}|}{2r} \tag{81}$$

The volume correction factor thus linearly varies between 1 and ½ depending on $|\boldsymbol{\xi}_{ij}|$. The equation of motion is thus updated into Eq. (82).

$$\rho\ddot{\boldsymbol{u}}(\boldsymbol{x}_i, t) = \sum_{\boldsymbol{x}_j \in H(\boldsymbol{x}_i)} \underline{\boldsymbol{T}}[\boldsymbol{x}_i, t]\langle \boldsymbol{x}_j - \boldsymbol{x}_i \rangle \upsilon_j \Delta V_{\boldsymbol{x}_j} - \sum_{\boldsymbol{x}_k \in H\prime(\boldsymbol{x}_i)} \underline{\boldsymbol{T}}[\boldsymbol{x}_k, t]\langle \boldsymbol{x}_i - \boldsymbol{x}_k \rangle \upsilon_k \Delta V_{\boldsymbol{x}_k} + \boldsymbol{b}(\boldsymbol{x}_i, t) \tag{82}$$

3.4. Surface effects

The implicit assumption in calculating peridynamic parameters such as force density and dilatation term is that the material point horizon does not extend the boundaries of the domain. A correction is thus needed for the material points that are near or at free surfaces.

This correction is heavily dependent on the shape of the free surface and therefore it is not possible to analytically find a correction factor for all the arbitrary surfaces. Madenci [40] used the terms

dilatation correction factor and distortion correction factors as surface correction factors. He approximated the dilatation correction factor as the dilatation term ratio between peridynamics and continuum mechanics and the distortion correction factor as the strain energy ratio between peridynamic and continuum mechanics. The surface correction factors are thus dependent on the problem parameters and loading conditions and must be recalculated given a different problem.

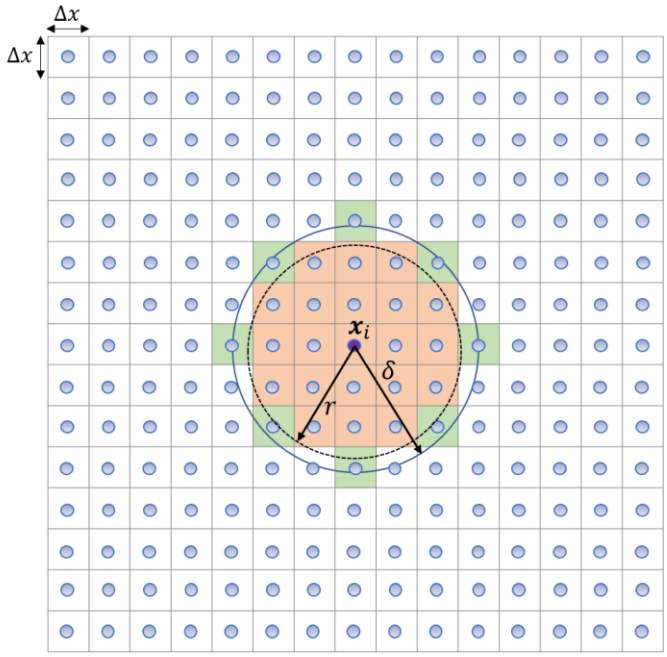

Figure 3.1. Volume correction factor is required for all the neighbors outside the circle with radius r but inside the horizon of $\boldsymbol{x}_i$ (i.e. the green cells).

A simple uniaxial stretch along one of the coordinate axes could be used to derive the peridynamic dilatation term θ_{PD}. In the case of a homogenous uniform body, the loading condition can be expressed as in Eq. (83).

$$\boldsymbol{u}_1^T(\boldsymbol{x}) = \{\frac{\partial u_1}{\partial x_1} x_1,\ \ 0\} \tag{83}$$

The dilatation term θ_{PD} is calculated using Eq. (71). In continuum mechanics, the corresponding dilatation term is uniform throughout the body and is given by Eq. (84).

$$\theta_{CM,i} = \varepsilon = \frac{\partial u_1}{\partial x_1} \tag{84}$$

Choosing a constant $\frac{\partial u_1}{\partial x_1} = \zeta$, the dilatation correction factor for material point $\boldsymbol{x}_i$ is calculated by Eq. (85).

$$G_{d,i} = \frac{\theta_{CM}}{\theta_{PD}} = \frac{\zeta}{d\delta \sum_{\boldsymbol{x}_j \in H(\boldsymbol{x}_i)} s_{ij}^{(n)} \Lambda_{ij}^{(n)} V_j} \tag{85}$$

The same argument is made for strain energy density W. In continuum mechanics, the strain energy density at point $\boldsymbol{x}_i$ is defined by Eq. (86).

$$W_{CM,i} = \left(\frac{E}{2(1-\nu^2)} - \alpha\right)\zeta^2 \tag{86}$$

In peridynamics, the strain energy density for material point $\boldsymbol{x}_i$ is given by Eq. (87)

$$W_{PD,i} = \alpha\theta_i^2 + \beta\delta \sum_{\boldsymbol{x}_j \in H(\boldsymbol{x}_i)} |\boldsymbol{\xi}_{ij}| s_{ij}^2 V_j \tag{87}$$

With α and β defined in Eq. (33). The distortion correction factor G_b is thus defined by Eq. (88)

$$G_{b,i} = \frac{W_{CM,i}}{W_{PD,i}} = \frac{\left(\frac{E}{2(1-\nu^2)} - \alpha\right)\zeta^2}{\alpha\theta_i^2 + \beta\delta \sum_{\boldsymbol{x}_j \in H(\boldsymbol{x}_i)} |\boldsymbol{\xi}_{ij}| s_{ij}^2 V_j} \tag{88}$$

In most cases, the W and θ of two neighbors are not equal. Therefore, unequal correction factors are derived for a pair of neighbors. To utilize the correction factor when discussing the interaction of two material points $\boldsymbol{x}_i$ and $\boldsymbol{x}_j$, the mean value can be used as defined in Eq. (89)

$$\bar{G}_{d,i,j} = \frac{G_{d,i} + G_{d,j}}{2}, \quad \bar{G}_{b,i,j} = \frac{G_{b,i} + G_{b,j}}{2} \tag{89}$$

After considering the surface effect for correction, the W and θ are redefined into Eq. (90) and Eq. (91), respectively.

$$\theta_i = d\delta \sum_{\boldsymbol{x}_j \in H(\boldsymbol{x}_i)} \bar{G}_{d,i,j} s_{ij} \Lambda_{ij} V_j \tag{90}$$

$$W_{PD,i} = \alpha\theta_i^2 + \beta\delta \sum_{\boldsymbol{x}_j \in H(\boldsymbol{x}_i)} \bar{G}_{b,i,j} |\boldsymbol{\xi}_{ij}| s_{ij}^2 V_j \tag{91}$$

3.5. Selecting horizon size

In single-horizon peridynamics, given a uniform grid, the horizon size can be assumed to be $\delta = 3\Delta x$, with Δx as the spacing between each material point. This horizon size value was first suggested by Silling and Askari [123] in bond-based peridynamics. Given a uniform grid and no damage in the peridynamical body, Wang and Oterkus [131] showed that a minimum of $\delta = 3\Delta x$ leads to accurate results compared to conventional FEM results. Any increase in the value of horizon size will lead to more accuracy but at the same time to more computation time. It is also shown that in a DH-PD, the minimum of $\delta = 3\Delta x$ is necessary for acceptable accuracy for both subdomains of different horizon sizes [131].

3.6. Neighbor searching algorithms

An algorithm needs to be implemented to find the neighbors of each material point. An exhaustive algorithm can be used in which the distance of each material point pair is measured and compared to the horizon size δ.

Algorithm 1 Exhaustive neighbor search

```
for i in range 1: N do
    for j in range 1: N and j ≠ i do
        calculate |ξ_ij|
        if |ξ_ij| ≤ δ(x_i) do
            add x_j to H(x_i)
        end if
    end for
end for
```

With N as the number of material points used in for discretization. With the time complexity of $O(N^2)$, the exhaustive neighbor search algorithm is not efficient. This time complexity order

means that as the number of N increases, the time required to find neighbors grows quadratically. If one has a large number of material points, this algorithm becomes computationally expensive.

The search for neighbors can be optimized by limiting the search only to an area in the vicinity of the material point under investigation. This method, called "Regional Neighbor Search", is the neighbor search algorithm that is implemented and utilized in this research instead of the exhaustive method. In this method, the body is separated into blocks of material points. The search for potential neighbors is limited to the block containing the material point, called the 'home

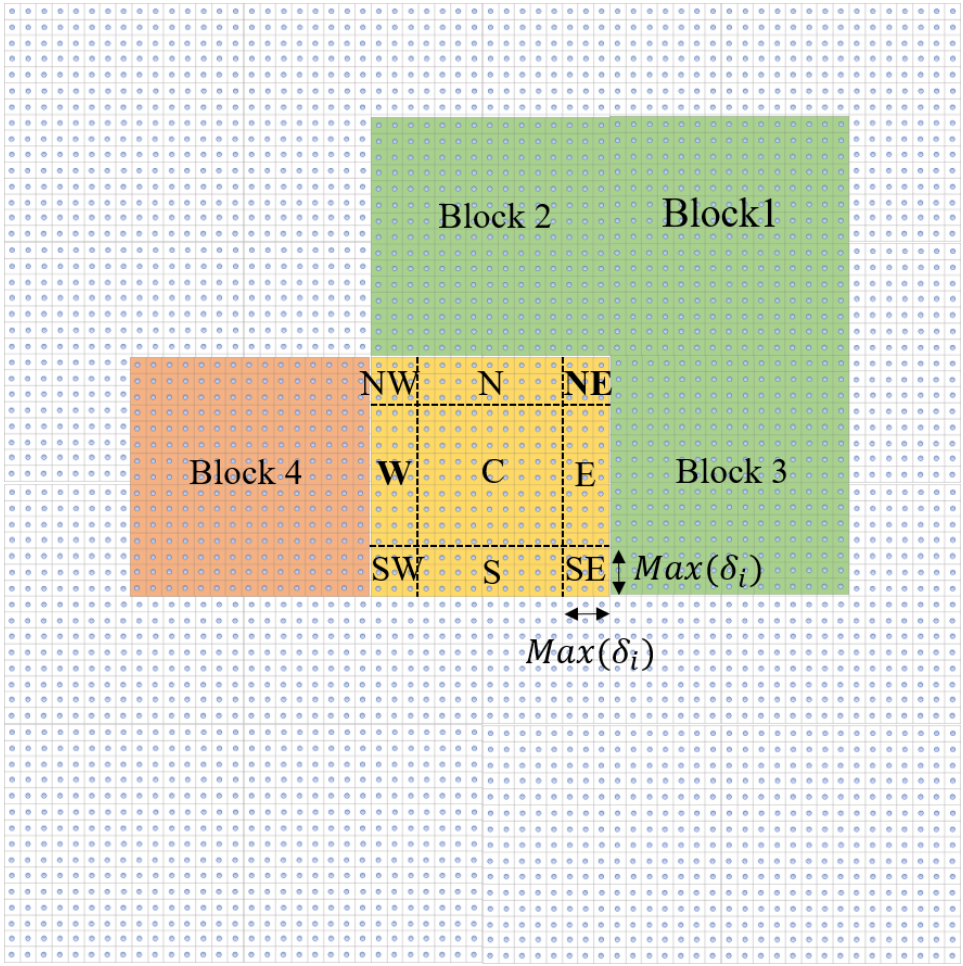

Figure 3.2. Schematics of regional neighbor search algorithm

block', and the adjacent blocks, depending on the coordinates of the material point. Each block is further divided into regions called 'E', 'NE', 'N', 'NW', 'W', 'SW', 'S', and 'C', which are demonstrated in Figure 3.2. Depending on which region the material point falls into, closest adjacent blocks will be included in the search for neighbors. The regions 'W', 'E', 'N', and 'S' each have a width of $\delta(\boldsymbol{x}_i)$, meaning that any material point that falls into the center of the block

'C' cannot have any neighbors outside of its home block. If the material point falls into the side regions, two blocks will be searched, the home block and the adjacent block which shares the corresponding edge. If the material point belongs to the corner regions ('NE', 'NW', 'SE', 'SW'), four blocks are searched: the home block and the other three blocks which share the corresponding corner. In the example of Figure 3.2, if a material point falls into region 'NE' of its home block (the yellow block), the search for its neighbors is focused on Blocks 1, 2, 3, and the home block (i.e. the green blocks plus the yellow block). If on the other hand, the material point falls into region 'W' of its home block, the search for neighbors is focused on the adjacent block to the left (Block 4) and the home block. Finally, the search for neighbors for any material point that falls into region 'C' is limited only to the home block itself. The blocks are square in shape as they best fit the geometry of the problem, but the shape can be arbitrary. A pseudo-code for Regional Neighbor Search algorithm can be seen in Algorithm 2 table.

Algorithm 2 Regional Neighbor Search

Separate the body into blocks based on block width and block length specified
for *i in range* 1: N **do**
$homeBlock \leftarrow$ *block containing* $\boldsymbol{x}_i$ *based on* $\boldsymbol{x}_i$ *coordinates*
Find the distance between $\boldsymbol{x}_i$ *and center of homeBlock*
Find the region for $\boldsymbol{x}_i$ *based on distance in step* 4
$adjacentBlocks \leftarrow$ *adjacent blocks based on* $\boldsymbol{x}_i$ *region and homeBlock*
for $\boldsymbol{x}_j$ *in enumerate*$\{homeBlock, adjacentBlocks\}$ **and** $j \neq i$ **do**
calculate $|\xi_{ij}|$
if $|\xi_{ij}| \leq \delta(\boldsymbol{x}_i)$ **do**
add $\boldsymbol{x}_j$ *to neighbors*$(\boldsymbol{x}_i)$ *array*
end if
end for
end for

3.7. Initial and boundary conditions

The peridynamic equation of motion is a complex partial differential equation with time and space derivatives. Notably, it doesn't rely on simplifications involving kinematic linearity, making it

well-suited for analyzing geometrically nonlinear scenarios. This equation encompasses both time derivatives and spatial integration but does not involve spatial derivatives related to displacements. Consequently, it remains applicable universally, irrespective of the presence or absence of displacement discontinuities within the material. Given that peridynamics equations are expressed as integro-differential equations, the approach for implementing boundary conditions in the peridynamics framework differs from that in the classical continuum mechanics. In peridynamics, boundary conditions are imposed by defining regions in space, and these regions are occasionally constructed as artificial or imaginary areas extending beyond the actual solution domain. These regions are called fictitious regions, $\mathcal{R}_f$, and are outside the main solution body $\mathfrak{B}$ shown in Figure 3.3. The effectiveness of this technique was shown by Macek and Silling [93] who suggested a fictitious boundary layer with an outward dimension of at least the size of the horizon δ. The

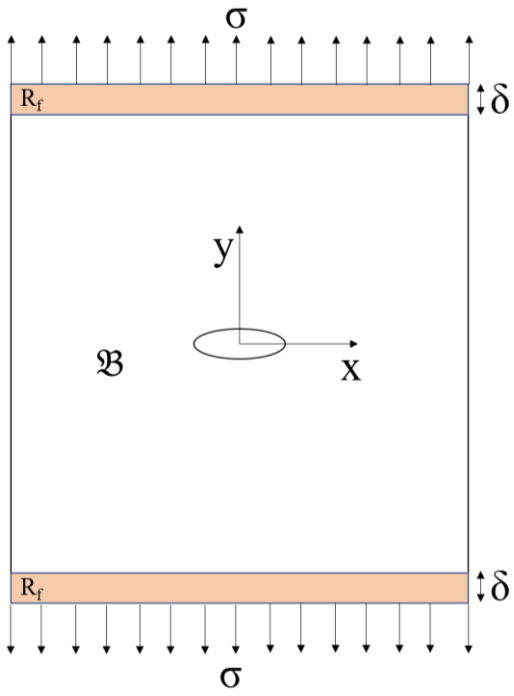

Figure 3.3. Constraints and external loads are required to be applied to boundary regions, R_f, with the outward dimension size of δ.

minimum size of δ is required so that the boundary conditions are successfully implemented upon the solution body.

3.7.1. Displacement and velocity constraints

Given a prescribed displacement vector $\boldsymbol{U}_0$, displacement constraints can be defined by Eq. (92).

$$\boldsymbol{u}(\boldsymbol{x},t) = \boldsymbol{U}_0, for\ \boldsymbol{x} \in\ \mathcal{R}_\mathrm{f} \tag{92}$$

A smoother transitory constraint can be enforced in the form of Eq. (93).

$$\boldsymbol{u}(\boldsymbol{x},t) = \begin{cases} \dfrac{\boldsymbol{U}_0 t}{t_0}, & for\ 0 \le t \le t_0 \\ \boldsymbol{U}_0, & for\ t_0 \le t \end{cases} \tag{93}$$

A velocity constraint can instead be prescribed given an initial velocity vector $\boldsymbol{V}(t)$ by Eq. (94).

$$\dot{\boldsymbol{u}}(\boldsymbol{x},t) = \boldsymbol{V}(t), for\ \boldsymbol{x} \in\ \mathcal{R}_\mathrm{f} \tag{94}$$

The same step function as in Eq. (93) could be used to avoid an abrupt velocity introduction as in Eq. (95).

$$\dot{\boldsymbol{u}}(\boldsymbol{x},t) = \begin{cases} \dfrac{\boldsymbol{V}(t) t}{t_0}, for\ 0 \le t \le t_0 \\ \boldsymbol{V}(t), \quad for\ t_0 \le t \end{cases} \tag{95}$$

3.7.2. External loads

The external forces can be introduced in a peridynamical model by applying an appropriate body force to the material points at the desired boundaries. In the case of a distributed pressure, $\boldsymbol{p}(\boldsymbol{x},t)$, the body force density vector is expressed by Eq. (96).

$$\boldsymbol{b}(\boldsymbol{x},t) = -\frac{1}{\Delta} p(\boldsymbol{x},t)\boldsymbol{n} \tag{96}$$

With Δ as a boundary dimension size which is usually set to be the horizon size δ.

Figure 3.4 shows the flowchart which summarizes the entire process of numerically solving a DH-PD model developed to solve for displacement and stress components. Initial geometrical and peridynamic parameters are inputs of the algorithm. These include desired peridynamic horizon size, selection of areas of interest, dimension of the body $\mathfrak{B}$, etc. The discretization is then commenced coordinates are assigned to each material point. Next, Regional Neighbor Search algorithm finds and assigns neighbors of each material point before the algorithm enters the iterative process of solving the peridynamic equation of motion. Note that certain parameters such as surface correction factor and dilatation term will have to be recalculated as per cycle or time step n. The stability of the solution is tested with the rate of change in displacement calculation. The algorithm stops once the difference between displacements of two cycles is below a threshold

ϵ set by the user. In other words, the iteration stops if $||\boldsymbol{u}^{(n)}(\boldsymbol{x},t) - \boldsymbol{u}^{(n-1)}(\boldsymbol{x},t)|| < \epsilon$. The final step is to calculate stress components with the stable solution parameters.

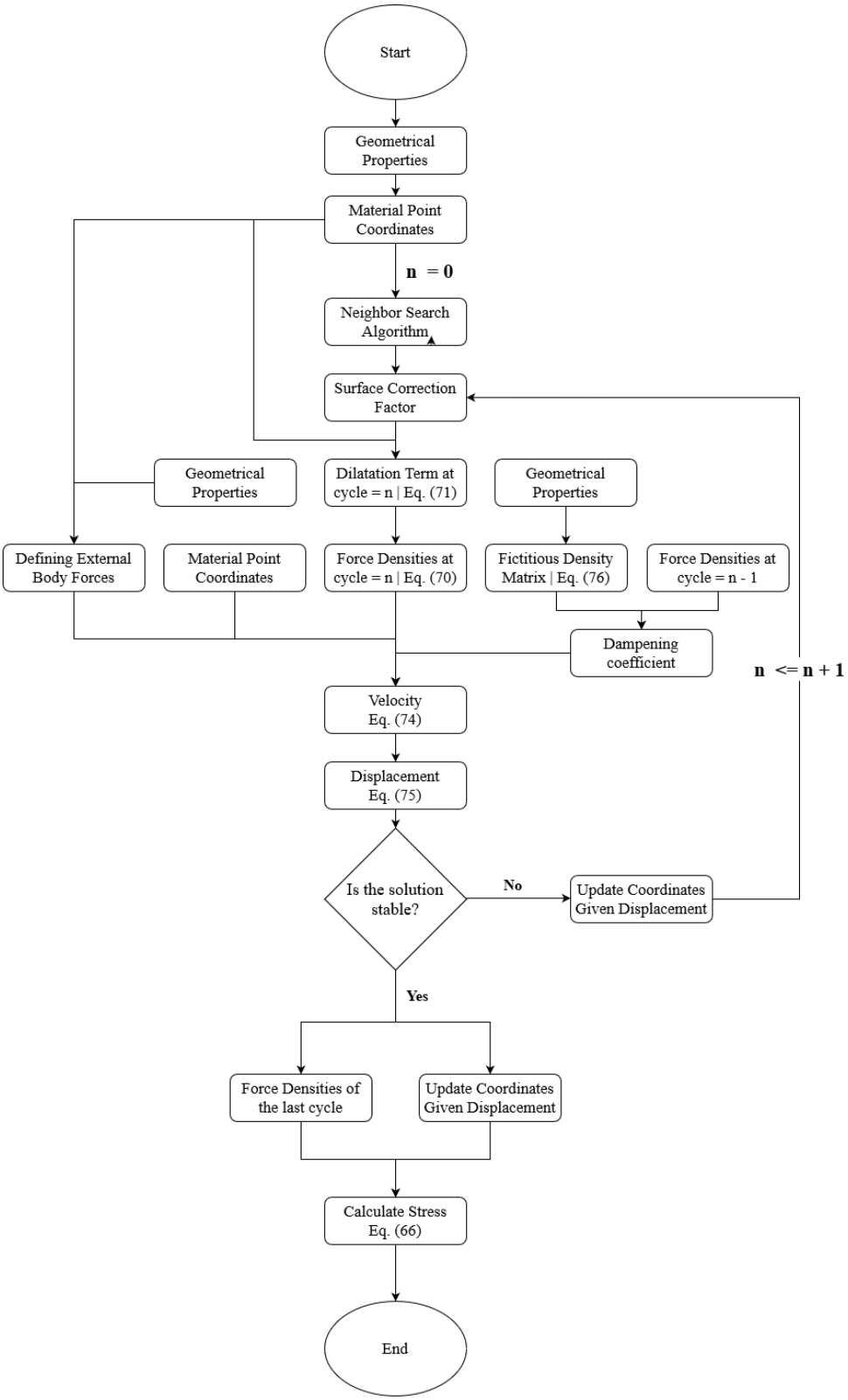

Figure 3.4. Flowchart of the DH-PD model progression

3.8. Summary of benchmark problems

The developed dual horizon peridynamic model is tested on the benchmark problem of a steel plate with a central hole under uniaxial tension. Several nomenclatures need to be defined in order to explain the nature of the following experiments. First, the concept of 'subdomain' is defined, which is the collective of all material points that share one horizon size. Given the usage of two horizon sizes in the current DH-PD model, the plate is separated into two subdomains, the remote subdomain Γ_r with the horizon size δ_r, and the local subdomain Γ_l with the horizon size δ_l. The local subdomain encompasses the central hole and stretches across the width of the plate. Any material point outside of this area is considered 'remote' and belongs to the remote subdomain Γ_r. Essentially in the case of these benchmark problems, all the areas of interest, including the high stress areas are in the local subdomain Γ_l (See Figure 3.5). The rest of the body is encompassed by the remote subdomain Γ_r. Throughout a simulation, each subdomain can be assigned a horizon size which in return defines the distance of material points Δx in that subdomain. Since δ and Δx are linearly correlated ($\delta = 3\Delta x$), assigning a small horizon size for a subdomain leads to a decrease in Δx and the subsequent increase in the number of subdomain material points (i.e. small horizon size equates to higher material point density in a subdomain).

Assigned horizon sizes remain constant per subdomain. The ratio of the subdomain horizon sizes, called horizon ratio ϕ, is an important hyperparameter whose effect on the accuracy and efficiency of the model is studied in Section 4.2, and is defined in Eq. (97).

$$\phi := \frac{\delta_r}{\delta_l} > 1 \tag{97}$$

Because the local subdomain Γ_l encompasses the high-stress locations, it is paramount that a finer discretization be used in Γ_l. This translates to a small horizon size δ_l. On the other hand, material points in subdomain Γ_r are considered remote in terms of distance from the high-stress locations, therefore a coarser discretization and a larger δ_r may be used. The horizon ratio ϕ, defined as δ_r divided by δ_l, is thus always larger than 1 (Eq. (97)).

The discretized plate is of the width and length of 0.5m. The Young's modulus and Poisson's ratio are 200GPa and 0.3, respectively. The central hole of the plate is of the elliptical shape and is

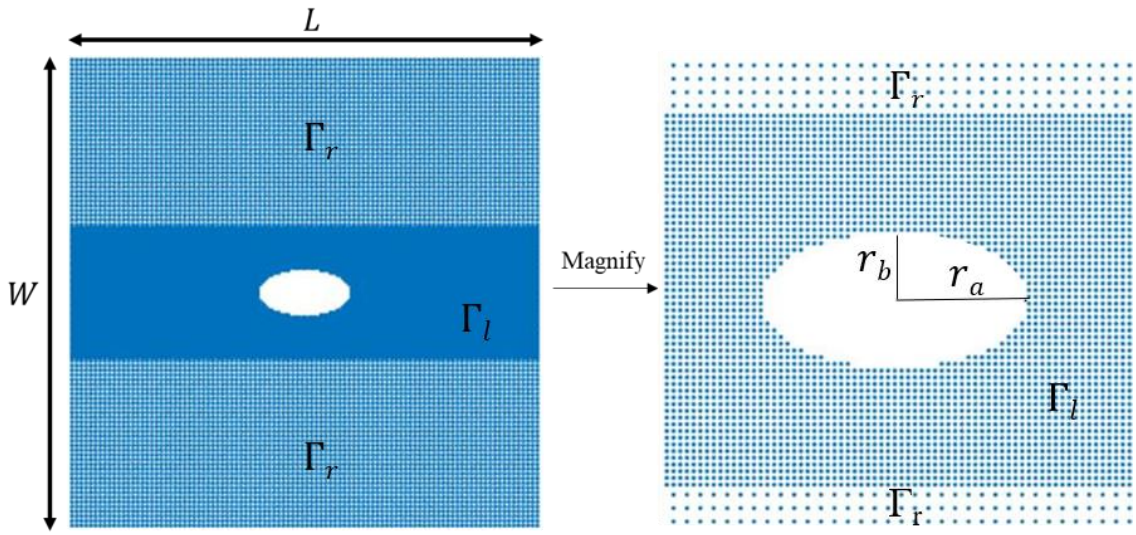

Figure 3.5. Schematic of the dimensional parameters in the DH-PD model of a steel plate with a central hole

denoted by a major radius r_a and a minor radius r_b. A parameter of interest in the following sections in the radius of the vertices on the major axis of the central hole ρ which is calculated by Eq. (98).

$$\rho := \frac{r_b^2}{r_a} \tag{98}$$

Chapter 4:

Results and Discussion

FE models are developed to test the validity of the developed peridynamic model. To make the two methods comparable, several constraints must be established. The FE model is discretized with structured linear quadrilateral elements with nodes corresponding to the material points in DH-PD, meaning that for every material point in DH-PD, there is an FE node in the same coordinates. In the areas of high curvature near the hole, the mesh shapes are deformed to fit the geometry. This is called adaptively refined mesh, which is refining the mesh size in areas prone to higher percentage of solution error. The material is homogeneous and linear isotropic, allowing a linear relation between displacement and force. The plastic zone near high stress concentration areas is assumed to be negligible.

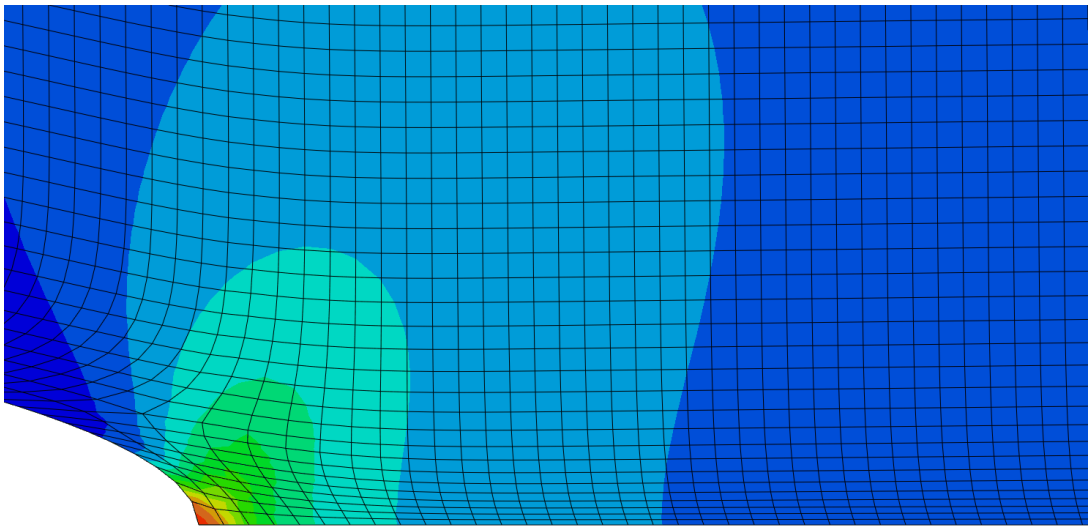

Figure 4.1. Close up schematic of the linear quadrilateral structured mesh used in FEM corresponding to peridynamic local horizon size of $\delta_l = 3.45mm$ and element size $\Delta x = 1.25mm$

The mesh element size in FEM corresponds to the cell size in DH-PD. The peridynamic cell size, equal to Δx, is measured as the distance of two material points in the peridynamic model. FEMs should thus be developed with quadrilateral mesh elements of average size of Δx. The cell size is inversely related to the subdomain material point density. A material points linear density of $D_l = 800m^{-1}$ corresponds to $\Delta x_l = 1.25mm$ (see Figure 4.1).

4.1. Impact of horizon size on displacement and stress accuracy

The steel plate with central hole of major radius $r_a = 5cm$ and minor radius $r_b = 0.6cm$ is

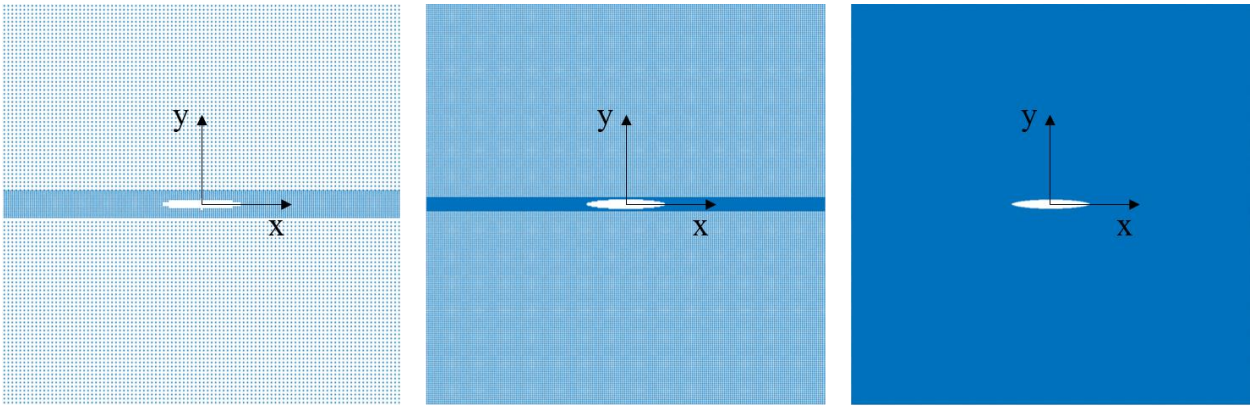

Figure 4.2. Three modes of discretization with a constant horizon ratio of $\phi = 2$ and varying remote horizon size of (a) $\delta_r = 7.5mm$, (b) $\delta_r = 3.75mm$, and (c) $\delta_r = 1.9mm$.

discretized into three modes. The remote horizon size is selected as $\delta_r = 7.5mm$, $\delta_r = 3.75mm$, and $\delta_r = 1.9mm$ per mode shown in Figure 4.2. The remote horizon size $\delta_r = 7.5mm$ corresponds to a material point linear density of 200 material points per meter. Dividing the remote horizon size by half will increase the linear density of material points in Figure 4.2.(b) to 400 material points per meter. Lastly, the remote horizon size $\delta_r = 1.9mm$ results in Figure 4.2.(c) in a linear density of 800 material points per meter in remote subdomains. The horizon sizes are thus selected to progressively double the linear density of material points from one discretization mode to another. The progressive increase of material points' linear density from one mode to another allows the observing of the influence of the number of material points on accuracy. The horizon ratio ϕ is kept constant in all three modes and is $\phi = 2$. This means that at the local subdomains, the density of material points is twice the density of material points at the remote subdomain in each mode. An increase in the number of material points around the curvature of the central hole is required to capture the contour of the elliptical-shaped hole more accurately. Table 4.1 summarizes the parameters used in these discretization modes.

Table 4.1. Discretization parameters of the three modes used to study the impact of horizon size on displacement and stress accuracy.

	$\delta_r(mm)$	$\delta_l(mm)$	ϕ	$\Delta x_r(mm)$	Density in $\Gamma_r(m^{-1})$	$\Delta x_l(mm)$	Density in $\Gamma_l(m^{-1})$
Mode (a)	7.5	3.75	2	2.5	200	1.25	400
Mode (b)	3.75	1.9	2	1.25	400	0.63	800
Mode (c)	1.9	0.95	2	0.63	800	0.32	1600

Figure 4.3 and Figure 4.4 provide a visual comparison of the contours depicting displacements u_x and u_y between the peridynamic approach and FEM. Notably, these figures depict the undeformed configuration. The outcomes reveal a consistent agreement between the calculated displacements in all three modes of discretization and their respective counterparts in FEM. Moreover, the results across the three modes exhibit close conformity, suggesting that the increase in material point density has a minimal impact on the accuracy of displacement calculations. Because of this, the minimum material point density, that is, the mode with the largest horizon size of $\delta_r = 7.5mm$ can be ruled as sufficient for this plate geometry. Keep in mind that this experiment does not prove that any horizon size is acceptable for this geometry. As will be shown in Section 4.2, a maximum horizon size exists, above which the model becomes unstable.

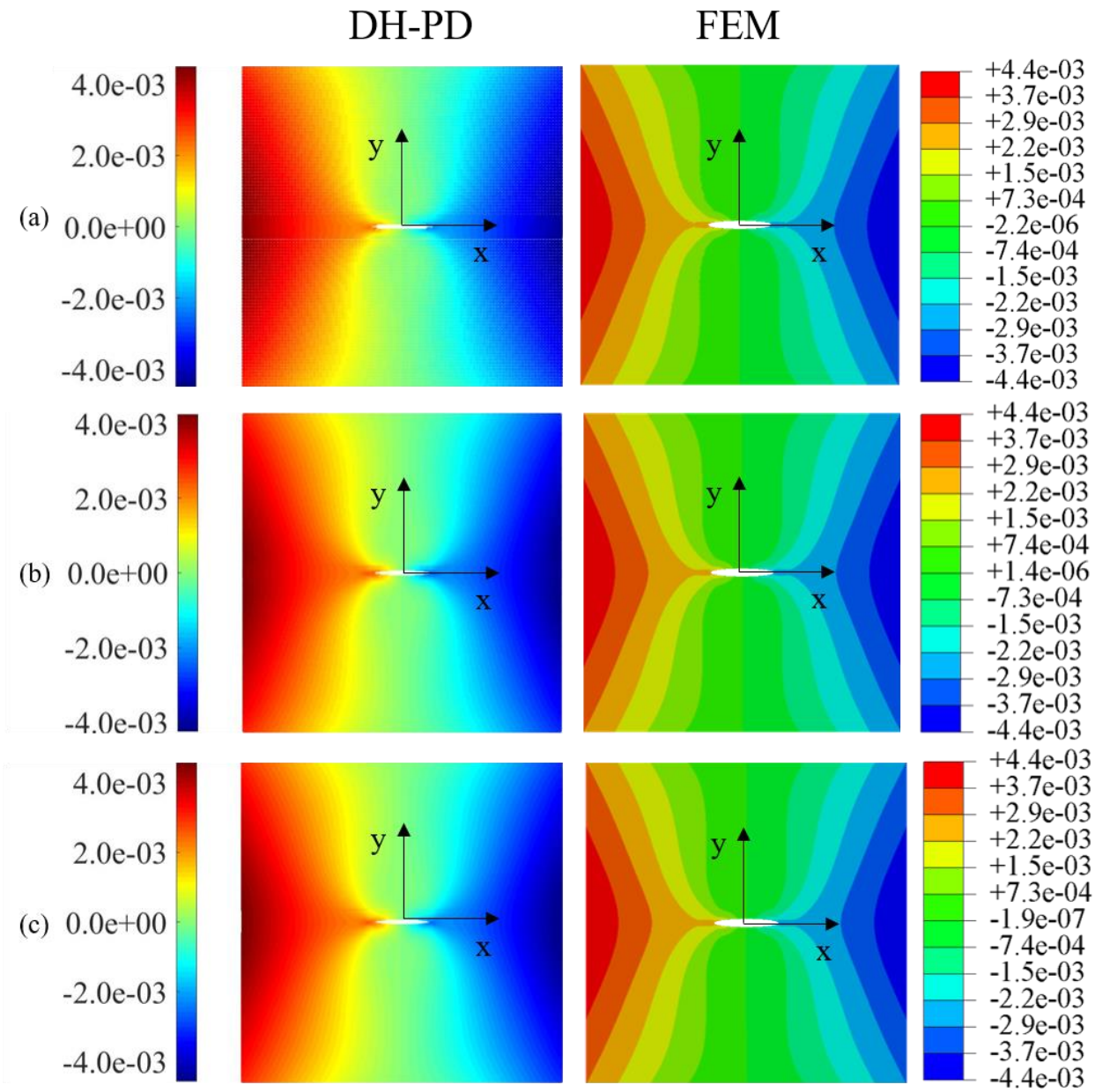

Figure 4.3. Displacement u_x (unit: mm) compared between DH-PD and its FEM counterpart for (a) $\delta_r = 7.5mm$, (b) $\delta_r = 3.75mm$, and (c) $\delta_r = 1.9mm$ given $\phi = 2$

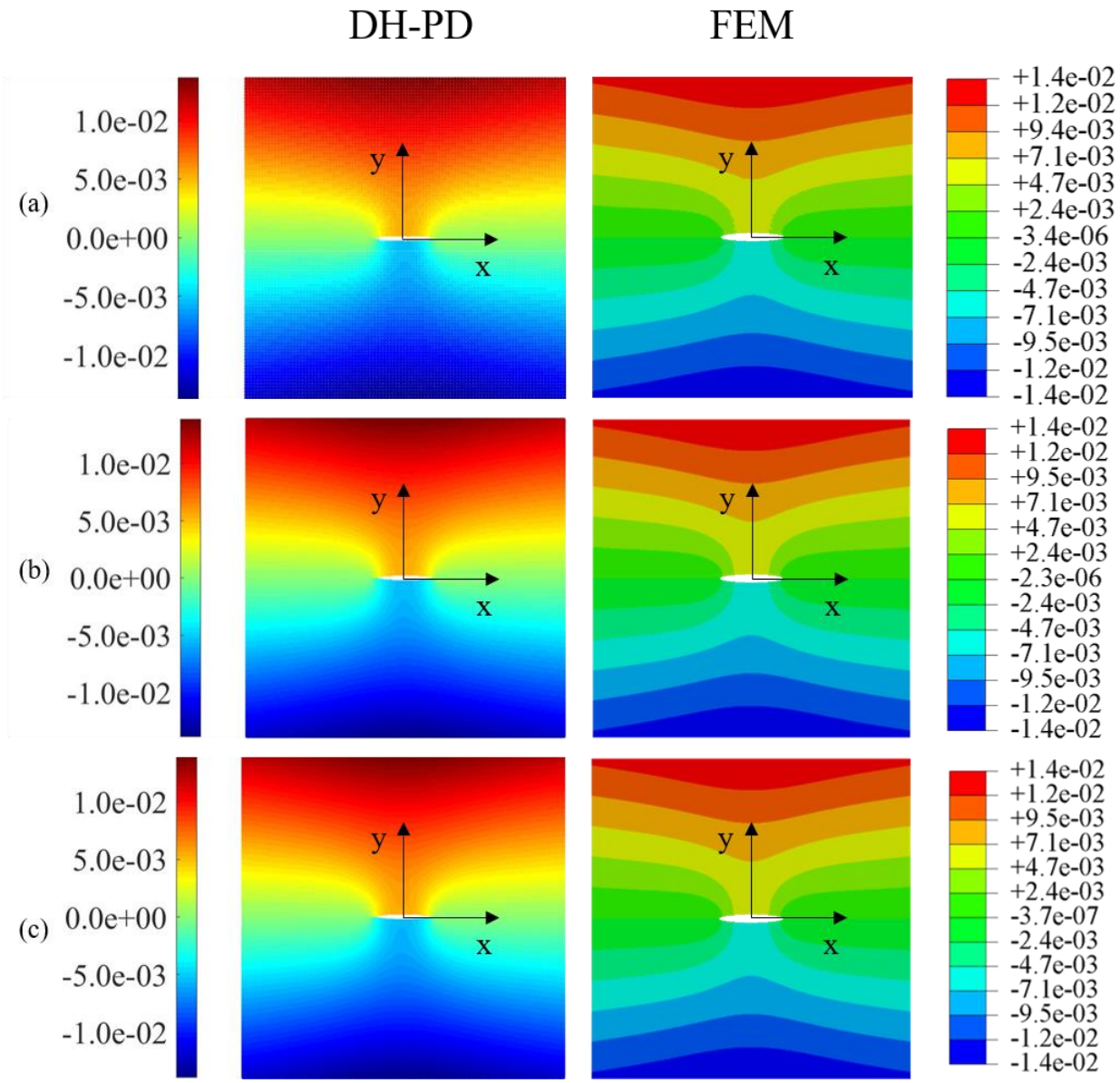

Figure 4.4. Displacement u_y (unit: mm) compared between DH-PD and its FEM counterpart for (a) $\delta_r = 7.5mm$, (b) $\delta_r = 3.75mm$, and (c) $\delta_r = 1.9mm$ given $\phi = 2$.

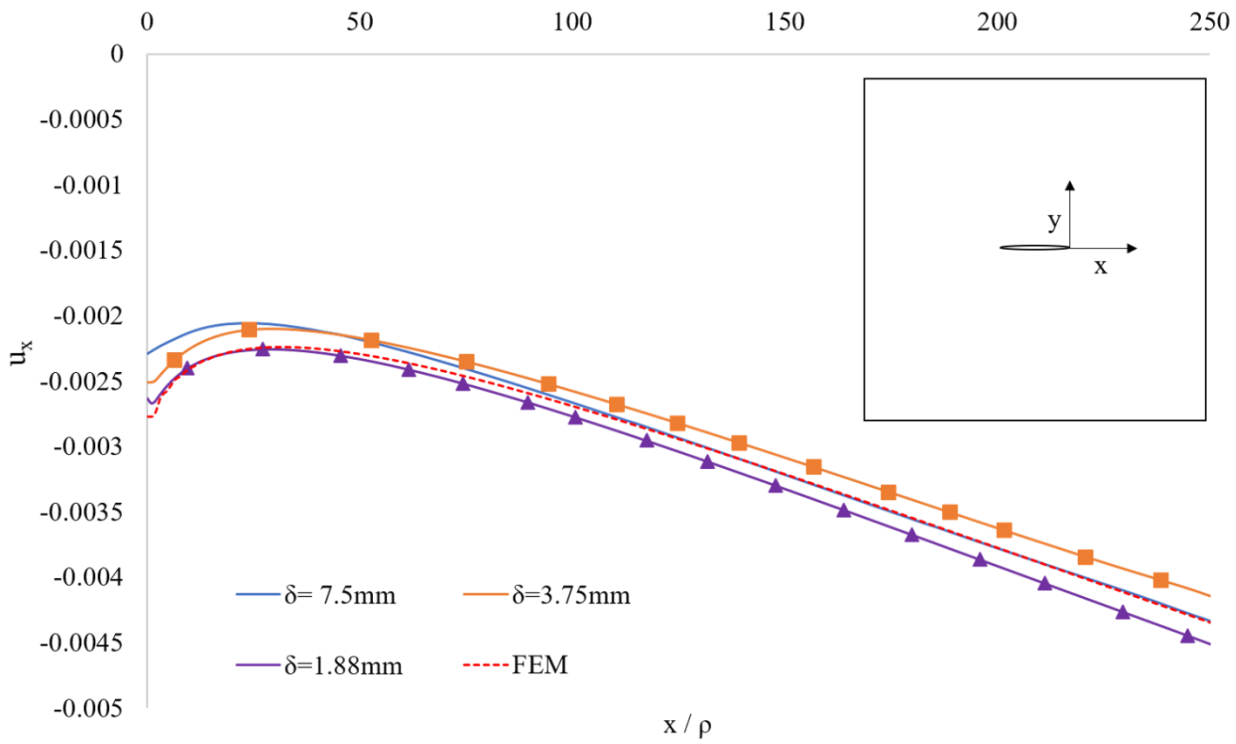

Figure 4.5. Comparison of u_x (unit:mm) on the line $y = 0$ at distance x normalized by ρ for $\delta_r = 7.5mm$, $\delta_r = 3.75mm$, $\delta_r = 1.88mm$ and FEM.

Figure 4.5 captures the displacement u_x along the line $y = 0$. The distance x on the line $y = 0$ is normalized with respect to the vertex radius of the central hole ρ. This allows a better understanding of displacement or stress component behavior in terms of distance relative to the curvature of the central hole. Equation (99) shows the norm-1 error equation used to calculate the difference between DH-PD and FEM results.

$$e = \frac{|u^{PD} - u^{FEM}|}{|u^{FEM}|} \tag{99}$$

As summarized in Table 4.2, the average norm-1 error percentages in measuring u_x for $\delta_r = 7.5mm$, $\delta_r = 3.75mm$, and $\delta_r = 1.88mm$ are $e = 2.3\%$, $e = 4.5\%$ and $e = 2.8\%$, respectively. At the distances of $x/\rho < 50$, the highest accuracy belongs to $\delta = 1.88mm$ with the error percentage of $e = 0.1\%$, matching the FEM results exactly. With further distance from the hole tip, the model with $\delta_r = 7.5mm$ converges with FEM results with an error percentage of

$e = 0.3\%$. This suggests that at the vicinity of the hole, finer discretization is desired, whereas coarser discretization can be used further away from the crack tip. Due to the symmetry of the benchmark problem and the experiment done under elastic conditions, the displacement u_y along the line $y = 0$ is zero across all three peridynamic modes and FEM.

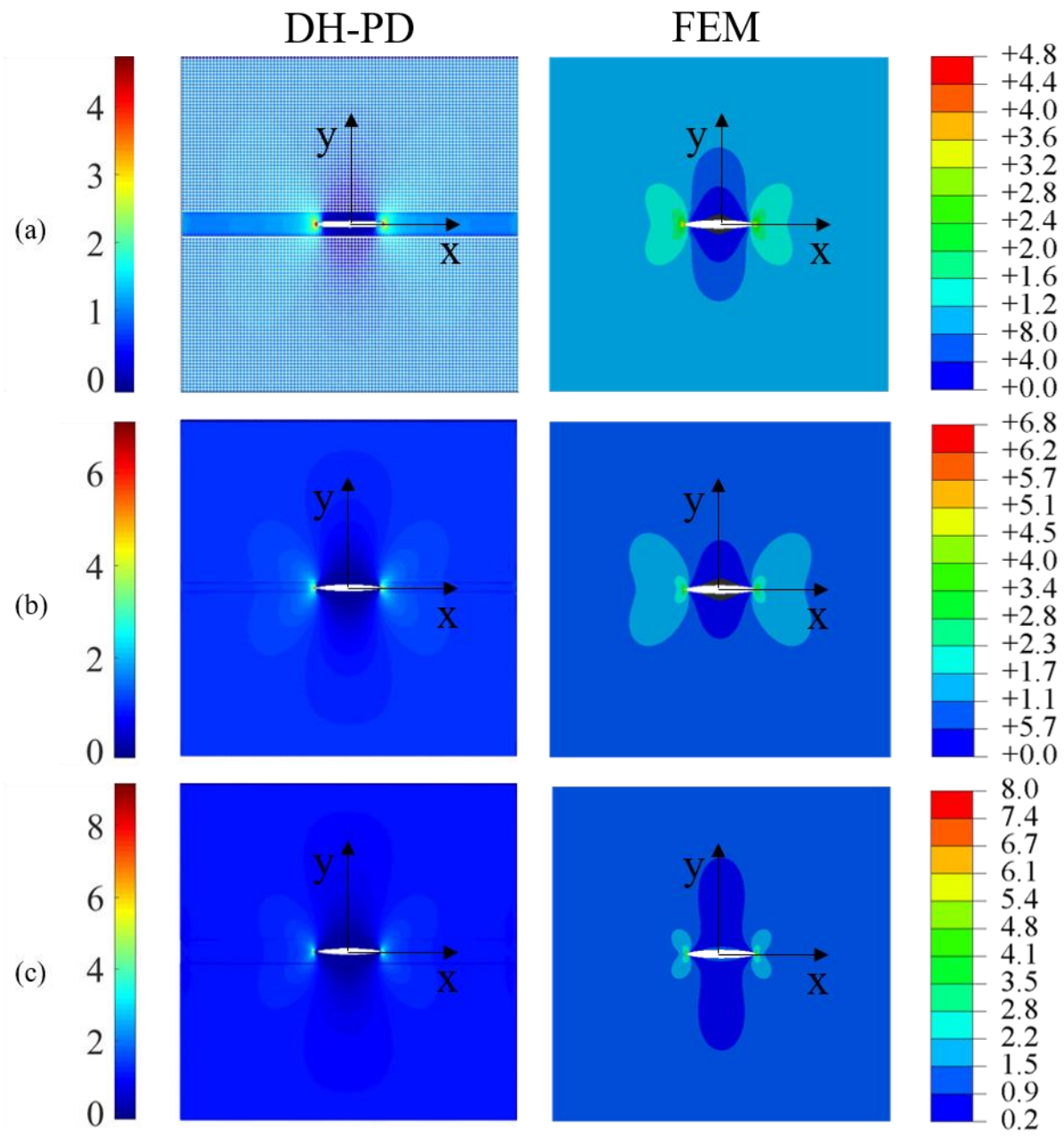

Figure 4.6. Normalized σ_{yy} with respect to the uniaxial tension S (unit: Pa / Pa) compared between DH-PD and its FEM counterpart for (a) $\delta_r = 7.5mm$, (b) $\delta_r = 3.75mm$, and (c) $\delta_r = 1.9mm$ given $\phi = 2$.

Table 4.2. The DH-PD total u_x norm-1 error percentage and average norm-1 error percentage for distances $x/\rho < 50$ and $x/\rho > 50$ given a constant $\phi = 2$ and varying δ_r configurations.

	Total norm-1 error	Norm-1 error: $x/\rho < 50$	Norm-1 error: $x/\rho > 50$
$\delta_r = 7.5mm$	2.3%	9.2%	0.3%
$\delta_r = 3.75mm$	4.5%	6.5%	4.0%
$\delta_r = 1.88mm$	2.8%	0.1%	3.5%

Figure 4.6 compares the stress component σ_{yy} contours in the peridynamic approach and FEM. The stress is normalized with respect to the uniaxial tension $S = 10MPa$. In comparison to FEM, stress contour can be captured accurately in DH-PD. The maximum value for σ_{yy} occurs at the hole tip.

Figure 4.7 compares σ_{yy} along the line $y = 0$, with the coordinate origin resting at the hole tip. The distance along the line $y = 0$ is normalized with respect to the tip curvature ρ. Here again the σ_{yy} is normalized by the uniaxial tension S. Given a constant geometry, with the decrease in δ, the maximum σ_{yy} measured in DH-PD increases. The increase is attributed to the fact that with more material points at the vicinity of the hole tip, the high stress concentration occurring can better be captured. With δ converging to zero, the plot converges towards the analytical solution.

Figure 4.8 compares DH-PD measured stress component σ_{yy} along the line $y = 0$ of each discretization mode with their FEM counterpart. As was mentioned in Section 3.8, for each discretization mode, FEM mesh is adjusted so that each node in FEM corresponds to a material point in DH-PD, and with elements corresponding to a material point cell, both in size, shape, and location. Figure 4.8 demonstrates that with comparable meshing and discretization in FEM and DH-PD, the results of DH-PD is close to their FEM counterparts. At the distance of $x/\rho = 5$ (i.e. $x = 4mm$ given $\rho = 0.78mm$) stress plots of FEM and DH-PD converge for $\delta_r = 1.88mm$ and $\delta_r = 3.75mm$. In $\delta_r = 7.5mm$, there is a discrepancy between FEM and DH-PD up to $x/\rho = 15$, followed by convergence.

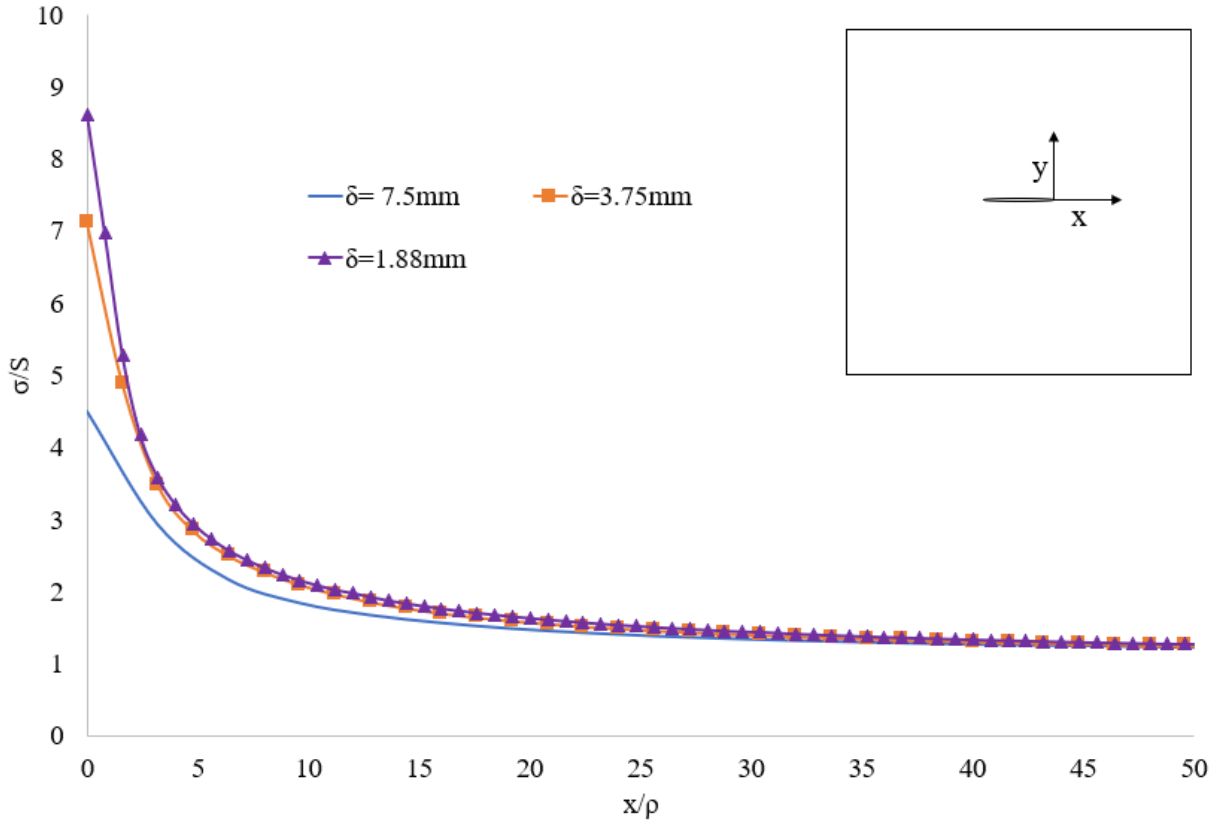

Figure 4.7. Comparison of normalized σ_{yy} (unit:mm) on the line $y = 0$ at distance x normalized by ρ for $\delta_r = 7.5mm$, $\delta_r = 3.75mm$, and $\delta_r = 1.88mm$.

Figure 4.9 shows the norm-1 error percentage in σ_{yy} measurement along the line $y = 0$. The distance along the line $y = 0$ is normalized with respect to the horizon size δ_l. In all the three modes, there is a higher error rate for material points right at the tip of the hole followed by a sharp error rate drop to below 5%. Similarly, there is a spike in error at the end of the path, by the edge of the plate. In all the modes, the sharp spikes in error rate occurs for the material points whose circular horizon overreaches the boundaries of the plate. This is caused by material points near the edges of the plate whose horizons are not symmetrical.

The abovementioned phenomenon, called the "skin effect", was originally reported by Ha and Bobaru [60] . The skin effect occurs because it is required that the horizon be symmetrical. In other words, the balance laws are not violated if the material point horizon is well within the boundaries of the body. The skin effect is similar to a "softening" of the material around the boundaries, that

is, its effect is similar to a reduction in Young's modulus and Poisson's ratio. For a given displacement, lower stress is calculated using Hook's law for a material that has a lower

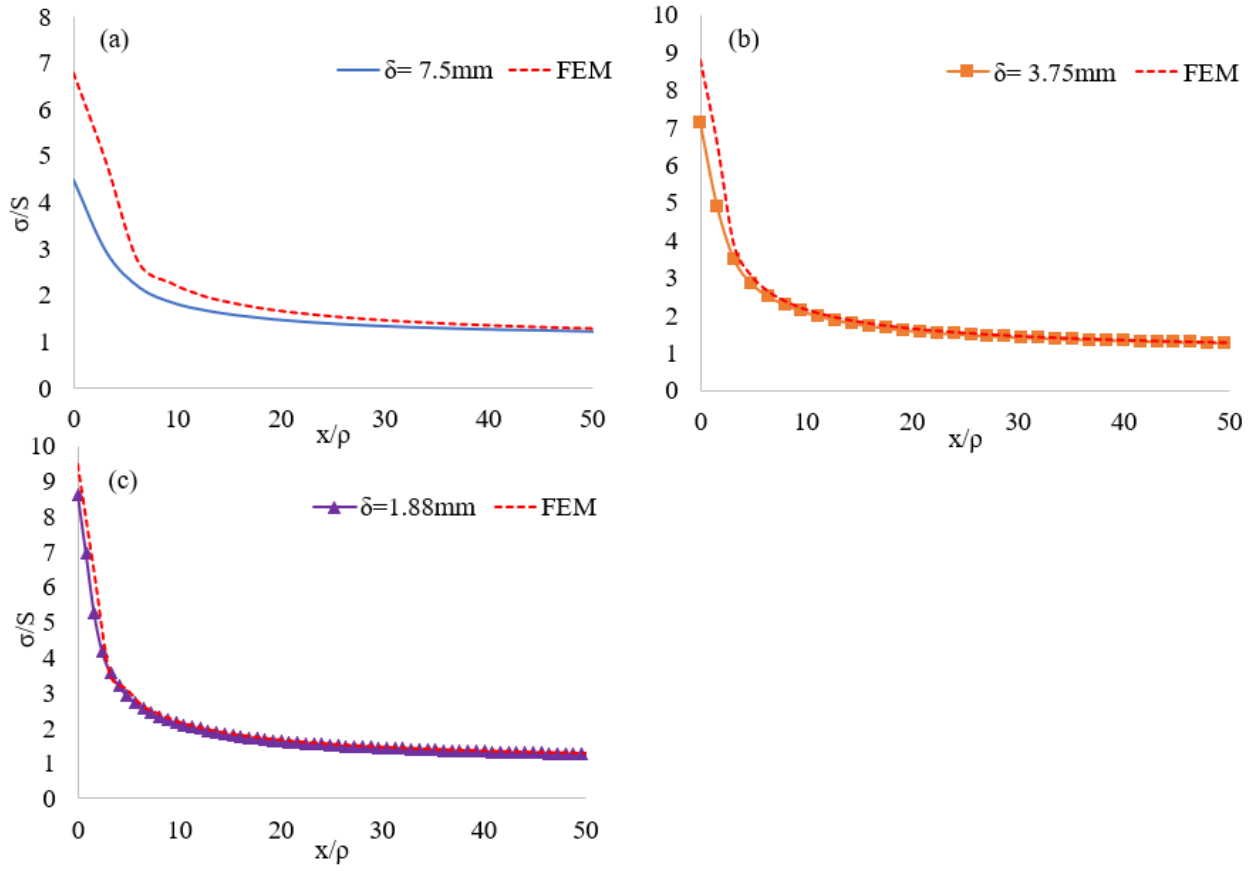

Figure 4.8. Inspection of the degree of agreement between DH-PD and its FEM counterpart calculation of normalized σ_{yy} along the line y = 0 for a) $\delta_r = 7.5mm$, b) $\delta_r = 3.75mm$, and c) $\delta_r = 1.88mm$.

Young's modulus. This is the main explanation behind the lower stress values calculated for material points adjacent to the hole tip.

Multitude techniques are available to alleviate the skin effect. In the case of applying the boundary conditions, which do not occur naturally in nonlocal theories such as peridynamics, a fictitious layer can be utilized, mentioned in Section 3.7. The softened regions caused by skin effect in peridynamics are of the thickness of δ, therefore a fictitious layer of minimum thickness δ can be used in locations where skin effect occurs [132, 133, 134]. Another method is to modify the micro-modulus formulation at the boundaries, as the skin effect is the cause of using the same micro-modulus as those produced for the bulk nodes [60]. The modification of the micro-modulus

formulation at the boundaries reduces the skin effect. Note that since the skin effect occurs at a maximum thickness of δ around the boundaries, the smaller the horizon is, the smaller the region affected by skin effect becomes. The skin effect does not have an overall noticeable effect on damage and crack propagation studies as the initiation and crack propagation is dependent on the energy available at the vicinity of the crack tip, which is inherently a nonlocal entity and is not dependent on a single element or material point.

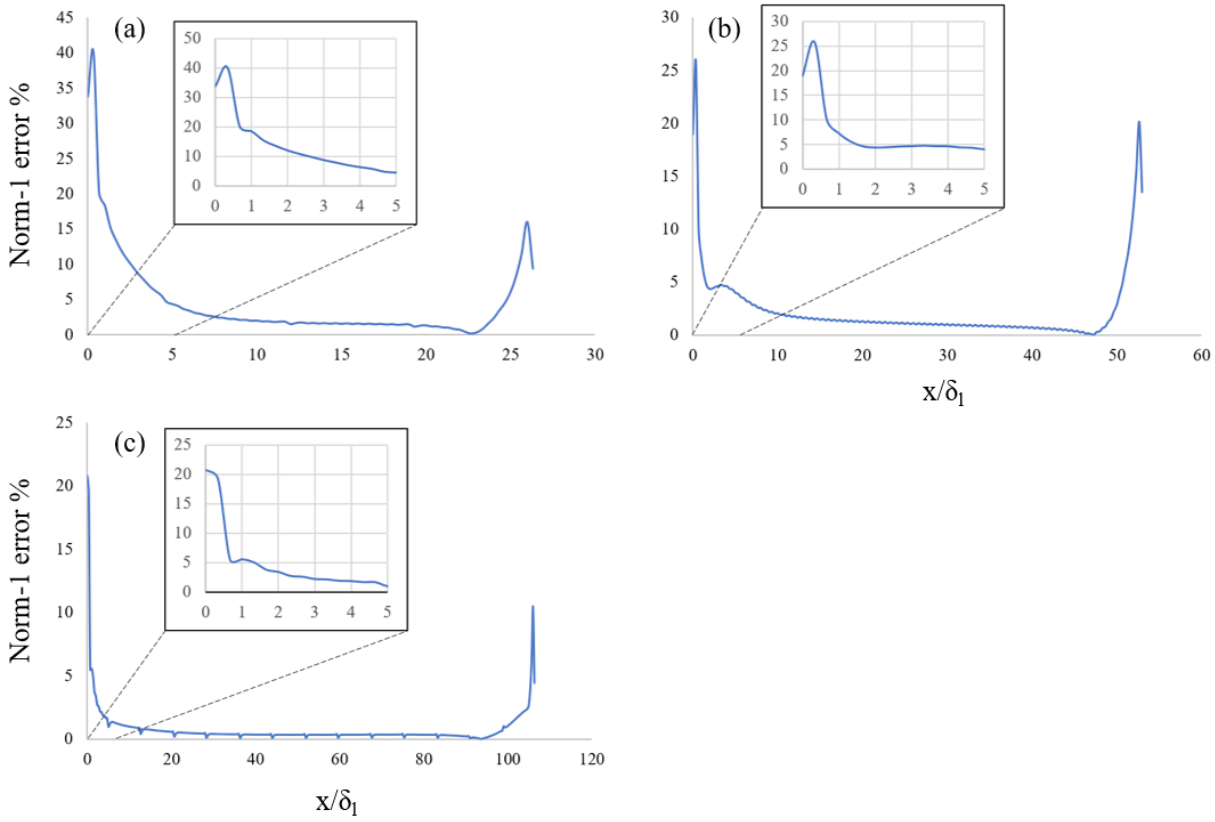

Figure 4.9. Norm-1 error percentage of normalized σ_{yy} along line $y = 0$ at a at distance x normalized by δ_l for a) $\delta_r = 7.5mm$, b) $\delta_r = 3.75mm$, and c) $\delta_r = 1.88mm$.

The peridynamic approach is capable of modelling damage propagation despite the skin effect [123, 120]. Moreover, several studies have focused on the calculation of nonlocal J-integral and have concluded that the peridynamic J-integral formulation, based either on either displacement or stress fields, is accurate within 2% to 5% percentages of error, irrespective of the skin effect [135], since the J-integral formulation is based only on the nearest neighboring material points of the contour integral [136]. Several trends can be pointed to in Figure 4.9, first, the error drops

sharply at the distance of $x/\delta_l = 1$, into a plateau before rising sharply again at the right edge of the plate. At the vicinity of the hole tip, the drop becomes sharper as δ_l gets smaller. This means that to alleviate the skin effect, a small horizon size should be used around areas where the horizon shape may not be symmetrical (e.g. near crack tips, edges, etc.). Secondly, the maximum error drops with the decrease of δ_l. This means that the discretization mode with the highest density of material points is more accurate when compared with its FEM counterpart. Summarized in Table 4.3, the lowest norm-1 error percentage belongs to $\delta_r = 1.88mm$ mode, with e = 0.8%. The lowest error rate for the distance range of $x/\delta_l < 1$ also belongs to mode $\delta_r = 1.88mm$, with e = 12%.

Table 4.3. The DH-PD total σ_{yy} norm-1 error percentage and average norm-1 error percentage for distances $x/\delta_l < 1$.

	σ_{yy} total norm-1 error	σ_{yy} norm-1 error: $x/\delta_l < 1$
$\delta_r = 7.5mm$	4.7%	28.1%
$\delta_r = 3.75mm$	2.3%	15.5%
$\delta_r = 1.88mm$	0.8%	12%

4.2. Impact of horizon ratio on displacement and stress accuracy

The optimization of the horizon size ratio ϕ is studied in this section. Given the formulation of this ratio in Eq. (97), the increase in ϕ, given that δ_l is constant, results in an increase in δ_r, which is desirable in terms of computation efficiency.

This section focuses on investigating how an important parameter, ϕ, influences the stability of the solution for a steel plate containing a central hole. This steel plate has specific geometric characteristics: it has a major radius, denoted as r_a , equal to 5 cm and a minor radius, denoted as r_b , equal to 0.5 centimeters. To conduct this study, the plate is divided into three different modes or configurations for analysis.

In all three modes, the local horizon size, δ_l, remains constant at 1.88 mm. What varies among these modes is the value of the parameter ϕ, which is set at three different magnitudes: 2, 4, and

8. The discretization or division of the steel plate for analysis is shown in Figure 4.10, where the differences in discretization between these three modes are visually compared. It's important to note that with the given values of ϕ and δ_l, the remote horizon, denoted as δ_r, is determined to be 3.75 mm, 7.5 mm, and 15 mm, respectively, for the three modes.

To assess the accuracy of the analysis, Figure 4.11 and Figure 4.12 present a comparison of the displacement components, u_x and u_y , as calculated by the DH-PD approach, against the Finite Element Method (FEM) solution. In the FEM solution, a mesh is used with elements of size equal to the material point cell size, Δx, which is equal to 1.88/3 mm, corresponding to $\delta_l = 1.88$ mm. The primary objective here is to compare the results obtained from the DH-PD modes among themselves and with the FEM solution. Since the discretization is the same for the three modes in the local subdomain and is only different in the remote areas, only one FEM model is developed as a reference point, with a uniform mesh density across the area of the plate corresponding to the material point density of the local subdomain with $\delta_l = 1.88mm$

The figures demonstrate that the displacement contour is accurately captured by the modes with ϕ equal to 2 and 4, However, the third mode, which corresponds to $\phi = 8$, fails to accurately represent the displacement contours. This leads to a possible conclusion that there is a maximum magnitude allowable for ϕ, which is a hyperparameter controlling the disparity of material point density between the two subdomains Γ_l and Γ_r.

To address this issue and stabilize the model when ϕ is set to 8, a specific adjustment is tried. The width of the local subdomain, denoted as Γ_l, is increased by 200%. This revised discretization ensures that any material points located on either side of the local subdomain Γ_l will not recognize each other as neighbors, thus stabilizing the model under these conditions. The comparison is shown schematically for a query material.

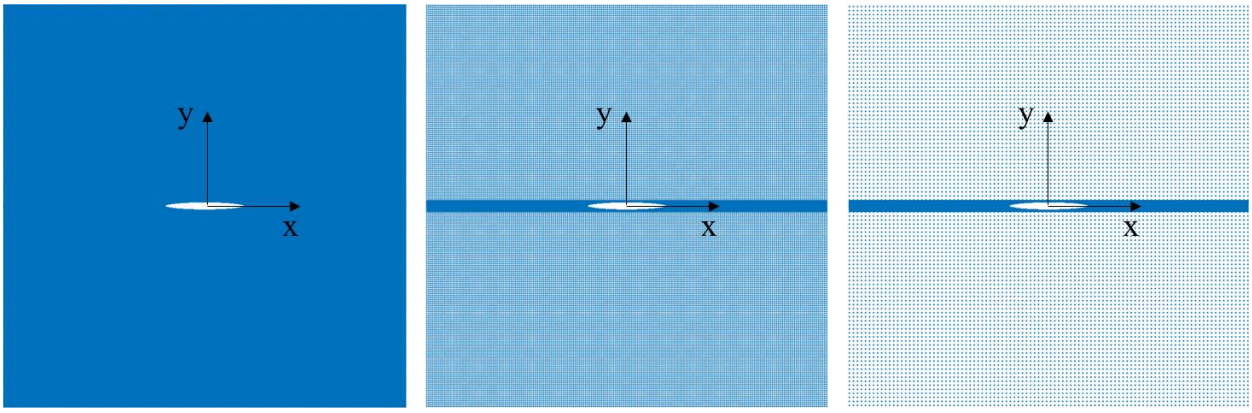

(a) (b) (c)

Figure 4.10. Three modes of discretization with a constant local horizon size of $\delta_l = 1.88m$ and varying horizon ratio of (a) $\phi = 2$, (b) $\phi = 4$, and (c) $\phi = 8$.

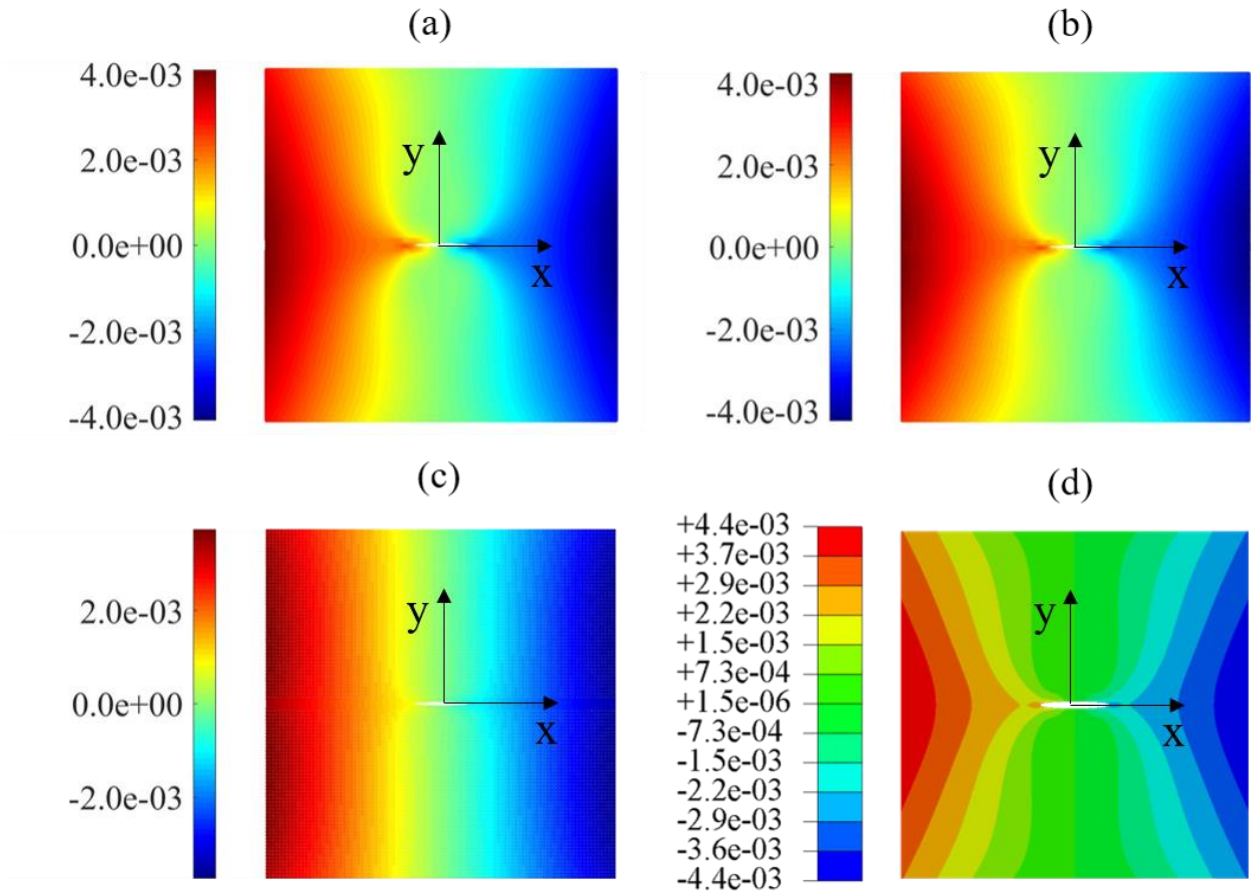

Figure 4.11. Displacement u_x (unit: mm) compared between DH-PD and its FEM counterpart for (a) $\phi = 2$, (b) $\phi = 4$, (c) $\phi = 8$ (unstable) and d) FEM, given $\delta_l = 1.88mm$.

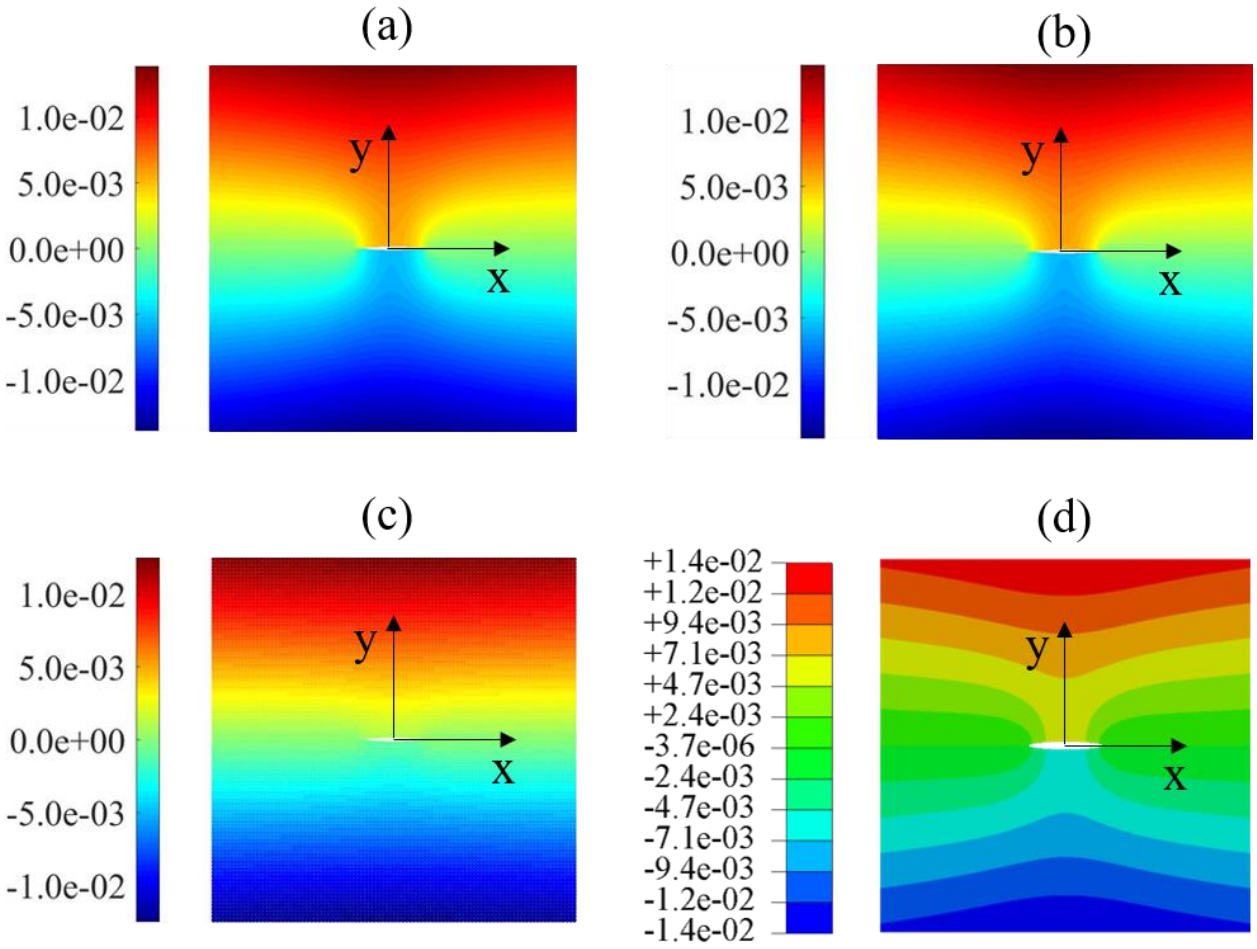

Figure 4.12. Displacement u_y (unit: mm) compared between DH-PD and its FEM counterpart for (a) $\phi = 2$, (b) $\phi = 4$, (c) $\phi = 8$ (unstable) and d) FEM, given $\delta_l = 1.88mm$.

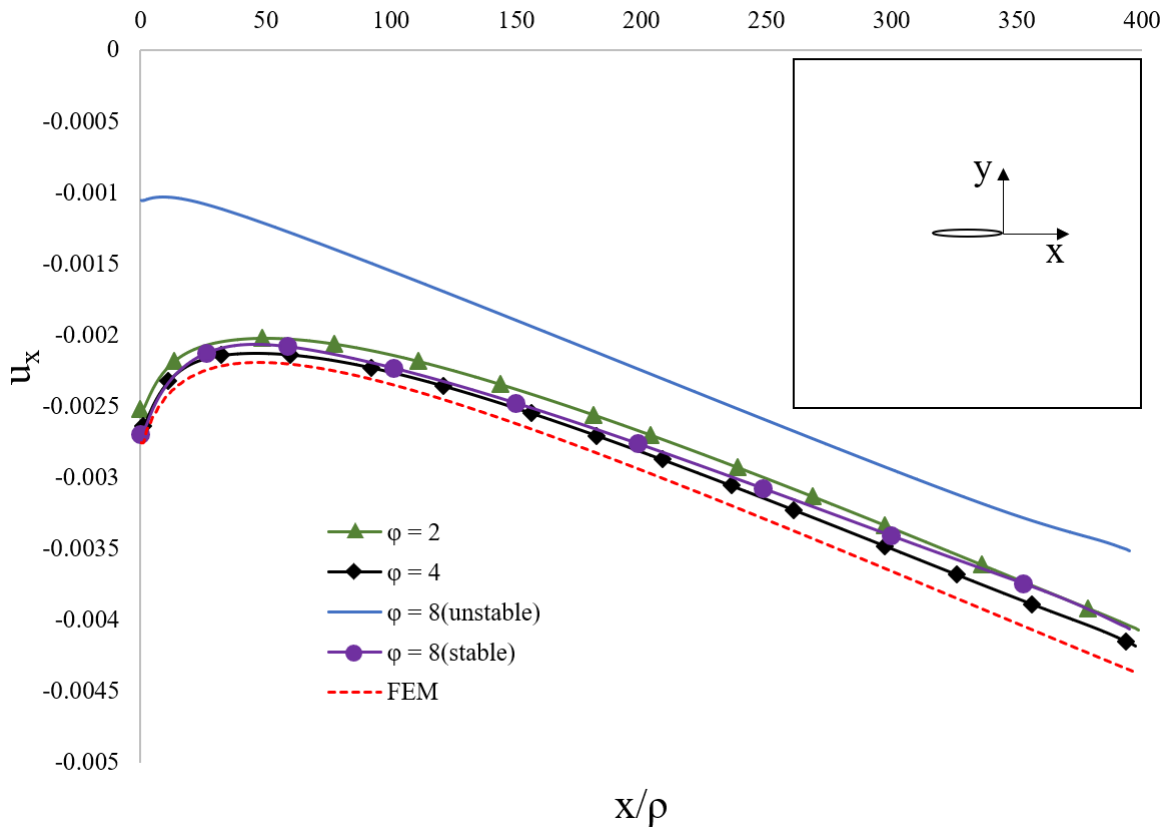

Figure 4.13. Comparison of u_x (unit: mm) on the line $y = 0$ at distance x normalized by $\rho = 0.05cm$ for $\phi = 2$, $\phi = 4$, $\phi = 8$ (unstable), $\phi = 8$ (stable), and FEM.

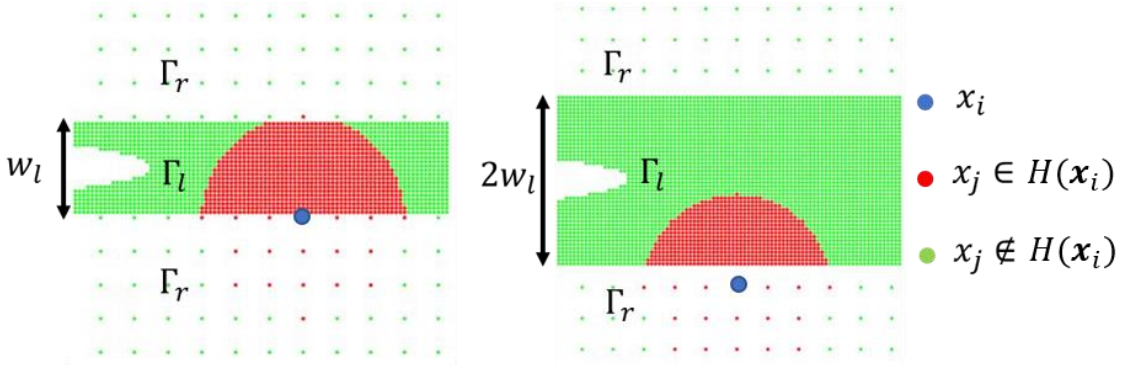

Figure 4.14. The increase in width of the local subdomain stabilizes the DH-PD solution for $\phi = 8$

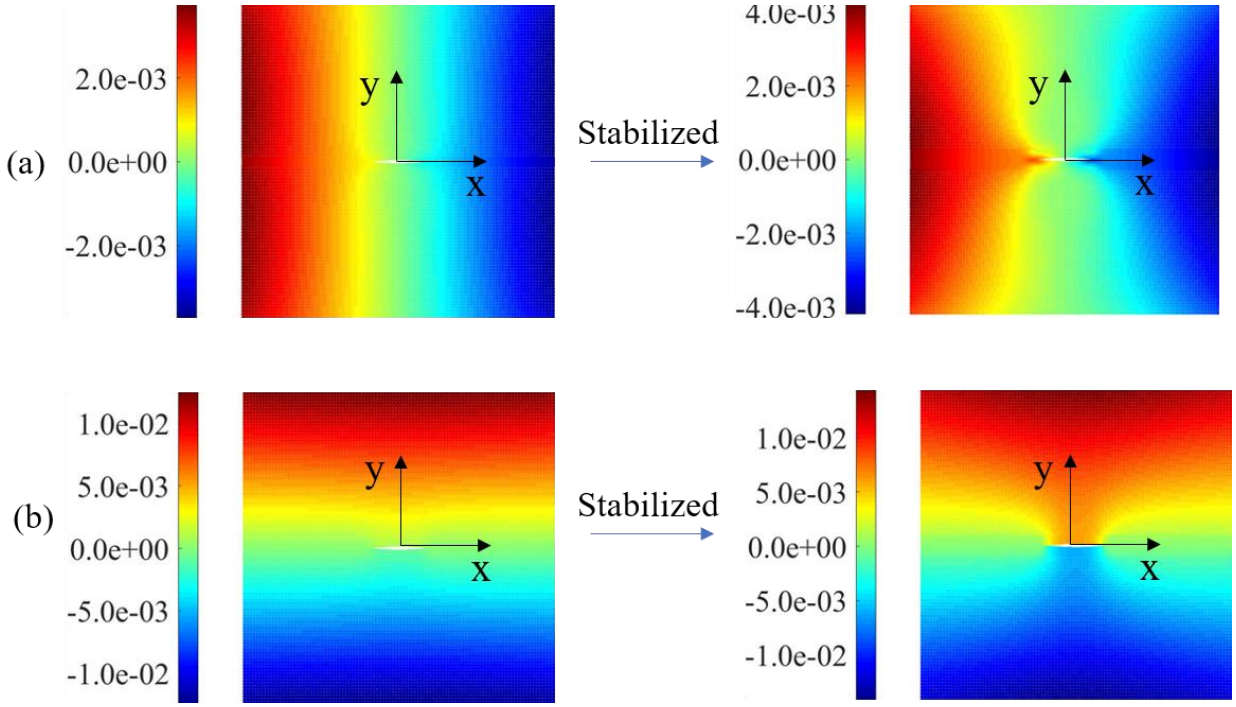

Figure 4.15. Displacement field stabilization in (a) u_x, and (b) u_y (unit: mm) shown for configuration $\phi = 8$ undergoing an increase in width of the local subdomain.

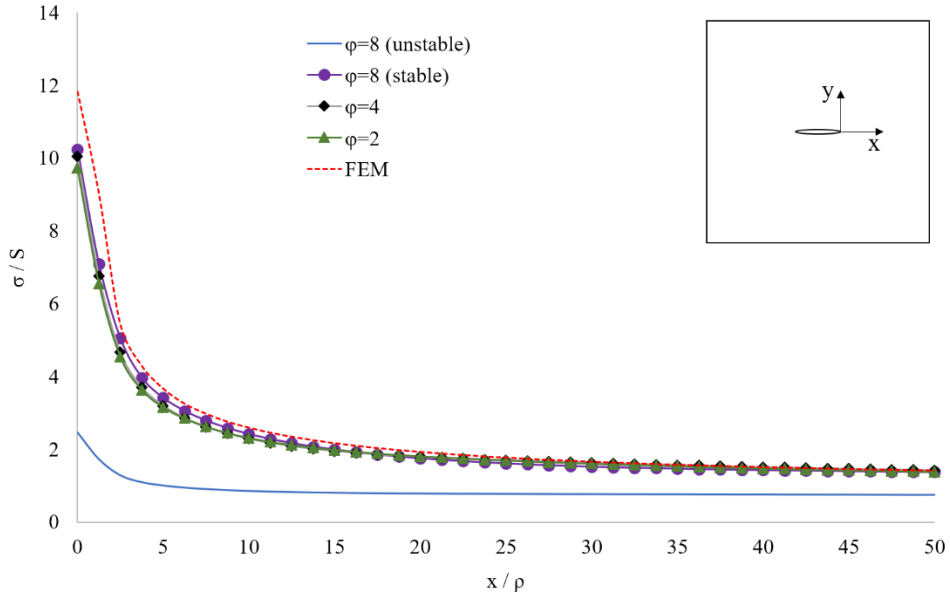

Figure 4.16. Comparison of normalized σ_{yy} (unit: Pa/Pa) on the line $y = 0$ at distance x normalized by $\rho = 0.05cm$ for $\phi = 2$, $\phi = 4$, $\phi = 8$ (unstable), $\phi = 8$ (stable), and FEM.

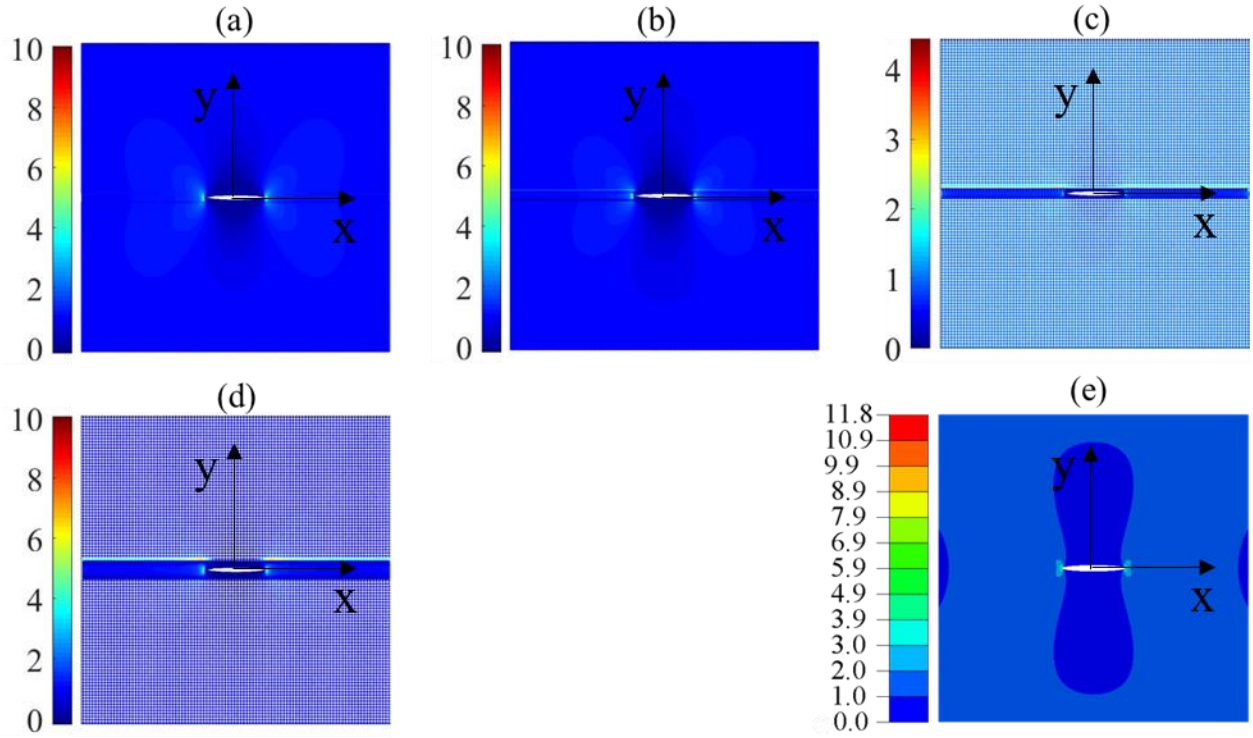

Figure 4.17. Contour of normalized σ_{yy} with respect to S (unit: Pa/Pa) compared between DH-PD and its FEM counterpart for (a) $\phi = 2$, (b) $\phi = 4$, (c) $\phi = 8$ (unstable), d) $\phi = 8$ (stable) and e) FEM, given $\delta_l = 1.88mm$.

point x_i in Figure 4.14 which has stabilized the stress and displacement calculation. It appears that the width of the local subdomain Γ_l should be at least larger than half of the largest horizon size used in the model, i.e. the inequality in Eq. (100)

$$W_{\Gamma_l} > \frac{Max(\delta(x_i))}{2}, \qquad \forall x_i \in \mathfrak{B} \tag{100}$$

With the DH-PD approach in this study, the largest horizon size is equal to the remote horizon size δ_r . The displacement contour of the stabilized mode with $\phi = 8$ is shown in Figure 4.15. Figure 4.14 shows the displacement component u_x along the line $y = 0$ for the three modes of DH-PD and compares with FEM results. The modes $\phi = 2$, $\phi = 4$, and the stabilized $\phi = 8$ all show accurate displacement results when compared with FEM. The norm-1 displacement u_x error percentage is demonstrated in Table 4.4. The highest accuracy at distances of $x / \rho < 50$ belongs

to mode $\phi = 4$ with the error rate of $e = 3.3\%$. In terms of total norm-1 error, the mode $\phi = 4$ again has the lowest error rate.

Table 4.4. The DH-PD total u_x norm-1 error percentage and average norm-1 error percentage for distances $x/\rho < 50$ and $x/\rho > 50$ given a constant $\delta_l = 1.88mm$ and varying ϕ configurations.

	Total norm-1 error	Norm-1 error: $x/\rho < 50$	Norm-1 error: $x/\rho > 50$
$\phi = 2$	8.1%	7.7%	8.2%
$\phi = 4$	3.7%	3.3%	3.8%
$\phi = 8\ (unstable)$	28.5%	52.5%	25.0%
$\phi = 8\ (stable)$	5.7%	4.5%	5.8%

Figure 4.16 shows the comparison of the normalized stress component σ_{yy} plot along the line $y = 0$, respectively. Except for the unstable $\phi = 8$, the other modes closely follow a similar trajectory. Like the displacement field, the stabilization of stress calculation depends on the satisfaction of Eq. (100). The Average maximum normalized σ_{yy} with respect to S predicted by the three modes is 10. The Maximum normalized σ_{yy} with respect to S predicted by FEM is 11.8.

All three stable modes show little variance in accuracy in both the displacement and stress components, which leads to the conclusion that as long as Eq. (100) is satisfied, the calculations are independent of the magnitude of ϕ. In other words, the highest magnitude of ϕ that satisfy Eq. (100) can be used to ensure computational efficiency.

Chapter 5:

Conclusions and recommendations

5.1. Conclusion

An advanced extended dual-horizon peridynamic model has been implemented, drawing inspiration from Lehoucq and Silling's work [105] on the SB-PD framework. This model exhibits the capability to accurately assess the stress component parallel to the applied load. To achieve this, explicit integration techniques were employed to solve the peridynamical equations and measure displacement fields. The primary focus was on a well-known benchmark scenario involving a 2D steel plate with a central hole subjected to tension.
To develop the model, the principles of the peridynamic approach is outlined.

The difference between the dual horizon and single horizon peridynamic as well as modes of peridynamic models such as bond-based and state-based peridynamics are summarized in the literature review. The methodology involves around developing a dual-horizon peridynamic model with implemented volumetric and surface correction factors. To make the peridynamic model capable of solving quasi-static problems such as the abovementioned benchmark problem, the adaptive dynamic relaxation technique is introduced and implemented.

The investigation in this study revolves around the impact of two critical factors on the accuracy of stress calculation in a DH-PD model: the density of material points and the ratio between the peridynamic horizon sizes employed in the model. FEM solution of benchmark problems is utilized to test the accuracy of the model. It is shown that the DH-PD displacement components match closely with their FEM counterparts. Moreover, the increase in the density of material points (i.e. decrease in the horizon size) does not lead to more accuracy in the displacement calculation. It is therefore computationally preferable to use the largest horizon size possible for discretization. In the calculation of the normal stress component, it is shown that with the decrease in horizon size, the model can capture higher stress concentrations. This pattern is similar to that of using finer mesh in FEM near areas of high-stress concentration. It is also observed that the decrease in horizon size leads to lower error rates. Skin effect is shown to affect the accuracy of stress calculation near the boundaries of the plate body. At the boundaries of the solution body, due to the horizon of material points becoming asymmetrical, a “softening of the material” effect occurs, leading to lower maximum stress calculated in DH-PD near the boundaries. However, the error rate is shown to drop drastically to below 5% at a distance of one horizon away from the edges.

The effect of the horizon ratio hyperparameter ϕ is investigated on stress and displacement calculation and their computational efficiency. Given the description of ϕ, the higher horizon ratio is more desirable in terms of time efficiency. It is shown that below a maximum threshold for ϕ, the value of the horizon ratio does not influence the accuracy. However, if the maximum threshold is exceeded, a sudden transition from low-density to high-density regions occurs, resulting in instability in stress measurements. It is important to note that this critical density ratio is influenced by the specific geometric characteristics of the benchmark problem, and its determination often necessitates a trial and error approach. An experimental equation is introduced that serves as a rule of thumb to find the maximum stable ϕ in a two-dimensional quasi-static problem.

In summary, the effectiveness of the dual-horizon peridynamic model in accurately calculating stress components in complex structures is showcased. Furthermore, the importance of tailoring the material point density to the specific geometric features of the problem is emphasized, as exceeding a critical density ratio can lead to measurement instability in multi-horizon peridynamics.

Some limitations of this model should be mentioned. The experimental nature of the density ratio ϕ makes it difficult to find a ϕ suitable for all geometries, therefore the optimum ϕ must be found by trial and error. As was mentioned, an experimental upper bound for ϕ is found for the specific benchmark problems studied. Moreover, the computation time rises exponentially with the increase of material point density. This is due to the $O(N^2)$ time complexity of the algorithms used to calculate peridynamic force densities. Lastly, the current model is limited to calculating the normal stress components. However, with given equations for stress calculation in peridynamics, it is possible to calculate shear stress components as well. Of course, these additional calculations must justify the increase in overall time cost and complexity.

5.2. Further research and recommendation

There exist multiple ways to develop more complex models based on the study summarized in this dissertation. The model itself can be improved in the following cases:

- Three-dimensional problems: The model shown in this study was only studied on two-dimensional benchmark problems. The peridynamic constitutive laws are general in the

sense of dimensionality and the principles used here for two-dimensions can easily be transformed to be applicable to three-dimensional problems.

- Adaptive discretization: The discretization shown in this study is done manually by the user and the horizon size along with the position of local and remote subdomains is chosen based on the user's judgment. An adaptive discretization technique can be used that similar to FEM software such as ABAQUS and ANSYS, can automatically detect areas of interest such as highly curved edges or cracks and use higher density of material points at the vicinity of those locations.
- Skin-effect elimination: It is alluded to in this study that there are ways to mitigate the skin-effect. The recommended approach is to change the micropotential equation for the material points at the edges of the plate to eliminate the skin effect.
- Full stress tensor calculations: The study can be extended to calculate all the components of the stress tensor. Care must be taken into the fact that the non-locality of the peridynamics forces a new definition of the components of the stress different from the differential definition given in continuum mechanics for Cauchy stress tensors.

Furthermore, the majority of damage analysis done by peridynamics models focuses on the definition of stretch parameters in bond-based and state-based peridynamics. Stress calculation does not play a role in crack propagation analysis done in the literature. This study can be used for stress-based damage and fracture simulation using peridynamics. This includes J-integral calculation which relies on the stress contours at the vicinity of a crack tip.

References

[1] A.-L. Cauchy, Résumé des leçons données à l'École royale polytechnique sur le calcul infinitésimal, Paris: Impr. royale, 1823.

[2] J. R. Kermode, " Low-speed fracture instabilities in a brittle crystal.," *Nature,* no. 455, pp. 1224-1227, 2008.

[3] A. J. Pons and A. Karma, "Helical crack-front instability in mixed-mode fracture," *Nature,* no. 464, pp. 85-89, 2010.

[4] D. H. Warner, W. A. Curtin and S. Qu, "Rate dependence of crack-tip processes predicts twinning trend in f.c.c. metals," *Nature Mater,* no. 6, pp. 876-881, 2007.

[5] M. J. Buchler and H. Gao, "Dynamical fracture instabilities due to local hyperelasticity at crack tips," *Nature,* no. 439, pp. 307-310, 2006.

[6] J. Song and W. Curtin, "Atomic mechanism and prediction of hydrogen embrittlement in iron," *Nature Mater,* no. 12, pp. 145-151, 2013.

[7] A. Livne, E. Bouchbinder, I. Svetlizky and J. Fineberg, "The near-tip fields of fast cracks," *Science,* no. 327, pp. 1359-1363, 2010.

[8] R. K. Nalla, J. H. Kinney and R. O. Richie, "Mechanistic fracture criteria for the failure of human cortical bone," *Nature Mater,* no. 2, pp. 164-168, 2003.

[9] Z. P. Bazant, "Concrete fracture models: testing and practice," *Eng. Frac. Mech.,* no. 69, pp. 165-205, 2002.

[10] P. Ehrhart, "Properties and interactions of atomic defects in metals and alloys," Berlin, Springer, 2013, p. 88.

[11] R. W. Siegel, "Atomic defects and diffusion in metals," Yamada conference on point defects and defect interactions in metals, Kyoto, 1981.

[12] E. Emmrich and D. Puhst, "A short note on modeling damage in peridynamics," *J Elasticity,* vol. 123, no. 2, pp. 245-252, 2016.

[13] S. A. Silling, "Stability of peridynamic correspondence material models and their particle discretizations," *Comput. Methods Appl. Mech. Eng.,* vol. 322, pp. 42-57, 2017.

[14] A. A. Griffith, "The phenomena of rupture and flow in solids," *Philos. Trans. R. Soc.,* vol. 221, pp. 163-198, 1921.

[15] F. Z. Li, C. F. Shih and A. Needleman, "A comparison of methods for calculating energy release rates," *Engineering Fracture Mechanics,* vol. 21, no. 2, pp. 405-421, 1985.

[16] B. Budiansky and J. R. Rice, "onservation Laws and Energy-Release Rates," *J. Appl. Mech.,* vol. 40, no. 1, pp. 201-203, 1973.

[17] J. L. González-Velázquez, "Linear elastic fracture mechanics," in *A Practical Approach to Fracture Mechanics*, Elsevier, 2021, pp. 35-74.

[18] R. W. Hertzberg, R. P. Vinci and J. L. Hertzberg, Deformation and Fracture Mechanics of Engineering Materials, New Jersey: John Wiley & Sons, Inc., 2012.

[19] G. R. Irwin, "Analysis of stresses and strain near the end of a crack transversing a plate," *J. of Applied mechanics,* vol. 24, pp. 361-364, 1957.

[20] S. Timoshenko and J. N. Goodier, Theory of Elasticity, McGraw-Hill, 1951.

[21] M. H. Sadd, Elasticity: theory, applications, and numerics, Academic Press, 2009.

[22] D. P. Rooke and D. J. Cartwright, "Compendium of stress intensity factors," *HMSO Ministry of Defence,* 1976.

[23] M. Liu, "An improved semi-analytical solution for stress at round-tip notches," *Engineering Fracture Mechanics,* vol. 149, pp. 134-143, 2015.

[24] A. F. Bower, Applied mechanics of solids, CRC Press, 2009.

[25] R. W. Clough, "The finite element method in plane stress analysis," in *Proceedings of the 2nd ASCE conference on electroni*, 1960.

[26] R. Courant, "Variational methods for the solutions of problems of equilibrium and vibrations," *Bull. Am. Math. Soc.,* vol. 49, pp. 1-23, 1943.

[27] N. Moës, J. Dolbow and T. Belytschko, "A finite element method for crack growth without remeshing," *International Journal for Numerical Methods in Engineering,* vol. 46, no. 1, pp. 131-150, 1999.

[28] J. M. Melenk and I. Babuska, *Computer Methods in Applied Mechanics and Engineering,* vol. 39, pp. 289-314, 1996.

[29] K. Park and G. Paulino, "Cohesive Zone Models: A Critical Review of Traction-Separation Relationships Across Fracture Surfaces," *Applied Mechanics Reviews,* vol. 64, 2011.

[30] D. S. Dugdale, "Yielding of Steel Sheets Containing Slits,," *Journal of the Mechanics and Physics of Solids,* vol. 8, pp. 100-104, 1960.

[31] M. F. Kanninen and C. Popelar, Advanced Fracture Mechanics, New York: Oxford University Press, 1985.

[32] Z. P. Bazant and L. Cedolin, Stability of Structures: Elastic, Inelastic,, New York: Oxford University Press, 1991.

[33] J. L. Cribb and B. Tomkins, "On the Nature of the Stress at the Tip of," *J. Mech. Phys. Solids,* vol. 25, pp. 135-140, 1967.

[34] C. Y. Hui, A. Ruina, R. Long and A. Jagota, "Cohesive Zone Models," *J. Adhes.,* vol. 87, pp. 1-52, 2011.

[35] Z. Zhang and G. Paulino, "Cohesive Zone Modeling of Dynamic," *Int. J. Plast.,* vol. 21, pp. 1195-1254, 2005.

[36] W. Brocks and A. Cornec, "uest Editorial: Cohesive Models,," *Eng. Fract. Mech.,* vol. 70, pp. 1741-1742, 2003.

[37] A. Hillerborg, M. Modeer and P. Petersson, "Analysis of Crack Formation and Crack Growth in Concrete by Means of Fracture Mechanics and Finite Elements," *Cem. Concr. Res.,* vol. 6, pp. 773-781, 1976.

[38] W. Celes, G. Paulino and R. Espinha, "A Compact Adjacency-Based Topological Data Structure for Finite Element Mesh Representation," *Int. J. Numer. Methods Eng.,* vol. 64, pp. 1529-1556, 2005.

[39] J. Song and T. Belytschko, "Cracking Node Method for Dynamic Fracture With Finite Elements," *Int. J. Numer. Methods Eng.,* vol. 77, pp. 360-385, 2009.

[40] E. Madenci and E. Oterkus, Peridynamic Theory and Its Applications, New York: Springer, 2014.

[41] S. A. Silling, M. Epton and O. Weckner, "Peridynamic States and Constitutive Modeling," *J. Elasticity.,* vol. 88, pp. 151-184, 2007.

[42] U. Stocker, D. Juchli and W. F. van Gunsteren, "Increasing the Time Step and Efficiency of Molecular Dynamics Simulations: Optimal Solutions for Equilibrium Simulations or Structure Refinement of Large Biomolecules," *Molecular Simulation,* vol. 29, no. 2, pp. 123-128, 2003.

[43] S. A. Silling, "Peridynamics:Introduction," *Handbook of Nonlocal Continuum Mechanics for Materials and Structures,* pp. 1-38, 2018.

[44] Z. P. Bazant and M. Jirasek, "Nonlocal integral formulations of plasticity and damage: Survey of Progress," *Journal of Engineering Mechanics,* vol. 128, pp. 1119-1149, 2002.

[45] R. D. Mindlin, "Second gradient of strain and surface-tension in linear elasticity," *International Journal of Solids and Structures,* vol. 1, pp. 417-438, 1965.

[46] S. A. Silling, O. Weckner, E. Askari and F. Bobaru, "Crack nucleation in a peridynamic solid," *Int. J. Fract.,* vol. 162, no. 1-2, pp. 219-227, 2010.

[47] O. Weckner, G. Brunk, M. A. Epton, S. A. Silling and E. Askari, "Green's functions in non-local three-dimensional linear elasticity," *Proceedings of the Royal Society,* vol. 465, pp. 3463-3487, 2009.

[48] A. C. Eringen, "Linear theory of nonlocal elasticity and dispersion of plane waves," *International Journal of Engineering Science,* vol. 10, pp. 425-435, 1972.

[49] O. Weckner and R. Abeyaratne, "The effect of long-range forces on the dynamics of a bar," *Journal of the Mechanics and Physics of Solids,* vol. 53, pp. 705-728, 2005.

[50] A. Seagraves and R. Radovitzky, "Advances in Cohesive Zone Modeling of Dynamic Fracture,," in *Dynamic Failure of Materials and Structures*, Springer, 2009, pp. 349-405.

[51] A. Askari, Y. Azdoud, F. Han, G. Lubineau and S. Silling, in *Peridynamics for analysis of failure in advanced composite materials*, Woodhead Publishing, 2015, pp. 331-350.

[52] H. Yi-le, Y. Yin and H. Wang, "eridynamic analytical method for progressive damage in notched composite laminates," *Composite Struct ,* vol. 108, no. 1, pp. 801-810, 2014.

[53] J. Jung and J. Seok, "atigue crack growth analysis in layered heterogeneous material systems using peridynamic approach," *Composite Struct ,* vol. 152, pp. 403-407, 2016.

[54] D. De Meo, C. Diyaroglu, N. Zhu, E. Oterkus and M. Siddiq, "odelling of stress-corrosion cracking by using peridynamics," *Int J Hydrogen Energy,* vol. 41, no. 15, pp. 6593-6609, 2016.

[55] D. De Meo and E. Oterkus, "inite element implementation of a peridynamic pitting corrosion damage model," *Ocean Eng,* vol. 135, pp. 76-83, 2017.

[56] Z. Chen and F. Bobaru, "Peridynamic modeling of pitting corrosion damage," *J Mech Phys Solids,* vol. 78, pp. 352-381, 2015.

[57] Z. Chen, G. Zhang and F. Bobaru, "The influence of passive film damage on pitting corrosion," *J Electrochem Soc ,* vol. 163, no. 2, pp. C19-C24, 2016.

[58] H. Jiang, L. He, L. Fan and G. Zhan, "Numerical analysis method of cemented carbide turning tool's micro breakage based on peridynamic theory," *Int J Adv Manufacturing Technol ,* vol. 88, no. 5-8, pp. 1619-1628, 2017.

[59] B. Kilic and E. Madenci, "Prediction of crack paths in a quenched glass plate by using peridynamic theory," *Int. J. Fract.,* vol. 156, pp. 165-177, 2009.

[60] Y. D. Ha and F. Bobaru, "Characteristics of dynamic brittle fracture captured with peridynamics," *Engineering Fracture Mechanics,* vol. 78, no. 6, pp. 1156-1168, 2011.

[61] Y. Shi, "Creating atomic models of brittle glasses for in silico mechanical tests," *Int J Appl Glass Sci ,* vol. 7, no. 4, pp. 464-473, 2016.

[62] W. Liu and J. W. Hong, "Discretized peridynamics for brittle and ductile solids," *International Journal for Numerical Methods in Engineering,* vol. 89, no. 8, pp. 1028-1046, 2012.

[63] S. A. Silling, "Dynamic fracture modeling with a meshfree peridynamic code," *Computat. Fluid Solid Mech.,* vol. 1, pp. 641-644, 2003.

[64] A. Shojaei, T. Mudric, M. Zaccariotto and U. Galvanetto, "A coupled meshless finite point/Peridynamic method for 2D dynamic fracture analysis," *Int J Mech Sci ,* vol. 119, pp. 419-431, 2016.

[65] E. Madenci, K. Colavito and N. Phan, "Peridynamics for unguided crack growth prediction under mixed-mode loading," *Eng. Fract. Mech.,* vol. 167, pp. 34-44, 2016.

[66] Y. Shi, "Creating Atomic Models of Brittle Glasses for In Silico Mechanical Tests," *Int. J. Appl. Glass Sci.,* vol. 7, pp. 464-473, 2016.

[67] F. Bobaru, "Influence of van der Waals forces on increasing the strength and toughness in dynamic fracture of nanofibre networks: a peridynamic approach," *Modell. Sim. Mater. Sci. Eng.,* vol. 15, no. 5, p. 3970417, 2007.

[68] J. Lee and J. W. Hong, "Dynamic crack branching and curving in brittle polymers," *Int. J. Solids Struct.,* pp. 332-340, 2016.

[69] D. Huang, G. Lu and Y. Liu, "Nonlocal peridynamic modeling and simulation on crack propagation in concrete structures," *Math Problems Eng.,* pp. 1-11, 2015.

[70] W. Hu, Y. D. Ha and F. Bobaru, "Peridynamic model for dynamic fracture in unidirectional fiber-reinforced composites," *2012,* Vols. 217-220, pp. 247-261, Comput. Meth. Appl. Mech. Eng..

[71] M. Ghajari, L. Iannucci and P. Curtis, "A peridynamic material model for the analysis of dynamic crack propagation in orthotropic media," *Comput. Meth. Appl. Mech. Eng.,* vol. 276, pp. 431-452, 2014.

[72] G. Zhang, Q. Le, A. Loghin, A. Subramaniyan and F. Bobaru, "Validation of a peridynamic model for fatigue cracking," *Eng. Fract. Mech.,* vol. 162, pp. 76-94, 2016.

[73] G. Evangelatos and P. Spansos, "A collocation approach for spatial discretization of stochastic peridynamic modeling of fracture," *J Mech Mater Struct,* vol. 6, no. 7-8, pp. 1171-1195, 2011.

[74] F. S. Vieira and A. L. Araujo, "A peridynamic model for electromechanical fracture and crack propagation in piezoelectric solids," *Comput. Methods Appl. Mech. Engrg.,* vol. 412, 2023.

[75] D. Lu, Z. Song, G. Wang and X. Du, "Viscoelastic peridynamic fracture analysis for concrete beam with initial crack under impact," *Theoretical and Applied Fracture Mechanics,* p. 124, 2023.

[76] Y. Xiang, Z. Zhong and Z. Jiao, "An adaptive thermo-mechanical peridynamic model for crack analysis in anode-supported solid oxide fuel cell," *Journal of Power Sources,* vol. 547, 2022.

[77] Y. Hu and E. Madenci, "Peridynamics for fatigue life and residual strength prediction of composite laminates," *Composite Struct,* vol. 160, pp. 169-184, 2017.

[78] G. Zhang, Q. Le, A. Loghin, A. Subramaniyan and F. Bobaru, "A peridynamic model for dynamic fracture in functionally graded materials," *Composite Struct,* vol. 133, pp. 529-546, 2015.

[79] H. Wang, H. Dong, Z. Cai, Y. Liu and W. Wang, "Corrosion fatigue crack growth in stainless steels: A peridynamic study," *International Journal of Mechanical Sciences,* vol. 254, 2023.

[80] S. Silling, "Origin and effect of nonlocality in a composite," *J Mech Mater Struct,* vol. 9, no. 2, pp. 245-258, 2014.

[81] C. Sun and Z. Huang, "Peridynamic simulation to impacting damage in composite laminate," *Composite Struct,* Vols. 336-341, p. 138, 2016.

[82] B. Kilic, A. Agwai and E. Madenci, "Peridynamic theory for progressive damage prediction in center-cracked composite laminates," *Composite Struct,* vol. 90, no. 2, pp. 141-151, 2009.

[83] Y. Hu, N. De Carvalho and E. Madenci, "Peridynamic modeling of delamination growth in composite laminates," *Composite Struct,* vol. 132, pp. 610-620, 2015.

[84] C. Diyaroglu, E. Oterkus, E. Madenci, T. Rabczuk and A. Siddiq, "Peridynamic modeling of composite laminates under explosive loading," *Composite Structures,* vol. 144, pp. 14-23, 2016.

[85] T. Sadowski and B. Pankowski, "Peridynamical modelling of nanoindentation in ceramic composites," *Solid State Phenomena,* vol. 254, pp. 55-59, 2016.

[86] P. Wu and Z. Chen, "Peridynamic electromechanical modeling of damaging and cracking in conductive composites: A stochastically homogenized approach," *Composite Structures,* vol. 305, 2023.

[87] Y. L. Hu, J. Y. Wang, E. Madenci, Z. Mu and Y. Yu, "Peridynamic micromechanical model for damage mechanisms in composites," *Composite Structures,* vol. 301, 2022.

[88] E. Madenci, A. Yaghoobi and A. Barut, "Peridynamics for failure prediction in variable angle tow composites," *Arch Appl Mech,* vol. 93, pp. 93-107, 2023.

[89] S. A. Silling and E. Askari, "A meshfree method based on the peridynamic model of solid mechanics," *Computers and Structures,* vol. 83, pp. 1526-1535, 2005.

[90] K. Dayal and K. Bhattacharya, "Kinetics of phase transformations in the peridynamic formulation of Continuum Mechanics," *Journal of the Mechanics and Physics of Solids,* vol. 54, pp. 1811-1842, 2006.

[91] E. Askari and F. Bobaru, "Peridynamics for multiscale materials modeling," *Journal of Physics,* vol. 125, 2008.

[92] F. Bobaru and M. Duangpanya, "The peridynamic formulation for transient heat conduction," *International Journal of Heat and Mass Transfer,* 2010.

[93] R. W. Macek and S. A. Silling, "Peridynamics via finite element analysis," *Finite Elements in Analysis and Design,* vol. 43, no. 15, pp. 1169-1178, 2007.

[94] M. Parks, R. Lehoucq, S. Plimpton and S. A. Silling, "Implementing peridynamics within a molecular dynamics code," *Computer Physics Communications,* vol. 179, pp. 777-783, 2008.

[95] E. Emmrich and O. Wechner, "The peridynamic equation and its spatial discretization," *Math. Model. Anal.,* vol. 12, pp. 17-27, 2007.

[96] S. A. Silling and R. B. Lehoucq, "Convergence of peridynamics to classical elasticity theory," *Journal of Elasticity,* vol. 93, pp. 13-37, 2008.

[97] Y. D. Ha and F. Bobaru, "Studies of dynamic crack propagation and crack branching with peridynamics," *International Journal of Fracture,* vol. 162, pp. 229-244, 2010.

[98] F. Bobaru and W. Hu., "The meaning, selection, and use of the preidynamic horizon and its relation to crack branching in brittle materials," *Int. J. Fract.,* vol. 176, no. 2, pp. 215-222, 2012.

[99] D. Dipasquale, M. Zaccariotto and U. Galvanetto, "Crack propagation with adaptive grid refinement in 2D peridynamics," *Int. J. Fract.,* vol. 190, no. 1-2, pp. 1-22, 2014.

[100] R. Lipton, "Cohesive dynamics and brittle fracture," *J. Elasticity,* vol. 124, no. 2, pp. 143-191, 2016.

[101] R. Panchadhara and P. A. Gordon, "Application of peridynamic stress intensity factors to dynamic fracture initiation and propagation," *Int. J. Fract.,* vol. 201, no. 1, pp. 81-96, 2016.

[102] X. Zhou, Y. Wang and X. Xu, "Numerical simulation of initiation, propagation and coalescence of cracks using the non-ordinary state-based peridynamics," *Int. J. Fract.,* vol. 201, no. 2, pp. 213-234, 2016.

[103] S. Oterkus and E. Madenci, "Peridynamic modeling of fuel pellet cracking," *Eng. Fract. Mech.,* vol. 176, pp. 23-37, 2017.

[104] R. Beckmann, R. Mella and M. R. Wenman, "Mesh and timestep sensitivity of fracture from thermal strains using peridynamics implemented in Abaqus," *Comput. Meth. Appl. Mech. Eng.,* vol. 263, pp. 71-80, 2013.

[105] R. B. Lehoucq and A. S. S., "Force flux and the peridynamic stress tensor," *Journal of the Mechanics and Physics of Solids,* vol. 56, no. 4, pp. 1566-1577, 2008.

[106] A. S. Fallah and et al., "On the Computational Derivation of Bond-Based Peridynamic Stress Tensor," *Journal of Peridynamics and Nonlocal Modeling,* vol. 2, pp. 352-378, 2020.

[107] T. L. Warren, S. A. Silling, A. Askari, O. Weckner, M. A. Epton and J. Xu, "A non-ordinary state-based peridynamic method to model solid material deformation and fracture," *Int. J. Solids and Stru.,* vol. 46, no. 5, pp. 1186-1195, 2009.

[108] L. E. Malvern, Introduction to the Mechanics of a Continuous Medium, Englewood Cliffs, NJ.: Prentice-Hall, 1969.

[109] X. W. Jiang and H. Wang, "Crack-tip stress evaluation of multi-scale Griffitch crack subjected to tensile loading by using peridynamics," Scool of Aeronautics and Astronautics, Shanghai Jiao Tong University, Shanghai, 2017.

[110] D. Dipasquale, G. Sarego, P. Prapamonthon, S. Yooyen and A. Shojaei, "A Stress Tensor-based Failure Criterion for Ordinary State-based Peridynamic Models," *J. Appl. Comput. Mech.,,* vol. 8, no. 2, pp. 617-628, 2021.

[111] M. Asgari and M. A. Kouchakzadeh, "An equivalent von Mises stress and corresponding equivalent plastic strain for elastic–plastic ordinary peridynamics," *Meccanica,* vol. 54, pp. 1001-1014, 2019.

[112] M. Q. Le, "Mode-I J-integral via peridynamic stresses," *Int J Fract,* vol. 241, pp. 143-151, 2023.

[113] S. Li, "Peridynamic stress is a weighted static Virial stress," *arXiv,* Vols. arXiv:2103.00489v2 [physics.class-ph], 2021.

[114] N. Sau, J. Medina-Mendoza and A. C. Borbon-Almada, "Peridynamic modelling of reinforced concrete structures," *Engineering Failure Analysis,* vol. 103, pp. 266-274, 2019.

[115] H. Ren, X. Zhuang and T. Rabczuk, "Dual-horizon peridynamics: A stable solution to varying horizons," *Comput. Methods. Appl. Mech. Engrg,* no. 318, pp. 762-782, 2017.

[116] B. Wang, S. Oterkus and E. Oterkus, "Derivation of dual-horizon state-based peridynamics formulation based on Euler-Lagrange equation," *Continuum Mech. Thermodyn.,* pp. https://doi.org/10.1007/s00161-020-00915-y, 2020.

[117] M. Dorduncu and E. Madenci, "Finite element implementation of ordinary state-based peridynamics with variable horizon," *Engineering with Computers,* vol. 39, pp. 641-654, 2023.

[118] P. Underwood, "Dynamic relaxation," *Comput. Meth. Trans. Anal.,* vol. 1, pp. 245-265, 1983.

[119] E. Oterkus, Peridynamic Theory for Modeling Three-Dimensional Damage Growth in Metallic and Composite Structures, Arizona: The University of Arizona, 2010.

[120] S. A. Silling and R. B. Lehoucq, "Peridynamic Theory of Solid Mechanics," *Advances in Applied Mechanics,* vol. 44, pp. 73-168, 2010.

[121] J. A. Mitchell, "A nonlocal, ordinary, state-based plasticity model for peridynamcis," Sandia Report, 2011.

[122] S. A. Silling, "Reformulation of elasticity theory for discontinuities and long-range forces," *Journal of the Mechanics and Physics of Solids,* vol. 48, no. 1, pp. 175-209, 2000.

[123] S. A. Silling and E. Askari, "A meshfree method based on the peridynamic model of solid mechanics," *Computers & Structures,* vol. 83, no. 17, pp. 1526-1535, 2005.

[124] H. Ren, X. Zhuang, Y. Cai and T. Rabczuk, "Dual-horizon peridynamics," *Int. J. Numer. Meth. Engng,* no. 108, pp. 1451-1476, 2016.

[125] A. Katiyar, J. T. Foster, H. Ouchi and M. M. Sharma, "A peridynamic formulation of pressure driven convective fluid transport in porous media," *Journal of Computational Physics,* vol. 261, pp. 209-229, 2014.

[126] T. Rabczuk, H. Ren and X. Zhuang, "Dual-Horizon Peridynamics," in *Computational Methods Based on Peridynamics and Nonlocal Operators*, Springer, 2023, pp. 25-65.

[127] B. Kilic and E. Madenci, "An adaptive dynamic relaxation method for quasi-static simulations using the peridynamic theory," *Theoretical and Applied Fracture Mechanics,* vol. 53, pp. 194-204, 2010.

[128] R. A. Horn and C. R. Johnson, Matrix Analysis, New York: Cambridge University Press, 2013.

[129] G. R. Joldes, A. Wittek and K. Miller, "An adaptive Dynamic Relaxation method for solving nonlinear finite element problems. Application to brain shift estimation," *Int J Numer Method Biomed Eng,* vol. 2, no. 27, pp. 173-185, 2011.

[130] S. A. Silling, EMU user's manual, Sandia National Laboratories, Albuquerque: Code Ver. 2.6d., 2004.

[131] B. Wang, S. Oterkus and E. Oterkus, "Determination of horizon size in state-based peridynamics," *Continuum Mech. Thermodyn.,* pp. https://doi.org/10.1007/s00161-020-00896-y, 2020.

[132] Y. Tao, X. Tian and Q. Du, "Nonlocal diffusion and peridynamic models with Neumann type constraints and their numerical approximations," *Appl. Math. Comput.,* Vols. 282-298, p. 305, 2017.

[133] Q. V. Le and F. Bobaru, "Surface corrections for peridynamic models in elasticity and fracture,," *Comput. Mech.,* vol. 61, pp. 499-518, 2018.

[134] S. Oterkus, E. Madenci and A. Agwai, "Peridynamic thermal diffusion,," *J. Comput. Phys. ,* vol. 265, pp. 71-96, 2014.

[135] W. Hu, Y. D. Ha, F. Bobaru and S. A. Silling, "The formulation and computation of the nonlocal J-integral in bond-based peridynamics," *Int J Fract,* vol. 176, pp. 195-206, 2012.

[136] C. Stenstrom and K. Eriksson, "The J-area integral applied in peridynamics," *Int J Fract ,* pp. 127-142, 2021.

[137] Z. Zeng, H. Zhang, X. Zhang, Y. Liu and Z. Chen, "An adaptive peridynamics material point method for dynamic fracture problem," *Comput. Methods Appl. Engrg.,* no. 393, 2022.

[138] Q. Zeng, Z. Liu, D. Xu, H. Wang and Z. Zhuang, "Modeling arbitrary crack propagation in coupled shell/solid structures with X-FEM," *Int. J. Numer. Methods Eng.,* vol. 106, no. 12, pp. 1018-1040, 2016.

[139] M. L. Williams, "On the Stress Distribution at the Base of a Stationary Crack," *J. Appl. Mech,* vol. 24, no. 1, pp. 109-114, 2021.

[140] C. Truesdell, "A First Course in Rational Continuum Mechanics," *General Concepts,* vol. I, pp. 120-121, 1977.

[141] J. Trageser and P. Seleson, "Bond-Based Peridynamics: a Tale of Two Poisson's Ratios," *J. Peridyn. Nonlocal Model,* vol. 2, pp. 278-288, 2020.

[142] S. Silling, W. Gerstle and N. Sau Soto, "Peridynamic modeling of plain and reinforced concrete structures," *18th International Conference on Structural Mechanics in Reactor Technology,* 2005.

[143] T. Rabczuk and H. Ren, "A peridynamic formulation for quasi-static fracture and contact in rock," *Engineering Geology,* no. 225, pp. 42-48, 2017.

[144] N. Prakash and G. D. Seidel, "A novel two-parameter linear elastic constitutive model for bond based peridynamics," 2015.

[145] M. Ortiz and A. Pandolfi, "Finite-deformation irreversible cohesive elements for three-dimensional crack-propagation analysis," *Int. J. Numer. Methods Eng.,* vol. 44, no. 9, pp. 1267-1282, 1999.

[146] B. Moran and C. F. Shih, "A general treatment of crack tip contour integrals," *International Journal of Fracture,* vol. 35, pp. 295-310, 1987.

[147] R. Maranganti and P. Sharma, "Length scales at which classical elasticity breaks down for various materials," *Physical Review Letters,* vol. IV, 2007.

[148] E. Madenci, M. Dorduncu, A. Barut and N. Phan, "A State-Based Peridynamic Analysis in a Finite Element Framework," *Engineering Fracture Mechanics,* vol. 195, 2018.

[149] I. A. Kunin, "Elastic media with microstructure II: threedimensional," *Springer Series,* vol. 1, 2012.

[150] B. Kilic and E. Madenci, "Peridynamic Theory for Thermomechanical Analysis," *IEEE Transactions on Advanced Packaging,* vol. 33, no. 1, pp. 97-105, 2010.

[151] G. R. Irwin, "Analysis of Stresses and Strains Near the End of a Crack Traversing a Plate," *J. Appl. Mech.,* vol. 24, no. 3, pp. 361-364, 1957.

[152] Y. D. Ha and F. Bobaru, "Studies of dynamic crack propagation and crack branching with peridynamics," *Int. J. Fract.,* vol. 162, no. 1-2, pp. 229-244, 2010.

[153] Y. Gui, Y. Yu, Y. Hu, Y. Zhang and L. Lew, "A peridynamic cohesive zone model for composite laminates," *ournal of Peridynamics Nonlocal Model,* 2021.

[154] M. Elices, G. V. Guinea, J. Gomez and J. Planas, "The cohesive zone model: advantages, limitations and challenges," *Eng. Fract. Mech.,* vol. 69, pp. 137-163, 2002.

[155] M. Dorduncu and E. Madenci, "Finite element implementation of ordinary state-based peridynamics with variable horizon," *Engineering with Computers,* pp. https://doi.org/10.1007/s00366-022-01641-6, 2022.

[156] E. Budyn, T. Hoc and J. Jonvaux, "Fracture strength assessment and aging signs detection in human cortical bone using an X-FEM multiple scale approach," *Comput. Mech.,* vol. 42, no. 4, pp. 579-591, 2008.

[157] F. Bobaru, M. Yang, L. F. Alves, S. A. Silling, E. Askari and J. Xu, "Convergence, adaptive refinement, and scaling in 1D peridynamics," *Int. J. Numer. Meth. Engng,* no. 77, pp. 852-877, 2009.

[158] T. Belytschko, R. Gracie and G. Ventura, "A review of extended/generalized finite element methods for material modeling," *Model. Simul. Mater. Sci. Eng.,* vol. 17, no. 4, 2009.

[159] F. Amiri, C. Anitescu, M. Arroyo, S. A. Bordas and T. Rabczuk, "XLME interpolants, a seamless bridge between XFEM and enriched meshless methods," *Computational Mechanics,* vol. 53, no. 1, pp. 45-57, 2014.

[160] S. A. Silling, M. Zimmermann and R. Abeyaratne, "Deformation of a peridynamic bar," *Journal of Elasticity,* vol. 73, pp. 173-190, 2003.

[161] M. Zimmermann, "continuum theory with long-range forces for solids," PhD thesis, Massachusetts Institue of Technology, 2005.

[162] S. Silling, D. Littlewood and P. Seleson, "Variable horizon in a peridynamic medium," Sandia National Laboratories (SNL-NM), Albuquerque, NM (United States), 2014.

[163] S. Silling and A. Askari, "Peridynamic model for fatigue cracks," Technical Report 18590, Sandia National Laboratories, 2014.

[164] V. Buryachenko, "Some general representations in thermoperistatics of random structure composites," *Int J Multiscale Computat Eng,* vol. 12, no. 4, pp. 331-350, 2014.

[165] J. L. Gonzalez-Velazquez, "Linear elastic fracture mechanics," in *A Practical Approach to Fracture Mechanics*, Elsevier Inc., 2021, pp. 35-72.